

CHAPTER 4

DEVELOPMENT OF A NEW SEMI-GLOBAL RATE EXPRESSION FOR CHAR COMBUSTION MODELING

Introduction

Advanced energy systems will operate over a wider range of temperature, pressure, and oxygen concentration than existing pc-technology. For this reason a more robust and widely applicable rate expression may be required for char combustion modelling in these systems. In this chapter we describe work done on this project targeted at the development and testing of such a new rate expression.

Background

The carbon-oxygen reaction has been described as "arguably the most important reaction known" [1], and indeed it plays an important role in key industrial technologies that include ironmaking and the combustion and gasification of coal, biomass, and solid waste. Computer models are increasingly used in the design and retrofit of these processes, and the complex design codes require simple and efficient numerical submodels of char combustion. Development of these simple combustion models is made difficult by the complexity of the carbon-oxygen reaction mechanism, whose kinetics are known to be influenced by transient buildup of surface oxides [2-4], the surface migration of these oxides [5], inorganic catalysis [6-8], and pronounced heterogeneity of surface sites, characterized by broad distributions of activation energies both for adsorption [9] and desorption [6,10,11]. These phenomena are difficult to capture in simple combustion models.

A reasonable approach for practical char combustion modeling, therefore, is to postulate semi-global mechanisms that yield kinetic laws with the proper mathematical form to reproduce the major features of the kinetic data, while accepting their inability to predict some minor features, however well established by experiment. Here semi-global kinetics are defined as those comprising more than one explicit reaction step, wherein the steps themselves are not necessarily elementary. Intrinsic kinetics are defined as those not influenced by transport processes. With these definitions, the subject of this chapter is the best choice of semi-global intrinsic kinetic laws for char combustion modeling over the range of technologically important conditions.

A Review of Global Kinetic Parameters from Experiment

A specific goal of this chapter is to identify a semi-global intrinsic kinetic model that can reproduce the correct magnitudes of the temperature dependence (global intrinsic activation energy) and concentration dependence (global intrinsic reaction order) during steady-state combustion across the various temperature ranges of technological interest. The literature on the kinetics of the carbon-oxygen reaction is extensive and there is no universal consensus on the magnitude of the global orders or activation energies. Here a large set of existing data will be reviewed, covering a wide range in temperature and char type, but drawing only from experiments at near atmospheric pressure and reported in the more recent literature — an approach which reveals strong trends in the data.

Figure 4.1 shows a compilation of global intrinsic reaction orders reported in the literature at or near atmospheric pressure. For inclusion in Fig. 4.1 the reported experiments must have included an oxygen partial pressure in the range of 0.1-2 bar, evidence of detailed consideration of transport effects, and a publication date within the last thirty years. The data fall into two categories as reported by the original investigators: (a) Zone I values, corresponding here to all points below 900 K, and (b) intrinsic values extracted from Zone II (here all points above 1100 K) using transport models and/or the classic Thiele mapping relations: $E_{\text{observed}} = 1/2 E$; $n_{\text{observed}} = (n + 1)/2$, where the unsubscripted E and n represent intrinsic values.

Figure 4.1 shows strong evidence for high fractional order (0.6 - 1) in the low-temperature, Zone I regime. Most of these studies employed thermogravimetric analysis, a technique that can be readily assessed for the absence of most forms of transport limitations (through observation of the effects of bed mass and particle size on rate) and allows a nearly direct measurement of reaction order without the added uncertainty of parameter extraction through transport models. An example study in this group is that of Ranish and Walker [1], who, based on simple adsorption/desorption arguments, set out in search of expected zero order behavior at low temperature (733-842 K) and high pressure (1 - 64 bar), but found high order instead.

Results from the Zone II regime are less clear: many authors report half-order apparent kinetics, implying an intrinsic order of zero, but several studies report first order apparent kinetics implying an intrinsic order of unity. A number of authors cited in the Zone II regime report uncertainty in their own value of order (see points in parentheses) and very few have analyzed their data with fractional intrinsic order or with more detailed rate laws [12]. Despite the known difficulties determining accurate kinetic parameters from Zone II data, the set of cited studies as a whole do suggest low intrinsic order at high temperature (> 1100 K). Thus the global order of the carbon-oxygen reaction near atmospheric pressure appears to decrease from high to low as temperature increases from the onset of reaction near 600 K to the beginning of pc-flame conditions at 1500 K. Figure 4.1 shows that this transition occurs in or near some regimes of technological interest, so a kinetic law is sought that will be consistent with this basic trend.

Simple adsorption / desorption arguments strongly suggest the presence of a third regime in the high temperature limit, in which the reaction is adsorption controlled and first order in gaseous oxygen. Essenhigh and Mescher [12] have reported the beginnings of the adsorption control regime in that portion of Monson et al.'s data [13] that lies above 1273 K (with the remainder of the data near the zero order limit). Hong et al. [14] have recently analyzed the same data and found similar results, but report an adequate fit with zero order throughout. Overall, there are insufficient data in Fig. 4.1 to fully define the role of adsorption control at high temperature. It is likely, at atmospheric pressure and above, that the onset of adsorption control occurs in the high temperature regime where the rates are also significantly influenced by boundary layer diffusion, making accurate extraction of the adsorption kinetic parameters challenging in many cases.

A proposed semi-global kinetic law should also be consistent with observed global activation energies. Excluding highly pure heat treated carbons, there is relative agreement about the magnitude of the global intrinsic activation energy; it falls between 105 and 180 kJ / mol with many values in the range 130-150 kJ/mol, especially from the low temperature regime where direct measurement is possible. Other potentially useful

data for model evaluation are curves of reaction rate vs. oxygen partial pressure at a fixed temperature in the Zone I regime. Most studies, however, have not covered a wide range of partial pressures, and yield only a single, local value of the global reaction order as shown in Fig. 4.1. Exceptions are the TGA studies of Suuberg et al. [15], and more recently of Sawaya et al. [16], and of Roberts and Harris [17], both of which were concerned with pressurized combustion. These studies do not find an asymptotic value of the rate as pressure increases, as one might expect from the saturation of surface sites in classical Langmuir-Hinshelwood kinetics; rather the rates continue to increase with increasing pressure, yielding a power-law behavior with $n = 0.64 - 0.7$ [16] or $n = 0.68$ [15]. Roberts and Harris [17] contrast this behavior of O_2 with that of the gasifying agents H_2O and CO_2 , which do show asymptotic behavior in their high pressure data. Suuberg et al. [15] report a fractional reaction order (0.68) that remains constant over two orders of magnitude oxygen partial pressure, and comment that "no presently existing mechanistic model of O_2 gasification of char, with or without porous transport, is likely to be adequate for predicting ... [this behavior]." The central challenge for the present work is to suggest a kinetic model to reproduce the data in Figure 4.1, the observed magnitudes of the global activation energies, and the CO/CO_2 trends while maintaining simplicity appropriate for flame codes. Three candidate kinetic models are presented in Table 4.1 and discussed in turn below.

Model 1: Global Power-Law Kinetics

Entry 1 in Table 4.1 is the power-law or "nth order" form, which for $n \neq 0$ or 1 is entirely empirical in nature and cannot be derived from simple sequences of elementary steps. This expression is obviously unable to describe the variable global order seen in Fig. 4.1 and is inappropriate as a general form. Over limited ranges of temperature and pressure it may still find practical use, and with $n = 0$ it may be very useful in dedicated pulverized fuel codes that are restricted to the temperature range 1500 - 2000 K, where from Figure 4.1 the reaction appears to be of low order.

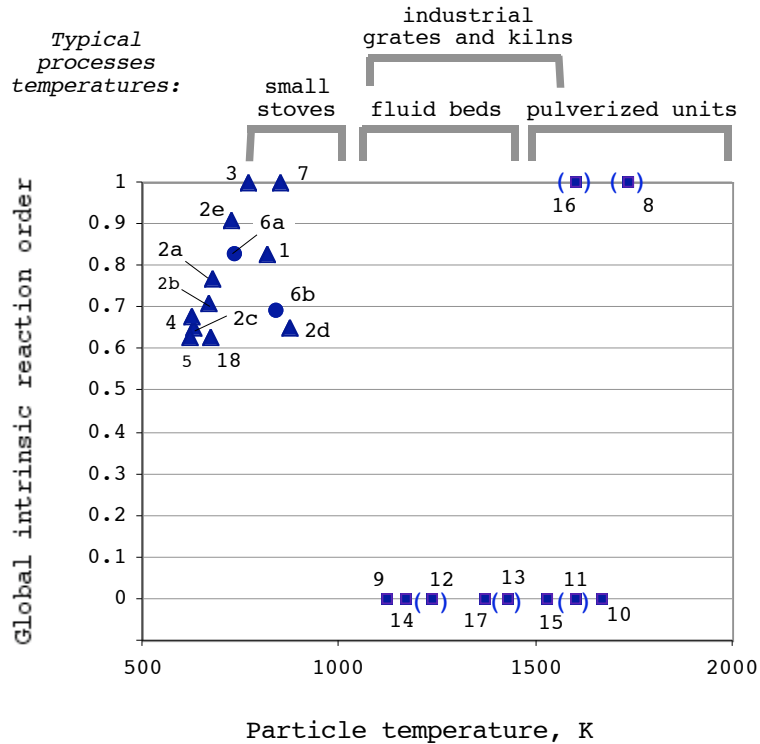


Figure 4.1: Compilation of global intrinsic reaction orders reported in the modern literature on char oxidation at near atmospheric pressure. For inclusion in Fig. 4.1 the reported experiments must have included an oxygen partial pressure in the range of 0.1-2 bar, been subject to detailed analysis of kinetics and transport, and been originally reported within the last thirty years. Triangles and circles were points reported as Zone I kinetics; squares are intrinsic parameters extracted from data reported to be in Zone II. Points in parentheses mark where original authors express uncertainty in the accuracy of their own reported reaction orders.

Figure 4.1 Data Key (Reference, carbon form, reaction temperature range)

- | | |
|---|--|
| 1. Du et al. [6], soot, 818 K | 10. Monson et al. [13] reanalyzed by Hong et al., [14] and by Essenhigh and Mesher [12]. The latter study reports zeroth order behavior over most of the data, but also the beginnings of a transition to adsorption control at high temperature (see Model 2) |
| 2. Sorenson and coworkers [32]
a,b. bituminous coals, 623-723 K
c. sub-bituminous coal, 573-673 K
d. coke, 777 - 885 K
e. activated carbon, 673-773 K | 11. Mitchell and McLean [37], pet. coke, coal, 1400-2200 K |
| 3. Lin et al. [33], bit. coal, 770 K | 12. Smith and Tyler [38], brown coal, 630 - 1812 K |
| 4. Suuberg et al. [15], phenol-formaldehyde resin char, 573-673 K | 13. Hamor et al. [39], brown coal, 630-2200 K. |
| 5. Hecker et al. [7] sub-bit. coal , 623 K | 14. Kurylko and Essenhigh [40], graphite, 873-1373 K |
| 6. Ranish and Walker [1], graphite, 733-842 K | 15. Essenhigh, 1970, anthracite, 1350-1750 K (presented in Essenhigh [19] as reference 37 therein. |
| 7. Croiset et al. [34], bit. coal, 850-1200 K. | 16. Field [41], various coals, 1200 - 2000 K |
| 8. Smith [35] pet. coke, anthracite, bit. coal, 1200-2270 K | 17. Young and Smith [42], pet. coke, 1000 - 1800 K |
| 9. Mathies [36], bit. coal, ~1200 K (typical | 18. Harris and Smith [43], pet. coke, brown coal, 500- |

Model 2: Langmuir-Hinshelwood (Two-Step) Semi-Global Kinetics

Entry 2 in Table 4.1 is the simplest of the Langmuir-Hinshelwood kinetic forms, as has been used for char combustion by a number of researchers. This rate law predicts an effective reaction order that varies with oxygen concentration and temperature. Activation energies for desorption have been measured in the range 160 - 400 kJ/mol [6,11,19], and those for adsorption in the range 10 - 125 kJ/mol [9,19], so for most surface sites $E_{\text{des}} \gg E_{\text{ads}}$. With this inequality the Langmuir-Hinshelwood form exhibits the following two limiting cases at a given pressure: $r_{\text{gas}} = k_2$ (zeroth order, desorption control) in the low temperature limit; and $r_{\text{gas}} = k_1 P_{\text{O}_2}$ (first order, adsorption control) in the high temperature limit. An example of the Langmuir-Hinshelwood behavior is shown in Fig. 4.2 using parameters reported by Essenhigh and Mescher [12] for the high temperature, high-pressure coal char combustion data of Monson et al. [13]. This predicted transition from low to high order with increasing temperature is precisely the opposite of the experimental behavior in the low-to-intermediate temperature range of Figs. 4.1 and 4.2. This discrepancy is further illustrated in the recent work of Hong et al. [14], who applied the Langmuir-Hinshelwood rate equation to three data sets from the literature. For two data sets in the high temperature regime they report the best fits with strict zero order (desorption control), in agreement with the general trend in Fig. 4.1 and 4.2 data. For the data of Ranish and Walker [1] at low temperatures (733 - 813 K) they achieve the best fits with $E_{\text{des}} = 172$ kJ/mol and $E_{\text{ads}} = 214$ kJ/mol [14]. These inverted activation energies ($E_{\text{ads}} > E_{\text{des}}$) were necessary to describe the observed decrease in reaction order with increasing temperature. The Langmuir-Hinshelwood law fit the data successfully, but the inverted activation energies likely negate any mechanistic

Table 4.1
Global and Semi-Global Mechanisms[†](left) and Rate Laws (right)

<p>Model 1. Global power-law</p> <p>1. $C + O_2 \rightarrow CO / CO_2$</p>	$r_{\text{gas}} = k P_{O_2}^n$
<p>Model 2. Langmuir-Hinshelwood</p> <p>1. $C + O_2 \rightarrow C(O)$</p> <p>2. $C(O) \rightarrow CO$</p>	$r_{\text{gas}} = \frac{k_1 k_2 P_{O_2}}{k_1 P_{O_2} + k_2}$ <p>(non-dissociative form)</p>
<p>Model 3. Three-step semi-global</p> <p>1. $C + O_2 \rightarrow 2C(O)$</p> <p>2. $C(O) + O_2 \rightarrow CO_2 + C(O)$</p> <p>3. $C(O) \rightarrow CO$</p>	$r_{\text{gas}} = \frac{k_1 k_2 P_{O_2}^2 + k_1 k_3 P_{O_2}}{k_1 P_{O_2} + k_3 / 2}$ $CO / CO_2 = \frac{k_3}{k_2 P_{O_2}}$ <p><i>all Model 3 calculations use:</i></p> <p>$A_2 = 5.7 \cdot 10^{-4} \text{ bar}^{-1}$ $E_2 = 130 \text{ kJ/mol}$ $E_3 = 180 \text{ kJ/mol}$ (normalized by $A_3 = 1.0$)</p>
<p>[†] in these semi-global "mechanisms", no attempt is made to define the precise stoichiometry of the steps or complexes, and the simplest forms of the rate laws are used, in which the reactions are assumed to be all first order (rather than second order) in surface densities.</p>	

significance of the fit. Langmuir-Hinshelwood kinetics are also unable to describe the persistent nth order behavior seen by Sawaya et al.[16] over a factor of 50 in P_{O_2} , and by Suuberg et al. [15] over a factor of 100 in P_{O_2} . The mathematical form of the Langmuir-Hinshelwood law allows zero order or first order as limiting cases, as well as a transition zone between the two, but the transition zone spans only about one order of magnitude in P_{O_2} . The simplest LH law is thus inappropriate as a general form, although it can be very useful in certain ranges of temperature and oxygen concentration.

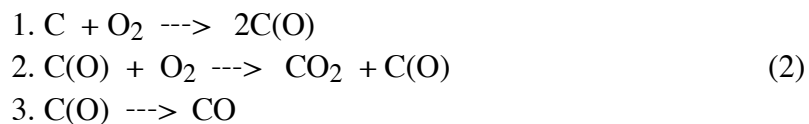
Model 3: Three-Step Semi-Global Kinetics

Both power-law and Langmuir-Hinshelwood kinetics do not provide even the crudest description of the reaction order data in Figs. 4.1 and 4.2. A solution to this problem is suggested by recent work on reactions involving gas phase oxygen with surface complexes:



which may or may not also involve the generation of a new complex, C(O), on the product side. Reactions of this class have been observed in a number of more recent studies [3,10,11,21], with the most direct proof coming from observations of isotopically mixed carbon dioxide, C¹⁸O¹⁶O, as the product of transient kinetic studies employing rapid switch-over from ¹⁸O₂ to ¹⁶O₂ [10,11,21]. This provides direct evidence for reaction of gas-phase oxygen, ¹⁶O₂, with previously formed complex, C(¹⁸O). In terms of magnitude, Ahmed and Back [3] find O₂- complex reactions to be an important source of CO₂ for gasification in oxygen pressures above 1 Torr; Zhuang et al. [10] find this reaction type to be the *main route* for CO₂ formation at 773 K in 0.05 bar O₂ using isotopic tracers. Most recently, Haynes and Newbury [11] report from isotopic tracer studies that 45% of the gasification at 873 K is due to O₂-complex reactions, falling to only 5% of the gasification at 1073 K. Further, both Zhuang et al. [21] and Haynes and Newbury [11] find that the O₂-complex reaction proceeds even on the thermally stable complexes, which in the absence of O₂ would not turn over fast enough at the reaction temperature to contribute significantly to the observed gasification. Thus in the presence of a broad distribution of desorption activation energies, the most stable complexes turnover preferentially by oxyreactivity (Eq.1), while on the same surface the labile complexes turnover preferentially by thermal desorption, producing a mixed reaction mode [11]. Analogous gas-complex reaction steps have been postulated to explain the kinetics of gasification with CO₂ [22] and steam [23].

These detailed surface studies provide a promising explanation for the high reaction orders at low temperature, since reaction (1) is nominally first order in oxygen. The following semi-global mechanism for steady-state combustion is suggested:



which is the basis for Model 3 in Table 4.1. It is in essence a version of the qualitative mechanistic pathway proposed by Tomita and coworkers [10], reduced here to allow quantitative treatment in combustion modeling.

In this semi-global "mechanism," any of the steps may be a lumped description of several more elementary steps. In particular, step 2 may represent any of the following:

- (a) direct collisional interaction between gaseous oxygen and a surface complex. This is a true Eley-Rideal reaction [24] as postulated early by Langmuir [25,26] for CO and H₂ reactions with oxygen complexes on platinum, and later generalized by Rideal [27].
- (b) the attack of sites adjacent to an existing complex resulting in complex destabilization and rapid desorption of CO₂. The rapid desorption makes this process first order in molecular oxygen.
- (c) Some modes of induced or intrinsic heterogeneity [1,28], in which adsorption activation energy increases and desorption activation energy decreases with increasing coverage. This trend can lead to partial or complete adsorption control at low temperatures where fractional coverage is very high.

Step 2 in Eq. 2 is the most appropriate semi-global step to describe elementary mechanisms (a) or (b). Mechanism (c) is better described by explicit models of surface heterogeneity, but step 2 in Eq. 2 can still mimic its global behavior, at least crudely, as it is a first-order process in gaseous oxygen that also requires the presence of complex. A number of observations support step 2 above as the primary pathway to CO₂, rather than



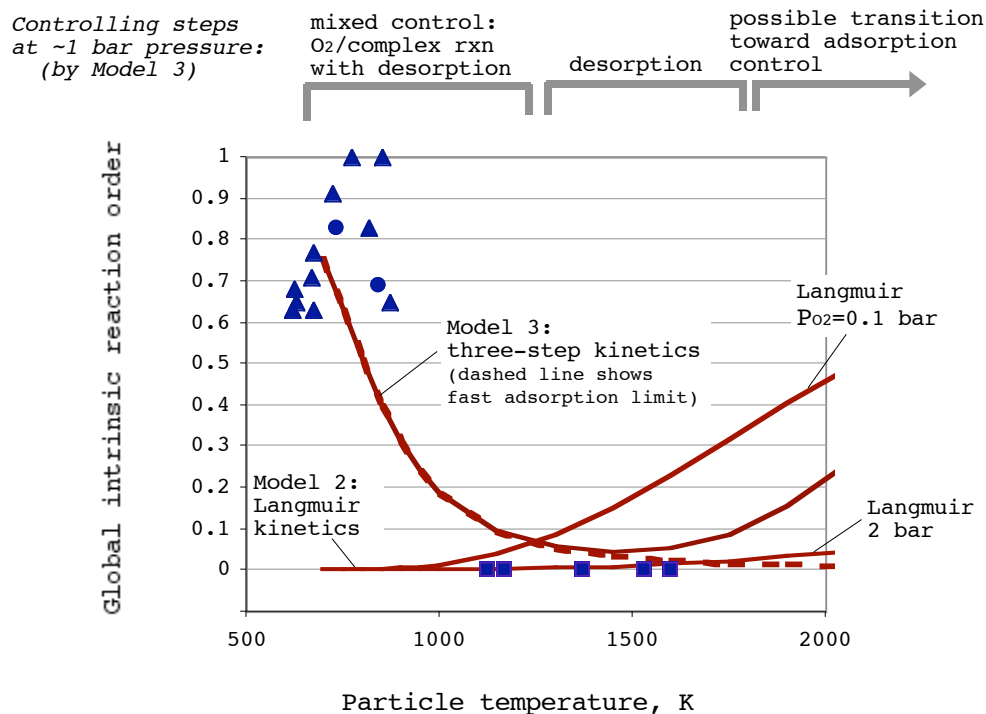


Figure 4.2. Data from Fig. 4.1 compared to behavior of two semi-global models. Model 2: Langmuir-Hinshelwood rate law (see 10 in key) at two different oxygen partial pressures; and Model 3: three-step semi-global rate law at 1 bar. The local global order is calculated from these models as: $n = (d \ln R / d \ln P)_T$.

Model 2 parameters: $A_{\text{ads}} = 0.435$, $E_{\text{ads}} = 31.4$ kJ/mol, $A_{\text{des}} = 4.5$, $E_{\text{des}} = 100$ kJ/mol from Klimesh and Essenhigh [20].

Model 3 parameters: $A_2 = 5.7 \cdot 10^{-4}$, $E_2 = 130$ kJ/mol, $E_3 = 180$ kJ/mol (normalized by $A_3 = 1.0$). Dashed line: fast (non-controlling) adsorption. Solid line: possible beginnings of adsorption control, using $A_1 = 3.3 \cdot 10^{-4}$, $E_1 = 35$ kJ/mol.

which is the favored explanation for CO₂ formation in all but the most recent literature. These observations include the high CO/CO₂ ratios seen during vacuum TPD relative to gasification conditions [1,6,21,29], the recent quantification of C¹⁸O¹⁶O in isotope tracer studies [10,11,21], and the inability of Eq. 3 to predict high reaction order at low temperature without additional model complexity as pointed out in this study.

For the quantitative treatment of Model 3 (Eq. 2), we will not define the precise stoichiometry with respect to free surface sites, "C" and will adopt instead the simplest form of the corresponding rate laws, which assume first order in site density:

$$R_1 = k_1 P_{O_2} (1-\theta) \quad (4)$$

$$R_2 = k_2 P_{O_2} \theta \quad (5)$$

$$R_3 = k_3 \theta \quad (6)$$

where θ represents the fraction of sites occupied by complex. These laws can be combined to yield the steady state expression for overall gasification rate and primary CO/CO₂ ratio:

$$r_{\text{gas}} = \frac{k_1 k_2 P_{O_2}^2 + k_1 k_3 P_{O_2}}{k_1 P_{O_2} + k_3/2} \quad (7)$$

$$\text{CO} / \text{CO}_2 = \frac{k_3}{k_2 P_{O_2}} \quad (8)$$

Based on the results of Haynes and Newbury [11] and the arguments of Ahmed and Back [3], one expects $E_3 > E_2 > E_1$, which yields the following limiting cases:

A) low temperature: $r_{\text{gas}} = k_2 P_{O_2}$ (O₂-complex reaction control) (9)
(k₃ small)

B) very high temperature: $r_{\text{gas}} = 2 k_1 P_{O_2}$ (adsorption control) (10)
(k₃ large)

both first-order processes. Depending on the magnitudes of the rate constants, several other degenerate forms may be seen at intermediate temperatures, including:

$$\text{C) low-moderate temperature: } r_{\text{gas}} = k_2 P_{\text{O}_2} + k_3 \quad (\text{mixed desorption / O}_2 \text{ / complex control}) \quad (11)$$

$(k_1 P_{\text{O}_2} \gg k_3)$

$$\text{D) moderate temperature } r_{\text{gas}} = k_3 \quad (\text{desorption control}) \quad (12)$$

$(k_1 P_{\text{O}_2} \gg k_3 \gg k_2 P_{\text{O}_2})$

$$\text{E) high-moderate temperature: } r_{\text{gas}} = \frac{k_1 k_3 P_{\text{O}_2}}{k_1 P_{\text{O}_2} + k_3/2} \quad (\text{Langmuir-Hinshel. type mixed adsorption / desorption control}) \quad (13)$$

$(k_1 P_{\text{O}_2}, k_3 \gg k_2 P_{\text{O}_2})$

It is immediately seen that inclusion of step 2 in Eq. 2 creates the potential to describe the data in Figs. 4.1 and 4.2 — as temperature increases global reaction order can shift from high (O₂-complex control, "A") to low (desorption control, "D") and back to high again (adsorption control "B"). It also provides some information on the CO/CO₂ ratio in the primary products which can be independently tested against data.

The full rate law, Eq. 7, contains 6 kinetic constants: the three pre-exponential factors, A₁, A₂, A₃; and activation energies: E₁, E₂, E₃ that define the three rate constants in Eq. 7, but not all need to be adjusted freely to test against the data. First, the experimental evidence for high temperature adsorption control is not perfectly clear in Figs. 4.1 and 4.2, so no attempt was made to adjust A₁ and E₁, as they affect only the high temperature region. Figure 4.2 shows two curves for the Model 3 prediction, a dashed curve in which A₁ and E₁ were set to give fast (non-limiting) adsorption, and a solid curve in which E₁ was set to a typical value for adsorption (35 kJ/mol) [19] and A₁ adjusted to show the beginnings of adsorption control at the highest temperatures in Fig. 4.2 — indicated by the upturn of the order curve. In addition, there was no attempt to predict an absolute rate, only the global order, and this is sensitive to the ratio A₂/A₃, but not to A₂ or A₃ individually. Therefore A₃ was set to unity and 3 parameters were adjusted: A₂, E₂, E₃ to closely match three sets of observations: (1) the global reaction order at atmospheric pressure (Fig. 4.2), (2) measured CO/CO₂ ratios surveyed by Skokova [18] (Fig. 4.3), and (3) the characteristic values of the global activation energy for oxidation, 105-180 kJ/mol.

A reasonable description of all the global behavior ratio is achieved with the following kinetic constants:

$$A_2 = 5.7 \cdot 10^{-4} \text{ bar}^{-1}, \quad E_2 = 130 \text{ kJ/mol}; \quad E_3 = 180 \text{ kJ/mol}$$

all normalized by setting $A_3 = 1.0$. Model 3 with these parameters provides an adequate fit to the global order data (Fig. 4.2), typical CO/CO₂ ratio behavior (Fig. 4.3), and gives an activation energy (Fig. 4.4) that varies from about 130 kJ/mol at $T = 700 \text{ K}$ to 180 kJ/mol at T from 900 - 1700 K. The slight increase in activation energy between 700 K and 900 K may or may not be detectable in laboratory data (as appreciated by visual examination of Fig. 4.4) or may be easily overridden by secondary effects not described by such a simple, semi-global model.

To achieve the fits in Figs. 4.1-3, $E_3 > E_2 > E_1$, as expected. Further, E_1 and E_3 are in the range quoted for adsorption and desorption activation energies [9,12], while E_2 is intermediate as expected, although it is much larger than the single value in the literature (130 kJ/mol vs. 34 kJ/mol estimated by Haynes and Newbury [11]). The effective "activation energy" for the CO/CO₂ ratio by Model 3 is $E_3 - E_2$ or 50 kJ/mol, very similar to the value reported by Arthur (52 kJ/mol) and in the middle of the range of later data sets (25-75 kJ/mol) as reviewed by Skokova [18].

The behavior of Model 3 can also be compared to the observation by Suuberg et al. [15] and Sawaya et al. [16], and Roberts and Harris [17] that the rate of low temperature oxidation does not reach an asymptotic value at high O₂ partial pressures, as would be expected from the saturation of surface sites by classical Langmuir-Hinshelwood kinetics. Figure 4.5 shows the predicted oxygen pressure dependence at 900 K using the full Model 3 mechanism with the standard parameter set (in Table 4.1). Clearly no saturation behavior is observed at high pressures. Figure 4.5 also shows a power-law fit with $n=0.8$. Model 3 cannot be strictly reduced to a power-law form, but can be approximated by one over about 1.5 orders of magnitude in oxygen partial pressure (1-30 bar). With two

orders of magnitude variation in P_{O_2} , the deviation from the power law behavior becomes quite clear, and therefore Model 3 alone cannot quite explain Suuberg's observation of persistent nth order behavior over two decades in P_{O_2} [15].

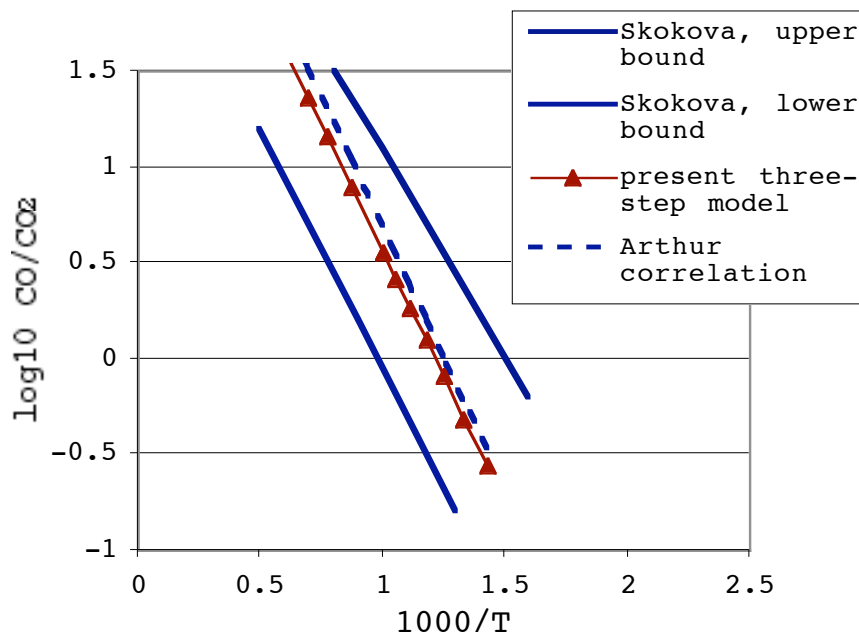


Figure 4.3. Survey of measured CO/CO_2 ratios adapted from Skokova [18] compared to predictions of the three-step, semi-global model (Model 3) with parameter set from Table 4.1: $A_2 = 5.7 \cdot 10^{-4} \text{ bar}^{-1}$; $E_2 = 130 \text{ kJ/mol}$; $E_3 = 180 \text{ kJ/mol}$ (all normalized to $A_3 = 1.0$). The shaded region encompasses about 80% of the data points in the original Skokova diagram [18]. Also shown is the correlation describing the CO/CO_2 measurements of Arthur [44].

Finally, Model 3 offers a simpler explanation than that previously available [1] for reaction orders that decrease with increasing temperature. The critical element in Model 3 is the inclusion of the CO_2 -producing step, step 2, which gives high order behavior at low temperature and near atmospheric pressure. It is likely that the role of reaction 2 (in Eq. 2) has been underestimated in much of the previous literature due to its diminished importance relative to Eq. 3 at the very low pressures used in many fundamental surface studies. This point has also been made by Ahmed and Back [3], who claim reaction 2 (in Eq. 2) is important in their data above $10^{-3} \text{ bar } O_2$, in contrast to the conclusions reached in previous studies at 10^{-6} bar [45,46]. By the argument of Ahmed and Back [3] it would certainly be dominant at the near atmospheric pressures in Figs. 4.1 and 4.2.

Model 3 for its extreme simplicity does a remarkable job of describing the trends in global reaction order, CO/CO₂, and global activation energy. It is not capable, however, of describing a number of other known features of the carbon-oxygen [47], for which more detailed models are still needed.

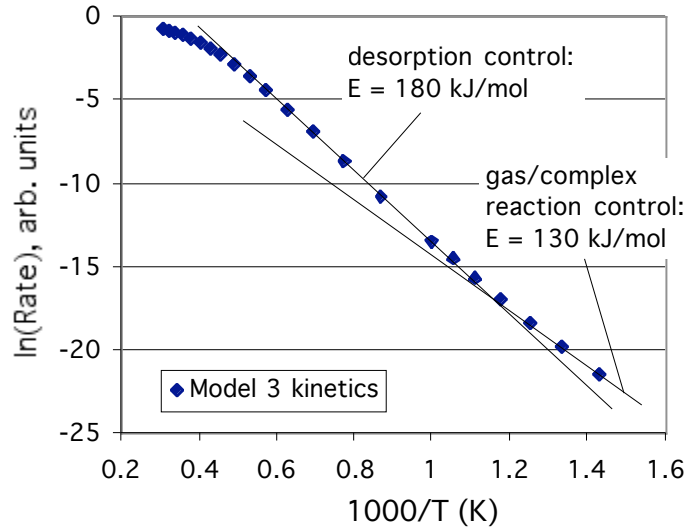


Figure 4.4. Points show Arrhenius behavior of Model 3 with parameter set: $A_2 = 5.7 \cdot 10^{-4} \text{ bar}^{-1}$; $E_2 = 130 \text{ kJ/mol}$; $E_3 = 180 \text{ kJ/mol}$ (all normalized to $A_3 = 1.0$). For illustration the calculation also uses $A_1 = 3.3 \cdot 10^{-4} \text{ bar}^{-1}$; $E_1 = 35 \text{ kJ/mol}$ to show the beginnings of a transition to adsorption control at high temperature. The lines point out two limiting regimes in the model.

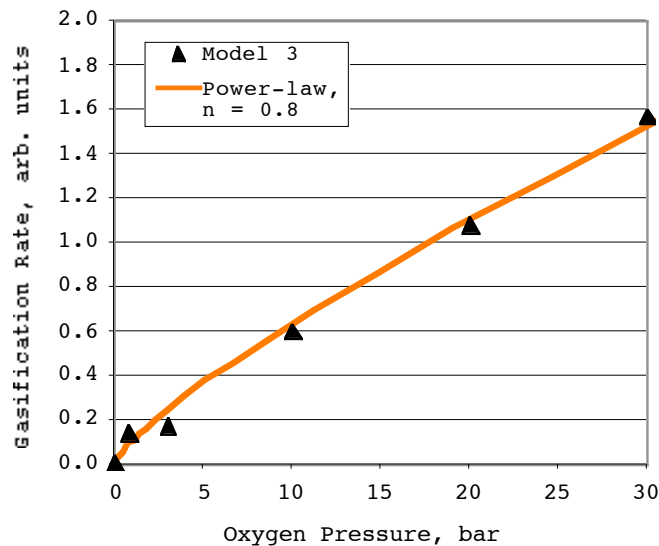


Figure 4.5. Model 3 behavior as a function of oxygen partial pressure at 900 K. The model behavior can be approximated as nth order with $n = 0.8$ over about 1.5 decades of oxygen partial pressure. Model 3 parameters are as in Figs. 4.2, 4.3, and 4.4.

Chapter 4 Conclusions

1. For char oxidation at O₂ partial pressures near atmospheric, there is strong experimental evidence for high intrinsic order in the low temperature, Zone I regime (< 900 K), significant though much weaker evidence for low intrinsic order in the high temperature, Zone II regime (> 1200K), and some suggestion of a transition toward a second higher-order regime at very high temperature (> about 1600 K).
2. Neither power-law kinetics nor Langmuir-Hinshelwood kinetics are appropriate as general forms for describing char combustion kinetics over the entire range of technological interest in temperature and oxygen pressure. Both zeroth order and Langmuir-Hinshelwood treatments can be appropriate under restricted conditions, especially at the high-temperatures prevailing in pulverized fuel combustion.
3. A three-step semi-global mechanism incorporating O₂-complex reaction is capable of describing the basic trends in global order, global activation energy, and CO/CO₂ ratio over a wide range of combustion conditions. The corresponding rate law is promising as a semi-empirical form for use in diverse combustion applications.
4. Beyond the global trends, there are many known features of carbon-oxygen kinetics that cannot be easily captured by models of the semi-global variety, and these features may be closely tied to heterogeneity in the energetics and chemical functionality of specific carbon active sites and their oxides.

Chapter 4 References

1. Ranish, J.M., and Walker, P.L. Jr., Carbon 31:135 (1993).
2. Phillips, R., Vastola, F.J., Walker, P.L. Jr., Carbon 8:205 (1970).
3. Ahmed, S., Back, M.H., Carbon 23:513 (1985).
4. Lizzio, A.A., Piotrowski, A., Radovic, L.R., Fuel 67:1691 (1988).
5. Yang, R.T., Wong, C., J. Chem. Phys. 75(9):4471 (1981).
6. Du, Z., Sarofim, A.F., Longwell, J.P., Energy and Fuels, 4:296 (1990).
7. Hecker, W.C., McDonald, K.M., Reade, W., Swenson, M.R., and Cope, R.F., Proceedings of the Combustion Institute, Vol 24, The Combustion Institute, Pittsburgh, 1992 pp. 1225-1231.
8. McKee, D.W., in Chemistry and Physics of Carbon, Vol. 16, (P.L. Walker, Jr., P.A. Throver, eds) Marcel Dekker, Inc. New York., 1981.
9. Brown, T.C., Lear, A.E., Haynes, B.S., Proceedings of the Combustion Institute, Vol 24, The Combustion Institute, Pittsburgh, 1992, pp. 1199-1206.
10. Zhuang, Q., Kyotani, T., Tomita, A., Energy and Fuels, 9:630 (1995).
11. Haynes, B.S., Newbury, T.G., Proceedings of the Combustion Institute, Vol 28, The Combustion Institute, Pittsburgh, 2000.
12. Essenhigh, R.H., Mesher, A.M., Proceedings of the Combustion Institute, Vol 26, The Combustion Institute, Pittsburgh, 1996, pp. 3085-3094.
13. Monson, C.R., Germane, G.J., Blackham, A.U., and Smoot, L.D., Combust. Flame, 100:669 (1995).
14. Hong J., Hecker, W.C., Fletcher, T.H., "Modeling High Pressure Char Oxidation Using Langmuir Kinetics with an Effectiveness Factor," Proceedings of the Combustion Institute, Vol 28, The Combustion Institute, Pittsburgh, 2000.
15. Suuberg, E.M., Wojtowicz, M., Calo, J.M. Proceedings of the Combustion Institute, Vol 22, The Combustion Institute, Pittsburgh, 1988, pp. 79-87.
16. Sawaya, R.J., Allen, J.W., Hecker, W.C., Fletcher, T.H., Smoot, D.S., ACS Division of Fuel Chem. Preprints, 44 1016-1019 (1999).
17. Roberts, D.G., Harris, D.J., Energy and Fuels, 14:483 (1993).
18. Skokova, K.A., "Selectivity in the Carbon-Oxygen Reaction," Ph.D. Thesis, The Pennsylvania State University, State College, PA, 1997.
19. Essenhigh, R.H., in Chemistry of Coal Utilization, Second Supplementary Volume (M.A. Elliott ed.) John Wiley and Sons, New York, 1981.
20. Klimesh, H.E., Essenhigh, R.H., Proceedings of the Combustion Institute, Vol 27, The Combustion Institute, Pittsburgh, 1998.
21. Zhuang, Q., Takashi, K., Tomita, A., Energy and Fuels, 10:169 (1996).
22. Blackwood, J.D., and Ingeme, A.J., Aust. J. Chem., 13:194 (1960).
23. Blackwood, J.D., and McGrory, F., Aust. J. Chem., 11:16 (1958).
24. Eley, D.D., and Rideal, E.K., Proc. Roy. Soc., London, Ser. A, 178:429 (1941).
25. Langmuir, I, Trans. Far. Soc., 17:607 (1921).
26. Langmuir, I., Trans Far. Soc. 17:621, (1921)
27. Rideal, E.K., Proc. Cambridge Phil. Soc. 35:130 (1939).
28. Brunauer, Love, and Keenan (J.A.C.S. 64:751 (1942).
29. Radovich, L.R., Lizzio, A.A., Jiang, H., in Fundamental Issues in Control of Carbon Gasification Reactivity (J. Lahaye and P. Ehrburger eds) p. 235, Kluwer Academic Publishers, Boston, 1990.
30. Calo, J.M., Perkins, M.T., Carbon 25:395 (1987).
31. Walker, P.L. Jr., Taylor, R.L., Ranish, J.M., Carbon 29:411 (1991).
32. Sorensen, L.H., Gjernes, E., Jessen, T., Fjellerup, J., Fuel 75(1):31 (1996).

33. Lin, S., Suzuki, Y., Hatano, H., Tsuchiya, K., *Chemical Engineering Science*, 55:43 (2000).
34. Croiset, E., Mallet, C., Rouan, J., Richard, J., *Proceedings of the Combustion Institute*, Vol 26, The Combustion Institute, Pittsburgh, 1996, pp. 3095-3102.
35. Smith, I.W., *Comb. and Flame*, 17:303 (1971).
36. Mathies, J.A., M.S. Thesis, Brigham Young University, Provo, Utah (1996).
37. Mitchell, R.E., McLean, W.J., *Proceedings of the Combustion Institute*, Vol 19, The Combustion Institute, Pittsburgh, 1982, pp. 1113 - 1122. .
38. Smith, I.W., Tyler, R.J., *Combustion Science and Technology*, 9:87 (1974).
39. Hamor, R.J., Smith, I.W., Tyler, R.J., *Combustion and Flame*, 21:153 (1973).
40. Kurylko, L., Essenhigh, R.H., *Proceedings of the Combustion Institute*, Vol 14, The Combustion Institute, Pittsburgh, 1973, pp. 1375-1386.
41. Field, M.A., *Combustion and Flame*, 14:237 (1970).
42. Young, B.C., Smith, I.W., *Proceedings of the Combustion Institute*, Vol 18, The Combustion Institute, Pittsburgh, 1981, pp. 1249-1255.
43. Harris, D.J., Smith, I.W., *Proceedings of the Combustion Institute*, Vol 23, The Combustion Institute, Pittsburgh, 1990, pp. 1185-1190.
44. Arthur, J.R., *Trans. Faraday Soc.*, 7:164 (1951).
45. Laine N.R., Vastola, F.J., Walker, P.L. Jr. *J. Phys. Chem.* 67 2030 (1963).
46. Walker P.L.Jr., Vastola, F.J., Hart, P.J., *Fundamentals of Gas-Surface Interactions* (Editors H. Saltsburg, J. Smith, M. Rogers), Academic Press, New York, 1967.
47. Hurt, R.H., Calo, J.M., *Combustion and Flame*, in press

CHAPTER 5

ON THE ORIGIN OF POWER-LAW KINETICS IN CHAR COMBUSTION

A limitation of the semi-global rate model presented in the previous chapter is its inability to describe the persistent power-law behavior typically observed in low-temperature char combustion. This chapter focuses on the origin of the power law behavior and also serves as a comparative evaluation of the straight power law approach (used in CBK8), relative to more complex rate laws such as that used in CBK/E. The overall goal, again, is to identify the best approach for high pressure conditions expected in advanced combustors and gasifiers.

The simple stoichiometry of the carbon/oxygen reaction, $C + O_2 \rightarrow CO / CO_2$, belies a complex kinetic behavior, which has to date prevented a consensus on the kinetic parameters or even the proper form of the rate expression. Identifying the most appropriate rate form remains an important practical goal, since in the long term it will allow more meaningful correlation and unification of the data needed to design furnaces and burner systems.

This chapter focuses initially on low-temperature studies (< 1000 K) where the kinetic data are much more suitable to detailed analysis, and on near-atmospheric studies ($P_{ox} > 0.01$ bar), which are of greatest technological relevance. This literature contains many reports of fractional orders (see Fig. 5.1), a fact that suggests complex kinetics. The Fig. 5.1 data includes a large and significant cluster of high fractional reaction orders, but also credible reports of low order [1,2], and a robust kinetic law must be capable of predicting both. Most of the studies in Fig. 5.1 employ relatively narrow ranges of oxygen pressure (factors of 3-10) and the reported orders that are best interpreted as local values, $n_{loc} = d \ln R / d \ln P$, that are slopes of some governing kinetic law whose functional form is not directly revealed. One of several exceptions in the literature is the study of Suuberg et al.[5.4], who measured combustion rates from 0.005 - 1 bar oxygen partial pressure from 573-673 K for a phenol-formaldehyde resin char (see Fig. 5.2). These authors find that the rates followed a power-law form: $R = k P_{ox}^n$, where n is constant at 0.62 over the entire range of oxygen pressure (see Fig. 5.2a). Similar

behavior has been observed in a recent study motivated by technological interest in high-pressure combustion and gasification[5,6] (see Fig. 5.2b).

This "persistent" power-law behavior is inconsistent with simple theories of adsorption and desorption on homogeneous (i.e. single site type) surfaces, which give the Langmuir law:

$$R = k_{des} k_{ads} P_{ox} / (k_{des} + k_{ads} P_{ox}) \quad (1)$$

This form requires the reaction to be first order, zeroth order, or in a transition zone between the two. Logarithmic differentiation of Eq. 1 yields the local reaction order implicit in the Langmuir law:

$$n_{local} = d \ln R / d \ln P = 1 / [1 + (k_{ads} P_{ox} / k_{des})] \quad (2)$$

Defining the transition region as $0.2 < n_{local} < 0.8$, its width by Eq. 2 is always a factor of 16 in oxygen pressure regardless of the specific values of k_{ads} and k_{des} . Experimental

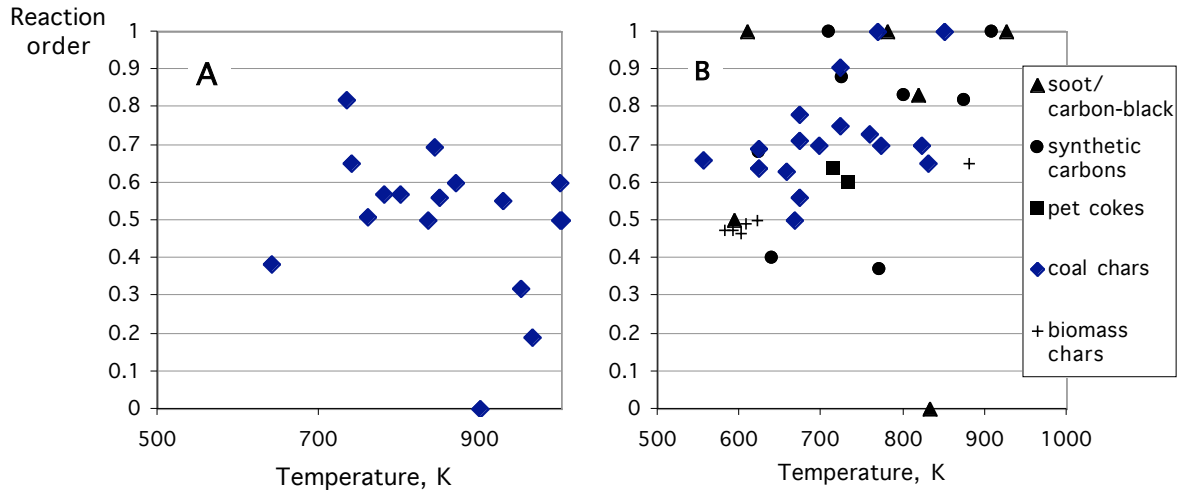


Figure 5.1. Summary of measured reaction orders reported in the literature for carbon oxidation at $T < 1000$ K, $P_{ox} > 0.01$ bar. **A:** graphitic carbons, **B:** non-graphitic carbons. The coal char data in this figure was taken from a previous compilation [3].

verification of this transition is conspicuously absent in the low-temperature carbon oxidation literature. The power law behavior reported by Suuberg et al. [4] over a factor of 200 in oxygen pressure is particularly incompatible with the simple Langmuir form (see Fig. 5.2). Further since measured activation energies for transient desorption are typically much greater than those for adsorption, this form requires zeroth order in the low-temperature, high-pressure limit, which is incompatible with the majority of the low-temperature data in Fig. 5.1. The power-law form may be an attractive alternative, but without a fundamental basis its use in combustion models will remain empirical and ultimately controversial.

The present chapter addresses the mechanistic origin of power-law kinetics by drawing from the fundamental literature on heterogeneous (real) surfaces. We will show that global power-law kinetics is a natural consequence of the already well-established heterogeneity of real carbon surfaces [7-10], whether the heterogeneity is intrinsic or induced. The chapter then compares the specific heterogeneous surface model of Haynes[11] to several example datasets and the results used to discuss the main features of the carbon oxidation database in the intrinsic regime at $T < 1000$ K and $P_{ox} > 0.01$ bar.

Simple Treatments of Turnover Kinetics on Heterogeneous Surfaces

This section explores the effects of surface heterogeneity on the global kinetics of a general heterogeneous reaction using simple theories of intrinsic and induced heterogeneity.

Intrinsic heterogeneity

Almost all solid surfaces exhibit site-to-site variations in turnover rates that reflect intrinsic local variations in bonding, composition, or surface nanotopology[12]. This intrinsic heterogeneity appears most notably as variations in activation energies for adsorption, surface reaction, and/or desorption. The simplest model of intrinsic heterogeneity assumes Langmuir kinetics on parallel, independent reaction sites with a

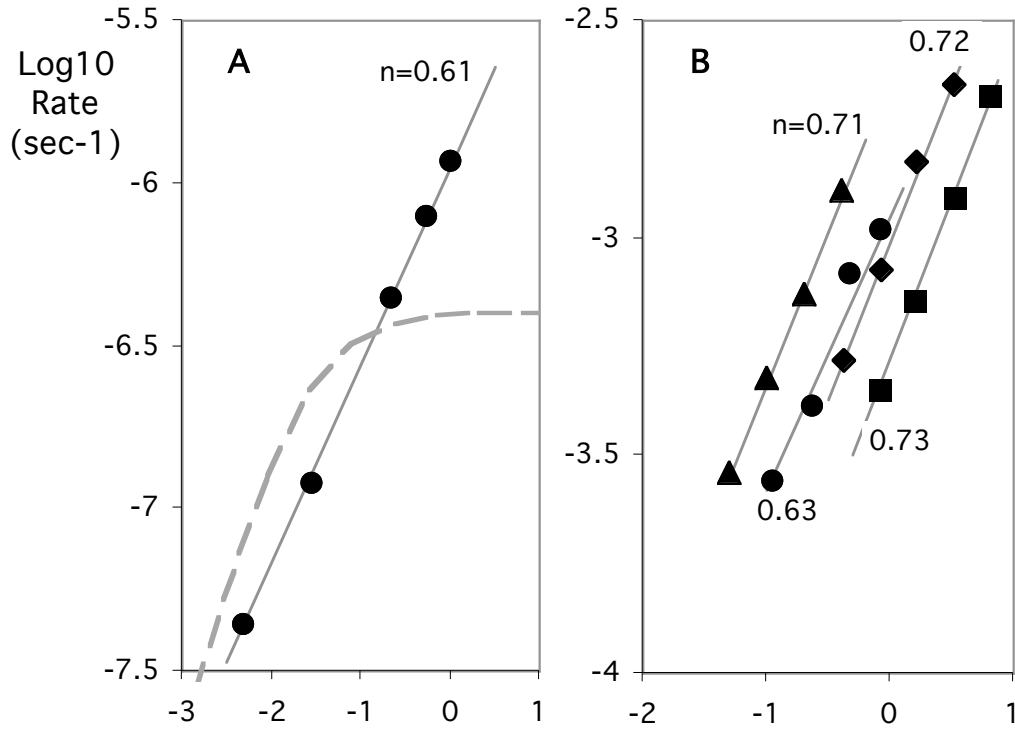


Figure 5.2. Global pressure dependence of low-temperature carbon oxidation kinetics on non-graphitic chars in the data of **A**: Suuberg et al. [4] for a phenol-formaldehyde resin char, and **B**: Madsen et al.[5] (see also Hecker et al.[6]) for high pressure oxidation of Pittsburgh seam bituminous coal char at various temperatures (triangles: 823 K, circles: 773, diamonds: 748K, squares: 723 K). The straight lines are empirical power-law fits with the best-fit exponent for each curve shown on the graph. The dashed curve shows the single-site Langmuir form, which always undergoes a transition from global first to zeroth order over a factor of 16 in oxygen pressure.

distribution of activation energies. For illustration we consider the effect of a distribution of the desorption energies only, and write the total rate as:

$$R_{global} = \int f(E_{des})R(E_{des})dE_{des} \quad (3)$$

where R_{global} is the overall rate of gasification, $f(E_{des})$ is the site density distribution, and R is given by Eq. 1 where k_{des} depends on E_{des} , and k_{ads} is a simple rate constant. Figure 5.3 shows the pressure dependence predicted by Eq. 3 for Gaussian distributions of E_{des} with various values of the standard deviation, σ_{E-des} . As the distribution breadth, σ_{E-des} , increases from 0 (the uniform surface) to 80 kJ/mol, the pressure dependence shifts gradually from the Langmuir-type to a linear $\log R_{global}-\log P$ relation. At $\sigma_{E-des} = 20$

kJ/mol the $R_{global}-P$ relation is adequately approximated by a power law function over about 3 orders of magnitude in pressure, while at $\bar{E}_{des} = 80$ kJ/mol the behavior is indistinguishable from power law kinetics over the entire range of calculation. Whether power-law behavior is observed in practice depends critically on the breadth of the energy distribution, \bar{E}_{des} for the solid surface in question.

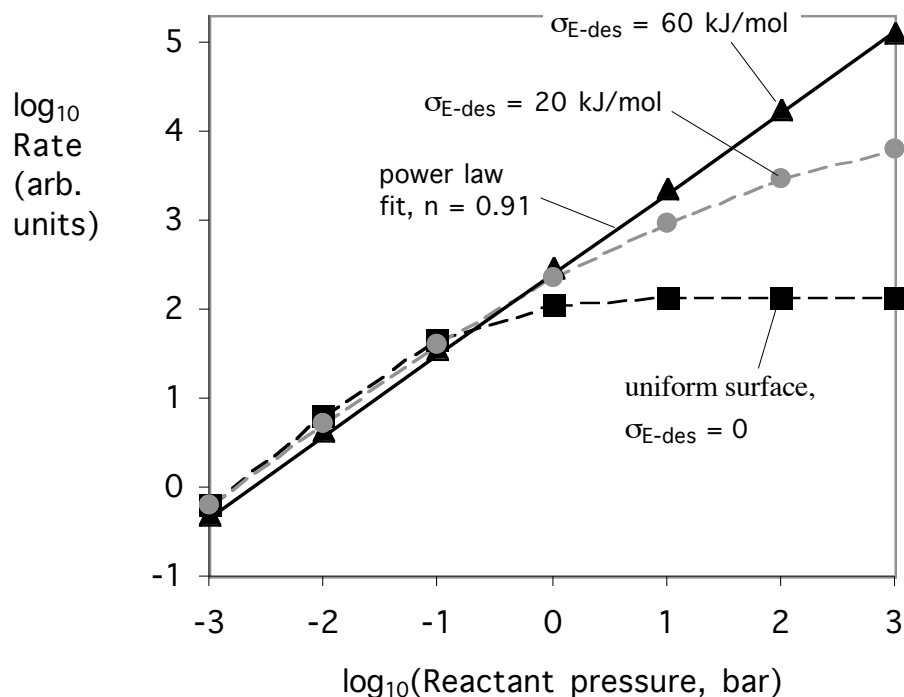


Figure 5.3. Behavior of the global reaction rate predicted by simple treatment of generic solid surfaces possessing *intrinsic* site heterogeneity. As the breadth of the desorption activation energy distribution, \bar{E}_{des} , increases, the global behavior gradually shifts from Langmuirian kinetics with its surface-saturated asymptote to a linear $\log R_{global}$ vs. $\log P$ relationship indicating power-law kinetics.

Induced heterogeneity

A second form of surface heterogeneity is not intrinsic to the solid phase, but occurs when adsorbed species influence the energetics of surface reactions. Chemisorbed species can alter solid surface properties through electron donation or withdrawal, or can interact with neighboring adsorbed species in either a cooperative or competitive fashion.

Chemisorption on one site can either inhibit adsorption on neighboring sites by steric exclusion or can enhance adsorption on those sites by adsorbate-adsorbate attractive forces[12]. In each case the result is an activation energy for adsorption and/or desorption that varies with surface coverage, θ .

A very simple model describing this induced heterogeneity allows both adsorption and desorption activation energies to vary with coverage according to:

$$E_{ads} = E^o_{ads} + \alpha \theta ; \quad E_{des} = E^o_{des} - \beta \theta \quad (4)$$

where α and β are parameters. Equating the rates of adsorption and desorption at steady state yields:

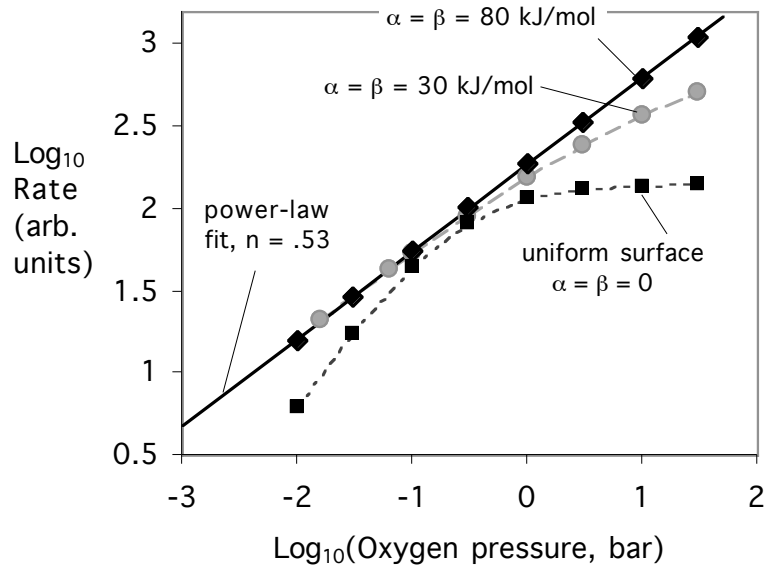
$$R_{global} = A_{ads} e^{-((E_{o,ads} + \alpha \theta)/RT)} P_{ox}(1-\theta) = A_{des} e^{-((E_{o,des} - \beta \theta)/RT)} \theta \quad (5)$$

which defines a complete model that for a given set of conditions can be solved numerically for coverage, θ , and then global rate. At $\alpha=\beta=0$ this model reduces to the one-site Langmuir form, while Fig. 5.4 shows that large values of α and/or β give a global behavior that is essentially indistinguishable from power-law kinetics. The global behavior is quite similar to that for intrinsic heterogeneity in Fig. 5.3, though the mathematical formulations are rather different, Eq. 3 being a statistical relation.

The origin of this power-law behavior imbedded in Eq. 5 can be understood as follows. Adsorption slows sharply as coverage increases, and desorption slows sharply as coverage decreases, so the steady-state coverage, which represents a competition between adsorption and desorption rates, does not easily reach either limiting case (desorption control at $\beta=1$, or adsorption control at $\alpha=0$). Rather, the coverage remains at intermediate values over wide ranges of pressure, and the reaction occurs in a stable regime of mixed adsorption/desorption control that yields n^{th} -order kinetics.

Figure 5.4.

Behavior of the global reaction rate predicted by simple treatment of generic solid surfaces possessing *induced* heterogeneity. Parameters Δ , \square describe the coverage-dependence of adsorption and desorption activities energies respectively. As they increase, the global behavior gradually shifts from Langmuirian kinetics to a linear $\log R_{global}$ vs. $\log P$ relationship indicating power-law kinetics.



Surface Heterogeneity in Carbon Oxidation

The turnover model of Haynes

Here we consider a specific formulation for carbon oxidation that has been developed by Haynes and coworkers[10,13] from transient measurements of adsorption and desorption for Sphero carb. This work culminated recently in a turnover model[11] based on the following reaction sequence:

1. $C + O_2 \rightarrow C(O) + CO$
2. $C(O) \rightarrow CO$ (6)
3. $C(O) + O_2 \rightarrow C(O) + CO/CO_2$

The Haynes turnover model contains explicit descriptions of site heterogeneity and has been shown to provide a good prediction of Sphero carb burning rates at 2.7 Pa from 873-1073 K[11]. Here we use a pseudo-steady version of this model to explore carbon

oxidation kinetic behavior over wide pressure ranges. The key equations in the Haynes turnover model used here are:

$$R_{ads} = A_{ads} e^{(-E_{ads}/RT)} P_{ox} (1-\theta) \quad (7)$$

where θ is the fraction coverage and A_{ads} comes from gas kinetic theory as:

$$A_{ads} = S / (2\theta M_{O_2} RT)^{1/2} \quad (8)$$

The activation energy, E_{ads} , is coverage-dependent according to

$$E_{ads} = a + b \ln(N) \quad (9)$$

where N is the total number of oxides and a and b are parameters. Experimentally determined parameters for Spherocharb are: $a = 165$ and $b = 10.38$ for N in mol/kg-carbon and E_{ads} in kJ/mol [11]. The desorption rate is obtained by integration over a distribution of sites of varying desorption activation energy:

$$R_{des} = \int A_{des} e^{(-E_{des}/RT)} q(E_{des}) f(E_{des}) dE_{des} \quad (10)$$

where A_{des} is 10^{14} sec^{-1} and the site density $f(E_{des})$ distribution has been determined for Spherocharb by TPD experiments with variable isothermal soak time. The present version adopts a Gaussian form for the distribution, as also assumed in the work of Du et al.[8], with baseline parameters from the Spherocharb studies: mean $E_{des} = 300 \text{ kJ/mol}$ and $\sigma_{des} = 60 \text{ kJ/mol}$.

At pseudo-steady-state, $R_{ads} = R_{des}$ since the gas-complex reaction step propagates the complex, and the overall gasification rate is:

$$R_{global} = R_{des} + R_{g-c} \quad (11)$$

The gas/complex reaction step underlying R_{g-c} (step 3) is not as well understood as steps 1 and 2. There is evidence of its importance at 2.7 Pa and 870-1080 K, but a reliable assessment of its role in traditional char combustion kinetic experiments at and above atmospheric pressure awaits further experimental data. The present study therefore focuses on the role of heterogeneity in reaction steps 1 and 2, where detailed quantitative treatments of site energy distributions are available from TPD experiments[10]. A minor modification was made to the original Haynes formulation[11] by introducing a total site number as a parameter to facilitate the examination of widely diverse carbon surfaces. A value of 0.85 mol/gm was used for the disordered carbons in this study (a value near the maximum experimental coverage in transient chemisorption data for Spherocarb[11]), while for graphite the parameter was adjusted to fit the data of Tyler as described later.

Figure 5.5 shows the Haynes model predictions with the previously determined numerical values for Spherocarb. The steady-state global kinetics follow fractional power-law kinetics ($n = 0.78$) over the entire numerical range — at least 6 orders of magnitude in oxygen pressure. In agreement with the previous simple heterogeneous surface model, this model of carbon oxidation predicts persistent n^{th} -order behavior to be a natural consequence of a broad distribution of activation energies. Figure 5.5 also shows a series of cases in which the E_a distribution for desorption is artificially narrowed in steps to examine behavior. At half the original breadth ($\Delta = 30$ kJ/mol) the persistent n^{th} -order behavior remains, but when the heterogeneity is essentially removed ($\Delta = 0.1$ kJ/mol), curvature in the $\log R_{\text{global}} - \log P_{\text{ox}}$ space appears. Only when both the desorption and adsorption heterogeneity are effectively removed ($\Delta = 0.1$ kJ/mol, $b = 0$ in Eq. 9) does the model collapse to the simple Langmuir law with its distinct transition from first to zeroth order. The actual distribution breadth for Spherocarb is 60 kJ/mol, and a similar TPD profile has been reported for a low-rank coal char[14], so based on these results persistent power-law behavior would be expected for both of these disordered carbons.

Partitioning of $f(E_{des})$ into three site classes

Figure 5.6 provides more insight into the origin of the persistent power-law behavior. For each value of E_{des} in the distribution, adsorption and desorption rates can be equated and the resulting local value of coverage, $\theta(E_{des})$, can be used to define three site classes:

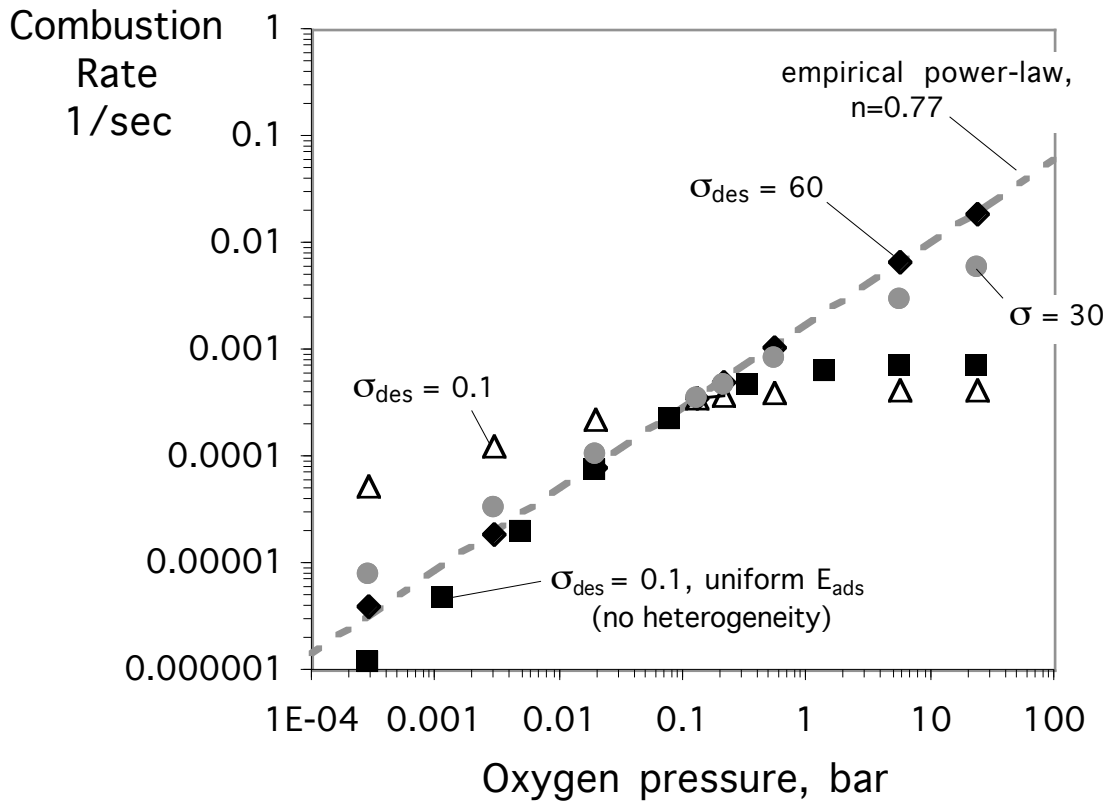


Figure 5.5. Oxygen pressure dependence predicted by a pseudo-steady version of the Haynes turnover model[11]. Using the original reported parameters for Spherocharb ($E_{des} = 60$ kJ/mol) the predictions follow a global power-law form ($n=0.78$) over at least 6 orders of magnitude in oxygen pressure. Additional curves give predictions with the original breadth of the desorption activation energy distribution artificially reduced from 60 to 30 to 0.1 kJ/mol. Note the mean desorption activation energy was adjusted to hold the absolute rate fixed at an oxygen pressure of 0.1 bar. The black squares show the Langmuirian behavior only when both adsorption and desorption distributions are narrowed to effectively zero breadth.

adsorption limited sites with $\theta \ll 1$, desorption-limited sites with $\theta \gg 1$, and transitional sites with fractional coverage. For this analytical form we define a parameter $E_{0.5}$ as the

desorption activation energy on those sites that are exactly half covered ($\theta=0.5$) at pseudo-steady-state, obtained by solving:

$$A_{ads} e^{-E_{ads}/RT} P_{ox} (1-\theta) = A_{des} e^{-E_{des}/RT} \theta \quad (12)$$

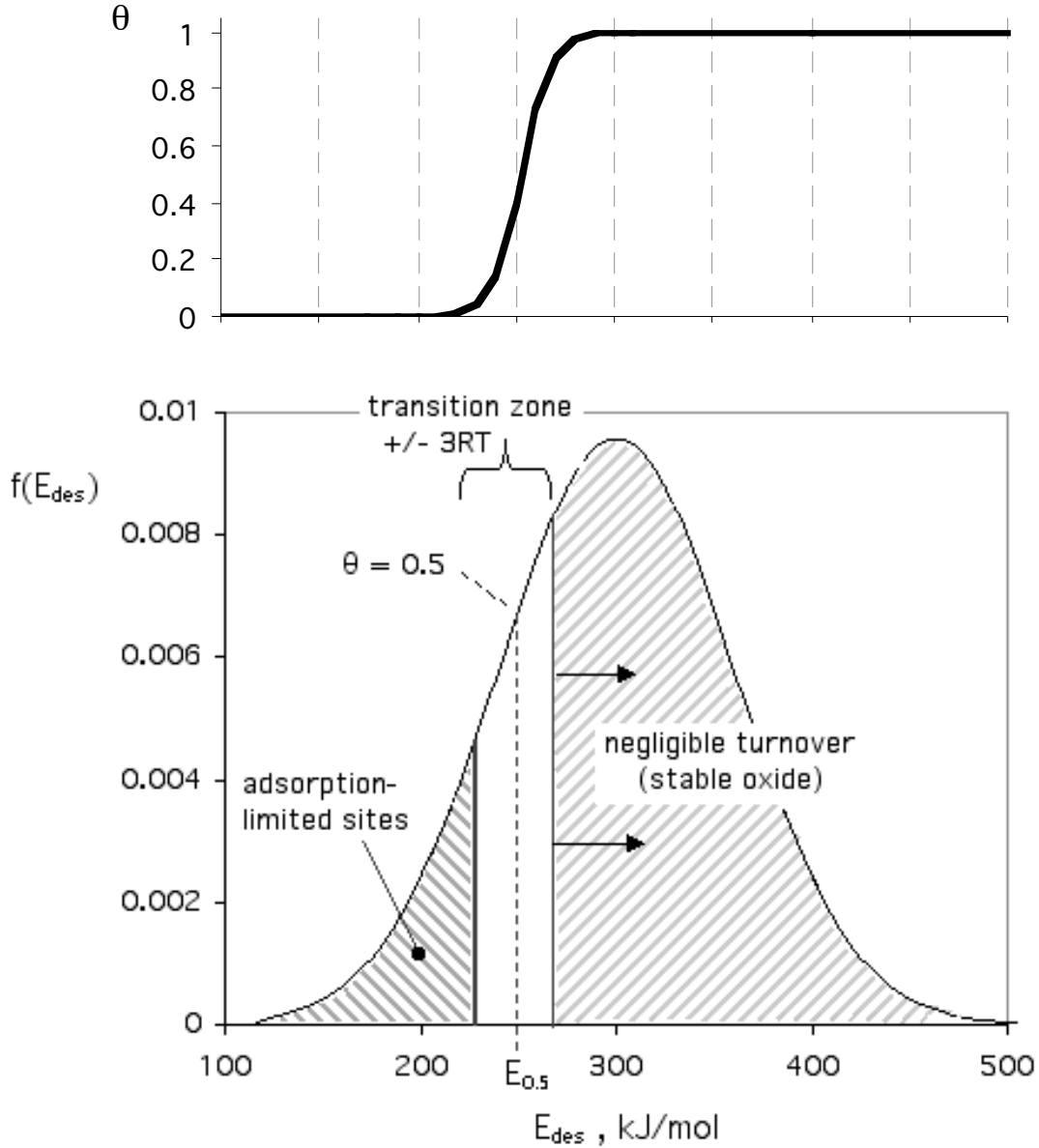


Figure 5.6. Distribution of desorption activation energies originally reported for Sphero carb [11]. The distribution curve is labeled to show the various site populations for an example set of conditions (873 K, 0.1 bar O_2). Under these conditions the sites with 50% coverage have desorption activation energies of 253 kJ/mol ($E_{0.5} = 253$ kJ/mol). The top panel shows coverage, θ , as a function of E_{des} .

for E_{des} when θ is 0.5 (see Fig. 5.6). It can be shown that θ goes from 0.1 to 0.9 over $\Delta E = 4.4RT$ or so the transition zone is conservatively defined as $E_{0.5} \pm 3RT$. The contribution to steady gasification from all sites with E above $E_{0.5} + 3RT$ is negligible, and these constitute the abundant stable oxides observed during low-temperature gasification experiments.

The global gasification reaction is thus dominated by two contributions: a first-order contribution on the bare sites in the low- E_{des} tail and a zeroth order contribution on covered sites that is attenuated rapidly as E_{des} increases due to rapidly decreasing reactivity as the stable oxide regime is approached and entered. In practice the fraction of these covered sites that significantly contributes is often small and the result is high fractional order, as observed experimentally (Fig. 5.1). Finally, since the threshold value, $E_{0.5}$, changes only slowly with oxygen pressure, this physical picture remains unaltered over wide pressure ranges, and persistent fractional order is observed, again in agreement with experiments (Fig. 5.2).

Derivation of an approximate analytical expression for n_{global}

Since the stable oxide does not turn over at a significant rate, there are two components to steady gasification: (1) first-order adsorption-limited reaction on bare sites with $E < E_{0.5} - 3RT$, and (2) mixed-order reaction on partially covered sites in the transition zone: $E_{0.5} - 3RT < E < E_{0.5} + 3RT$. In the limit of large Δ_{des} , the transition zone becomes small relative to the total distribution breadth and can be adequately described as a step function in coverage from 0 to 1 at the threshold value of $E_{0.5}$. This overestimates the rate in the transition zone for both site types, but the errors approximately cancel when the expression is differentiated for reaction order, whose value depends largely on the relative contribution of the two site types to the overall rate. In this limit there are only bare sites ($E < E_{0.5}$) and covered sites ($E > E_{0.5}$) yielding the following two contributions to the overall rate:

$$R_l = A_{ads} e^{(-E_{ads}/RT)} P_{ox} \int_0^{E_{0.5}} f(E_{des}) dE_{des} \quad (13)$$

$$R_0 = \int_{E_{0.5}} f(E_{des}) A_{des} e^{(-E_{des}/RT)} dE_{des} \quad (14)$$

where R_1 is the first-order component on bare sites and R_0 the zeroth order component on the covered sites and the global rate is

$$R_{global} = R_1 + R_0 \quad (15)$$

Differentiation of Eq. 15 together with Eqs. 13, 14 yields, after some algebraic manipulation,

$$\frac{d \ln R_{global}}{d \ln P_{ox}} \equiv n_{global} = \frac{R_1}{R_1 + R_0} \left[\frac{R_0}{R_1 + R_0} \frac{P_{ox}}{RT} \frac{dE_{ads}}{dP_{ox}} \right] \quad (16)$$

The second term containing dE_{ads}/dP_{ox} is difficult to simplify but is small under most practical conditions. Ignoring this term, Eqs. 13, 14, and 16 can be taken together give a working relation for the reaction order. This relation can be greatly simplified by recognizing that the local desorption rate: $A_{des} e^{(-E_{des}/RT)}$ is equal to the local adsorption rate, $A_{ads} e^{(-E_{ads}/RT)} P_{ox}$, at $E_{0.5}$, yielding:

$$n_{global} \approx \frac{1}{1 + (1/A_{<0.5}) \int_{E_{0.5}} f(E_{des}) e^{((E_{0.5} - E_{des})/RT)} dE_{des}} \quad (17)$$

Where $A_{<0.5}$ is the area of the E_{des} distribution below $E_{0.5}$. An even simpler form can be written for very broad distributions where $f(E_{des})$ changes slowly compared to $e^{((E_{0.5} - E_{des})/RT)}$. In this case $f(E_{des})$ is approximated as $f(E_{0.5})$ and simple integration yields

$$n_{global} \approx \frac{1}{1 + RTf(E_{0.5})/A_{<0.5}} \quad (18)$$

where $f(E_{0.5})$ is the height of the distribution at $E_{0.5}$. For the parameters used to generate Fig. 5.6: $f(E_{0.5}) = 0.0065$ mol/kJ, $A_{<0.5} = 0.22$, $T = 873$ K, and Eq. 18 yields $n_{global} = 0.82$ in

good agreement with Eq. 17 ($n_{global} = 0.81$) and in reasonable agreement with the full theory ($n_{global} = 0.78$), which requires numerical solution of Eqs. 7-10 and fitting of the resultant $R_{global} - P_{ox}$ relation with a power law expression.

Application to the Carbon Oxidation Database at T < 1000 K, P > 0.01 Bar

The previous sections demonstrate that surface heterogeneity, whether intrinsic or induced, is capable of explaining the long-standing paradox of power-law kinetics in carbon oxidation. The particular formulation of Haynes[11] is a promising candidate for application to the carbon oxidation database, but the model requires extensive surface characterization, which to date has only been carried out on the model carbon, Spherocarb. The philosophy, however, behind these detailed surface studies on model carbons has always been to identify the correct kinetic *framework*, which can then be extended to other chars in the form of a parameterized engineering model.

The goal of this section therefore is to explore the ability of the Haynes model framework to describe typical data on a range of carbons from the oxidation kinetic database. There is only limited experimental guidance on how best to parameterize the model. Important model parameters most likely to vary from one carbon to the next are the mean and standard deviation of E_{des} and the parameters a and b in Eq. 9 that govern adsorption kinetics. The experiments of Lear[14] show similar temperature programmed desorption spectra for Spherocarb and Loy Yang coal char, with somewhat larger differences in transient chemisorption kinetics. We therefore attempt here to describe the disordered carbon data of Suuberg[4] and Madsen[5] by starting with the Spherocarb parameters and making small adjustments to the adsorption and, if necessary, desorption energy distributions to match the overall rate and pressure dependence.

Figure 5.7a compares Haynes model predictions to the Fig. 5.2a data of Suuberg et al.[4] taken over a factor of 200 in partial pressure. The final parameter set is identical to that for Spherocarb except the parameter "a" in Eq. 9 was reduced from 165 kJ/mol to 152 kJ/mol and the desorption distribution breadth, Δ_{des} , decreased from 60 kJ/mol to 45

kJ/mol. Figure 5.7b shows the results of similar fits to the coal char data of Madsen et al.[5]. These chars have global kinetic parameters that are similar to those for Spherocarb, though the absolute rates differ greatly. In this case adjustments were made only to parameter "a" (Eq. 9) yielding 153 kJ/mol (Spherocarb), 142 kJ/mol (Pitt. coal), and 118 kJ/mol (lignite). All other parameters remain identical to those determined experimentally for Spherocarb. The model successfully predicts slight decreases in global order and activation energy as reactivity increases in the series Spherocarb < Pitt. #8 < Lignite char. The fit is not perfect, but the comparison is very encouraging, since only one parameter was adjusted ("a" in Eq. 9) to fit in essence three data features: the

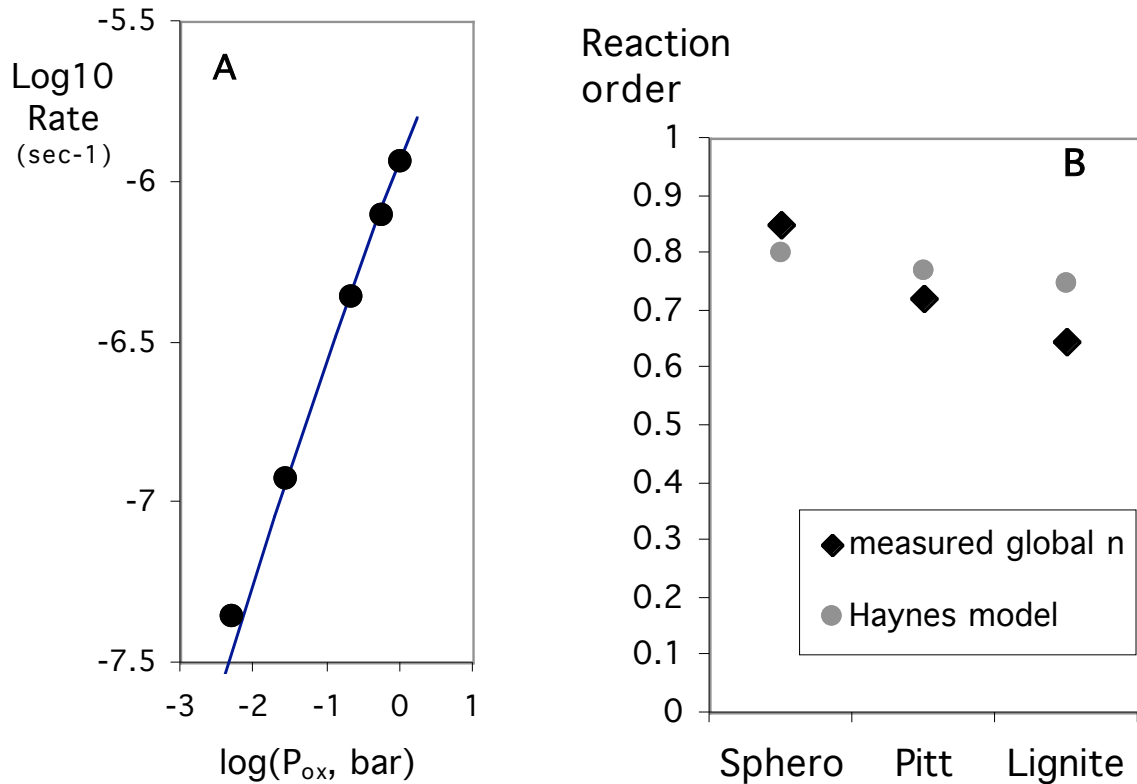


Figure 5.7 Example application of the Haynes model framework to the oxidation kinetics of polymer and coal chars. **A.** The persistent power-law behavior observed by Suuberg et al.[4] on a polymer char is well described by the Haynes model with $a = 139$ kJ/mol in Eq. 9 and $\Delta_{des} = 45$ kJ/mol. **B.** Extension to coal char data of Madsen[5], (see also Hecker et al.[6]) by variation in "a" from 153 to 118 kJ/mol. All other parameters are identical to those determined experimentally for Spherocarb[11].

absolute rate, n_{global} , and the pressure dependence of n_{global} . The Haynes model with only small perturbations to the experimental Spherocharb parameters is clearly capable of describing typical low temperature char oxidation data at and above atmospheric pressure.

Another useful modeling target is the graphite data of Tyler et al.[1], who published a particularly thorough study of the reaction order over a wide pressure range (see Fig. 5.8). The reported reaction orders vary *gradually* with oxygen pressure in a manner that is intermediate between the power-law and Langmuir limiting cases. Lear[14] found that the TPD distribution on Graphon, a highly annealed carbon black, has a similar mean E_{des} to disordered carbon, but is significantly narrower ($\sigma_{E-des} = 35$ kJ/mol vs. 60 kJ/mol for Spherocharb and 65 kJ/mol for Loy Yang coal char[14]). Lear also showed that oxygen chemisorption on Graphon is about 10% of that on Spherocharb, per unit mass of carbon. Therefore we attempted here to fit the Tyler global kinetic data starting with the Spherocharb parameters and varying the distribution width, σ_{des} , and the number of active sites per unit mass.

Figure 5.8 shows the result. The Haynes model can predict the Tyler et al. reaction orders and their gradual shift with pressure. The same parameters give a good prediction of the global activation energy, (258 kJ/mol vs. 268 kJ/mol measured), and an exact match (by design) to the absolute rate. Here two parameters (σ_{E-des} and $N_{Graphon}/N_{Spherocharb}$) were adjusted to fit four data features: n , the pressure dependence of n , E , and the absolute rate, R . The final parameters were $\sigma_{E-des} = 17$ kJ/mol and 0.033 mol-active-sites/kg. The active site number is a factor of 30 below the disordered carbon Spherocharb, which is not unreasonable, while the distribution breadth is significantly smaller than for the disordered chars, as expected. The narrower distribution is responsible for the weak pressure dependence of order (the distribution is not broad enough for full n^{th} -order kinetics) and the generally low orders, which arise from contraction of the low- E_{des} tail, giving a smaller value of $A_{<0.5}$ in Eq. 18 and thus fewer adsorption-limited sites). This fit offers an attractive explanation for the generally lower orders for graphitic carbons relative to disordered carbons in Fig. 5.1 — it is a natural consequence of reduced heterogeneity in these low-defect-density materials.

Chapter 5 Conclusions

A sufficient explanation for the long-standing paradox of persistent, high fractional order in the carbon/oxygen reaction is surface heterogeneity. Simple models of surface heterogeneity, whether intrinsic or induced, predict power-law behavior over wide ranges of partial pressure if the breadth of the activation energy distribution for adsorption and/or desorption is large. The available measurements of desorption activation energy distributions show more than enough breadth for this power-law behavior to be generally expected for non-graphitic carbons, in accordance with experimental observations.

The heterogeneous surface model of Haynes is a promising framework for describing the major features in the low-temperature carbon oxidation database. The Haynes model with minor perturbations to the original parameters determined experimentally for Sphero carb is capable of describing the rates, reaction orders, and pressure dependence of reaction order for several literature datasets on polymer and coal chars, along with the known existence of stable oxide. The Haynes model is also capable of predicting the lower orders and the gradual change in reaction order with pressure for graphitized carbon black, a behavior that is intermediate between power-law and Langmuirian kinetics. The model predicts these features as the direct consequence of the narrower distribution of site energies for the more homogeneous highly annealed carbon forms.

It is impractical to carry out the detailed surface characterization to fully define heterogeneous surface models for each carbon material of technological interest. Such models do provide, however, much needed theoretical underpinning for the commonly used power-law kinetic form, and the Haynes formulation in particular offers a new framework for the development of robust parameterized engineering models for practical application. More work is needed on the oxide oxidation step, $O_2 + C(O) \rightarrow products$ before a comprehensive model is available for application to the literature database. This reaction step is likely to be significant at the lowest temperatures of interest, where its kinetics will be superimposed on the power law behavior described here. The oxide

oxidation step is likely complex, but is nominally first order in O_2 , and its influence may thus provide an explanation for the significant number of unity and near unity orders seen in the literature compilation of Fig. 5.1.

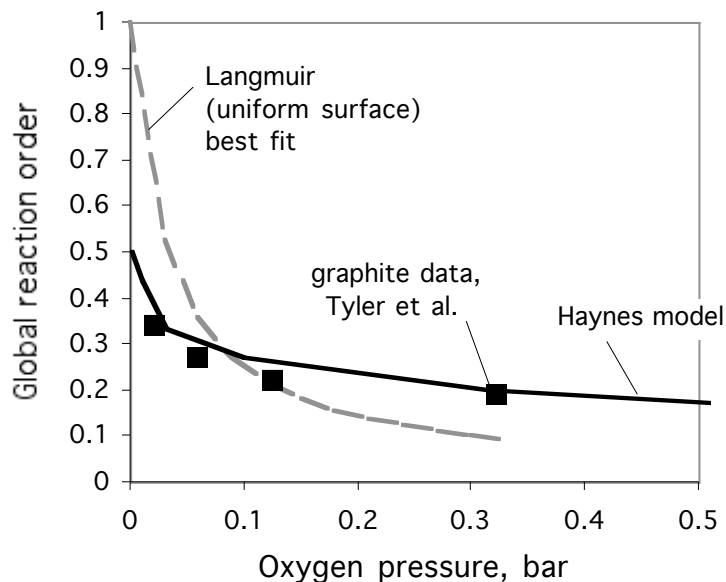


Figure 5.8. Graphite oxidation data of Tyler et al.[1] showing reaction order that varies gradually with pressure (closed diamonds), a behavior that is transitional between the single-site Langmuir form (dashed grey curve) and power-law kinetics. The solid curve gives the predictions from the Haynes model with $\square_{des} = 18$ kJ/mol, and an active site number ratio ($N_{Graphon} / N_{Spherocarb}$ of 1/30). All other parameters were the same as determined experimentally for Spherocarb [11].

Chapter 5 References

1. R.J. Tyler, H.J. Wouterlood, F.R. Mulcahy, *Carbon* 14 (1976) 271-278.
2. Froberg, R.W., Essenhigh, R., *Proc. Comb. Inst.* 17 (1979) 179-187.
3. R.H. Hurt, J.M. Calo, *Combust. Flame*, 125 (2001) 1138-1149.
4. E.M. Suuberg, M. Wojtowicz, J.M. Calo, *Proc. Combust. Inst.*, 22 (1988) 79-87.
5. P.M. Madsen, T.H. Fletcher, W.C. Hecker, *ACS Division of Fuel Chemistry Preprints*, 1, (2001) 318-320.
6. W.C. Hecker P.M. Madsen, M.R. Sherman, J.W. Allen, R.J. Sawaya, T.H. Fletcher, *Energy and Fuels*, 17(2) (2003) 427-432.

7. Q. Zhuang, T. Kyotani, A. Tomita, *Energy and Fuels* 9 (1995) 630-634.
8. Z. Du, A.F. Sarofim, J.P. Longwell, *Energy and Fuels*, 4 (1990) 296-302.
9. S.G. Chen, R.T. Yang, F. Kapteijn, J.A. Moulijn, *Ind. Eng. Chem. Res.* 32 (1993) 2835-2840.
10. M.C. Ma, B.S. Haynes, *Proc. Combust. Inst.* 26 (1996) 3119-3125.
11. B.S. Haynes, *Combust. Flame* 126 (2001) 1421-1432.
12. R.I. Masel, *Principles of Adsorption and Reaction on Solid Surfaces*, (1996) J. Wiley and Sons., New York.
13. B.S. Haynes, T.G. Newbury, *Proc. Combust. Inst.* 28 (2000) 2197-2203.
14. A. E. Lear, Ph.D. Thesis, Department of Chemical Engineering, University of Sydney, 1992.

CHAPTER 6

CHAR COMBUSTION REACTIVITIES FOR A SUITE OF DIVERSE SOLID FUELS

Introduction and Background

Concern over the potential effects of global warming is driving a diversification in solid fuel selection — a shift from almost sole reliance on coal to a broader fuel mix encompassing organic matter of quite diverse origin and composition. To support this effort, comparative studies are needed in which large sets of these diverse alternate fuels are burned under standard conditions chosen to reveal intrinsic fuel-to-fuel differences in each of the fundamental combustion subprocesses: pyrolysis, char oxidation, mineral transformations, and pollutant formation.

For coals, the char combustion subprocess has been extensively studied and reviewed [1-4], and the major reactivity trends have been established through comparative studies employing a range of coals, including studies below 1000K[5-8] and at flame temperatures [9,10]. There are no comparable studies on large sets of alternate fuels, although the recent literature does contain valuable information on individual fuels [11-14] or small sets of fuels of interest in a particular region [15-18]. It is not known if any of the compositional trends and correlations derived from coal studies have relevance to biomass and other alternate fuel types.

The goal of the present work was to measure char combustion reactivities for a large set of traditional and alternative solid fuels under standardized low-temperature conditions, free from the influence of mass- and heat-transfer processes (Zone I). A secondary goal was to identify possible quantitative relationships between char reactivity and parent fuel properties. To gain a deeper understanding of the origin of char reactivity in this data set, the sample suite was augmented by a series of char-forming chemical reagents and model materials that are nearly free of the inorganic contamination that is ubiquitous in practical solid fuels.

Materials and Experimental Procedures

A suite of 31 materials was assembled for this study (see Table 6.1), including 20 solid fuels and 11 organic model materials chosen for their low levels of potentially catalytic inorganic matter. Each of the 31 raw materials was pyrolyzed in a benchtop tube furnace at 700°C for 1 hour using a thin bed of sample spread in an oblong alumina boat, purged with flowing high-purity helium (600 cc/min). Seventeen of the raw materials were also pyrolyzed at 1000°C for 1 hour to investigate the effect of heat treatment temperature. The subsequent chars were crushed and sieved to obtain a 75-106 μm size fraction for study. Because of the enormous reactivity range within this sample suite (over four orders of magnitude), it is not practical to measure all reactivities at a common temperature. Non-isothermal thermogravimetric analysis (TGA) was therefore carried out using a Cahn TG-2141 apparatus fed with dry air (21% oxygen) at 40 cc/min and atmospheric pressure. Char samples of 3-10 mg were spread as a thin bed on a platinum pan to avoid mass- and heat-transfer effects. Time, sample temperature, and mass were continuously recorded as the sample temperature was raised first to 105°C to drive off any moisture, then at 7 K/min to 950°C, at which point complete burnout was achieved for all samples. All reactivity measurements were made in triplicate and the mean values reported.

A subset of 14 of the 700°C chars was chosen for surface area measurements. Some fresh (unreacted) chars exhibit strong molecular sieving behavior in which the nitrogen and carbon dioxide surface areas are grossly different, an effect that is typically eliminated by only slight oxidative conversion [19,20]. For such chars, the proper assignment of area is ambiguous and the nitrogen area of the fresh char may be not at all representative of its values during most of the burnout process. To avoid this problem, chars slated for vapor adsorption measurements were first partially reacted by slow air oxidation in a tube furnace to conversions from 15-35% — close to the 20% at which the reactivity indices were derived (see below). Each of these chars was outgassed for 20 hours at 300°C, followed by measurement of 80-point vapor adsorption isotherms in nitrogen at 77K and in carbon dioxide at 195K, from which surface areas were computed using the BET theory.

Definitions of Standard Reactivity Indices

The non-isothermal TGA profiles were used to extract standard char reactivities reported here in two different but essentially equivalent forms:

1. Critical temperature values, T_{cr} , defined as the temperature at which the combustion rate first equals 0.05 g/min-g-initial-char. Other researchers have reported T_{cr} values [7] defined in a similar manner[†] as a convenient reactivity index that does not require kinetic assumptions.
2. Reactivity values, R , as burning rates in air at a standard reference temperature (T_{ref}) of 500°C, defined as:

$$R \equiv \left[\frac{1}{m} \frac{dm}{dt} \right] e^{\left[\frac{E}{R} \left(\frac{1}{T_{ref}} - \frac{1}{T} \right) \right]} \quad [1]$$

where m , dm/dt , and T are determined at here 20% conversion, daf. The exponential term brings the raw rates to a common temperature for convenient fuel-to-fuel comparison. This temperature normalization was made using an activation energy of 35 kcal/mol (146 kJ/mol), a typical value for Zone I char oxidation [2,8,21,22]. The use of a single activation energy is not a significant disadvantage of this particular reactivity index, because activation energies vary over only a modest range for the low- temperature, disordered chars of interest in this study, and because the standard reference temperature is chosen near the center of the range of actual temperatures, making the temperature correction term inherently small. Indeed there is an excellent correlation between T_{cr} and R as shown in Figure 6.1, so either index may serve as a valid expression of the relative reactivity of different chars in the sample suite.

Results

Standard reactivities as T_{cr} and/or R values are presented in Table 6.1 and Figs. 6.2 and 6.3. Reactivities of the 1000 °C chars are presented in Figure 6.3. Surface areas are presented in Table 6.1 and are cross-plotted against reactivity in Figure 6.4. The nitrogen and carbon dioxide surface areas of the chars at 20% conversion are generally similar, indicating the absence of strong molecular sieving effects, which would have complicated the interpretation.

Table 6.1 Sample Suite of Solid Fuels and Organic Model Substances: Properties^b and Char Reactivities

Sample	ash	VM	C	H	O	N	S	Al	Ca	Fe	K	Mg	Na	Ni	Si	V	N ₂ Area ^c	CO ₂ Area ^c	T _{cr} ^j	log ₁₀ R ^f 700°C	log ₁₀ R ^f 1000°C
	dry %	dry %	daf %	ppmw	ppmw	ppmw	ppmw	ppmw	ppmw	ppmw	ppmw	ppmw	m ² /g	m ² /g	K	sec ⁻¹	sec ⁻¹				
Microcrystalline ^a Cellulose	0.05	90.71	41.86	6.42	51.68	0.02	0.02	<10	<5	<10	<40	<10	59	<1	12	<1	547.0	645.1	900	-4.35	-4.91
Synthetic RDF	19.84	71.32	41.95	6.46	51.55	0.02	0.02	23600	120	74	<40	44	253	1	62400	<1	335.5	353.3	905	-4.41	-4.84
Sucrose, C ₁₂ H ₂₂ O ₇ ^a	-	-	42.08	6.50	51.40	<0.01	<0.01	<100	<100	<100	<100	<100	<100	<100	<100	<50	592.1	638.0	900	-4.35	-4.58
Dried Sludge	0.06	76.36	42.37	6.54	48.01	3.05	0.03	67	983	289	480	218	452	<1	256	<1	-	-	838	-3.48	-
Corn Stalk	3.24	74.77	43.99	6.28	48.93	0.70	0.09	106	1900	130	15300	1600	41	<1	2380	<1	213.5	327.1	701	-1.70	-2.67
Wheat Straw	9.43	68.76	44.23	6.39	48.63	0.60	0.15	70	1720	52	15500	1140	72	<1	7880	<1	258.4	320.5	716	-2.12	-3.34
Rice Hulls	16.16	63.64	44.59	6.36	48.70	0.29	0.05	52	650	170	7880	400	72	7	71800	<1	-	-	751	-2.69	-
Hardwood	0.57	80.19	45.80	6.20	47.82	0.15	0.03	166	1470	270	1450	380	71	<1	954	<1	-	-	781	-3.07	-3.18
Bagasse Sachurum	3.82	78.43	45.92	6.26	47.60	0.17	0.05	3100	648	3700	1300	440	206	15	8770	8	-	-	873	-3.98	-
Pinus Radiata	0.22	79.44	46.05	6.31	47.58	0.04	0.02	170	408	240	738	150	77	<1	910	<1	-	-	845	-3.80	-
Softwood	0.46	76.14	46.14	6.32	46.01	1.48	0.05	220	700	250	997	217	1590	<1	745	<1	-	-	781	-3.08	-
Populus Deltoides	0.63	80.46	46.43	6.11	47.32	0.08	0.06	<10	2450	295	2360	300	68	<1	644	<1	434.3	458.0	762	-2.82	-
C ₂₂ H ₃₈ O ₇ ^{a,g}	-	-	63.73	9.16	26.85	<0.01	0.25	<100	<100	<100	<100	<100	<100	<100	<100	<50	386.8	504.2	912	-4.51	-5.05
Beulah (ligA) ^d	-	-	73.14	4.46	20.59	1.00	0.82	6000	18000	6100	500	5600	6600	0	5000	14	161.1	320.2	730	-2.44	-3.83
Polycarbon. Resin ^a	-	-	75.48	5.69	18.81	<0.01	0.01	<100	<100	<100	<100	<100	<100	<100	<100	<50	-	-	848	-3.85	-
Phenol-for. Resin ^a	-	-	77.76	5.96	16.22	0.05	<0.01	<100	<100	<100	<100	<100	<100	<100	<100	<50	-	-	886	-4.20	-4.81
Illinois #6 (hvCb) ^d	-	-	78.11	5.44	9.73	1.32	5.39	16000	5900	23000	2500	800	800	14	37000	3	-	-	823	-3.59	-4.46
Rosebud (subB) ^d	-	-	78.19	4.22	15.21	1.05	1.33	13000	13000	8500	500	2600	1200	<1	23000	2	-	-	765	-2.90	-
Koonfontain (mvb)	12.65	26.47	78.72	4.78	13.79	1.99	0.71	22600	6330	2630	689	1940	278	8	25400	16	-	-	904	-4.08	-
C ₃₀ H ₁₈ O ₄ ^{a,h}	-	-	79.69	4.19	16.05	0.01	0.06	<100	<100	300	<100	<100	100	<100	500	<50	-	-	847	-3.80	-
Fluid Coke	0.05	6.17	87.38	2.41	5.14	2.57	2.50	37	102	307	<10	20	136	476	193	477	-	-	951	-4.66	-5.07
Tire Bits	-	-	87.63	7.57	2.55	0.39	1.87	2200	2700	1500	500	600	400	200	5000	<50	-	-	931	-4.53	-4.89
Delayed Coke	0.05	11.04	87.80	3.96	1.41	1.43	5.40	17	47	213	<10	11	52	198	67	501	-	-	911	-4.39	-
Pocahontas (lvb) ^d	-	-	89.87	4.90	3.31	1.14	0.78	6000	600	7000	400	800	500	7	7000	9	113.5	136.2	974	-4.94	-
Lykens Valley (an) ^d	-	-	90.33	4.01	4.30	0.80	0.56	18000	400	3300	4600	600	200	17	29000	21	324.8	384.8	961	-4.88	-
Lei Yang (an)	22.35	5.64	90.47	2.01	5.86	0.72	0.93	27800	6250	6900	5790	1440	2730	19	46700	41	169.8	197.2	975	-5.01	-5.15
Petroleum Pitch ^a	-	-	94.50	5.09	0.19	0.00	0.22	-	-	-	-	-	-	-	-	-	-	-	974	-4.97	-
AR-HP Pitch ^{a,e}	-	-	95.13	4.87	0.00	0.00	0.00	-	-	-	-	-	-	-	-	-	141.1	175.1	966	-4.90	-5.76
AR-MP Pitch ^{a,e}	-	-	95.13	4.87	0.00	0.00	0.00	-	-	-	-	-	-	-	-	-	132.5	161.6	964	-4.90	-5.97
Graphite Powder ^a	-	-	96.30	0.38	<0.10	0.87	2.45	100	100	500	<100	<100	<100	100	200	280	-	-	1052	-5.54	-5.55
Graphite Rods ^{a,i}	-	-	100.0	0.00	0.00	0.00	0.00	1	2	1	0	0	1	0	7	0	5.05	6.15	1201	-6.39	-6.15

^a model materials selected for low amounts of potentially catalytic impurities

^b elemental analyses performed by Huffman Laboratories (Golden, CO) unless otherwise noted

^c multi-point BET surface areas of chars (He, 1 hr, 700°C) at 20% conversion (daf)

^d elemental analysis reported by Department of Energy Coal Bank at Penn State data sheets

^e synthetic mesophase pitches from naphthalene polymerization, high (HP) and medium (MP) grades; elemental analysis reported by manufacturer, Mitsubishi Gas Chemical

^f standard reactivity at 500°C in air of chars prepared at 700°C or 1000°C, as labeled

^g L-ascorbic acid 6-palmitate

^h 2,2'-dimethyl-1,1'-bianthraquinone

ⁱ elemental composition reported by vendor (Aldrich)

^j critical temperatures for the chars prepared at 700 °C

Trends in reactivity with fuel type are most easily identified using Figure 6.2, where we see that reactivities of the 700°C chars vary by almost 5 orders of magnitude under identical conditions. Considering only the practical solid fuels, the reactivities still span over 3 orders of magnitude, from high-rank coal chars (lowest reactivity) to corn stalk chars (highest reactivity). The 1000°C chars in Figure 6.3 show a similar data pattern, but with just over 3 orders of magnitude total variation in reactivity. A strong correlation is seen between reactivity and carbon (daf) content of the vitrinite-rich coals, as been observed previously [5,6,10]. This trend has no relevance for the biomass fuels, however, which cluster closely in composition (40%-50% daf carbon), while their reactivities span almost 3 orders of magnitude. Carbon content is a very poor indicator of biomass reactivity. By analyzing the data in Table 1 it can be further stated that no organic composition variable (C,H,O,N,S) provides enough information for making even a crude estimate of biomass char reactivity.

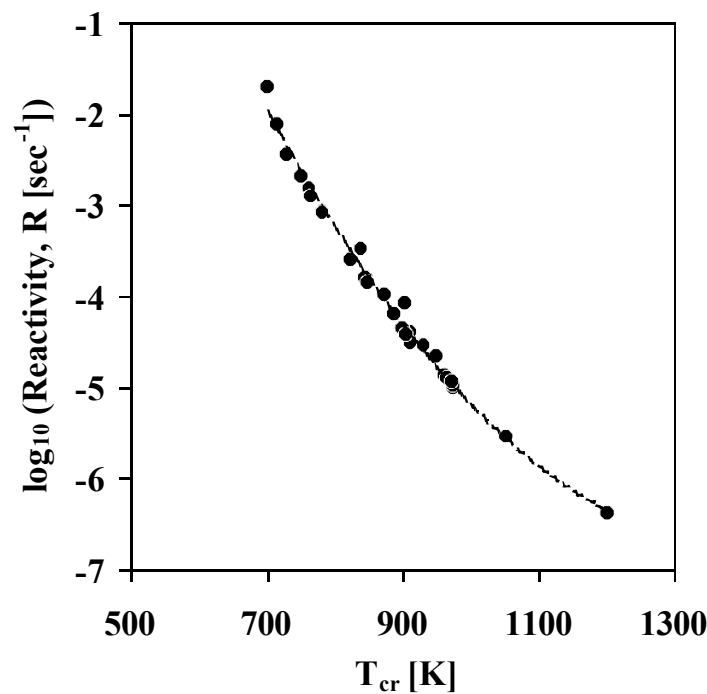


Figure 6.1. Correlation between the two reactivity indices reported in this work: critical temperatures, T_{cr} , and standard reactivities at 500 °C in air, R . For interconversion between the two indices one can use the following empirical expression: $\log_{10}R = -12.6 - 2.77 \cdot 10^{-2}T_{cr} + 9.97 \cdot 10^{-6}T_{cr}^2$

[†] Charpenay et al.[7] use a combustion rate of 0.065 min⁻¹ to define T_{cr} , but some samples in the present study never achieved rates this high at the chosen heating rate and gas environment

It is quite notable in Figure 6.2 that the model materials, chosen for their lack of inorganic impurities, all have reactivities that lie in a relatively narrow band in the low reactivity region. These non-catalytic char reactivities show almost no composition dependence between 40% and 80% carbon (daf), but do fall away above 90% carbon (daf). Overall, the patterns revealed in Figure 6.2 strongly suggest that organic composition is secondary to other factors determining reactivity in the char of precursors below 80% carbon (the majority of practical solid fuels). The next section examines reactivity/property relations in more detail.

Reactivity / Property Relations

The goal of this section is to investigate quantitative relationships between reactivity and properties of the parent material, focusing on the larger data set of 700°C chars. Statistical software (SPSS Inc.) used for multivariate linear regression revealed positive correlations with statistical significance between reactivity and three properties: wt-% K, Ca, and Mg. In addition a negative correlation was found between reactivity and wt-% carbon (daf). A simple linear correlation based on these four variables, however, does not provide an adequate description of the data set. Such blind statistical analyses are easy to perform, but make no use of insights gained from decades of research on combustion and fuel chemistry. Therefore, we pursued a hybrid approach that combines statistical analysis with chemical insights derived from literature data on different fuel classes. We begin by expressing the reactivity as a sum of two independent contributions:

$$R = R_{carb} + R_{cat} \quad [2]$$

where R_{carb} represents reaction on non-catalytic (carbon) active sites[23] and R_{cat} represents reaction on catalytic active sites [22], assumed to be independent, parallel processes. The existence of the narrow model substance band on Figure 6.2 suggests that variations in R_{carb} are only a small part of the total reactivity variation for fuels up to up to 80% carbon (daf) content. We therefore, as an approximation, define a single, non-catalytic baseline reactivity shown in Figure 6.2 that establishes the model parameter R_{carb} as a function of the parent material carbon content. This same line implicitly

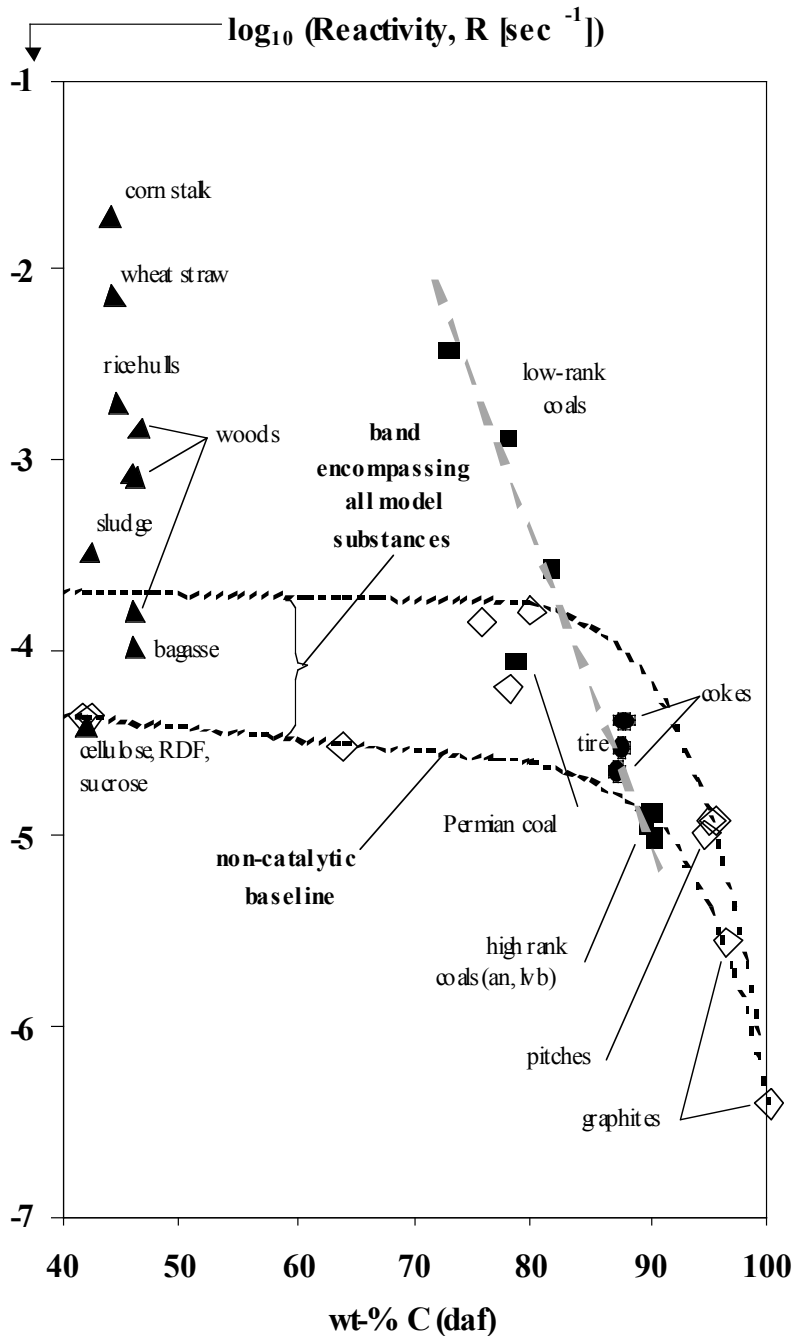


Figure 6.2 Master plot of measured reactivities for chars prepared at 700 °C from the 31 precursors plotted as the percentage carbon content of the parent material (daf). The thick dashed line shows a strong correlation between reactivity and rank among vitrinite-rich coals, as reported in other oxidation kinetic studies[5,6,10]. The dotted lines define a relatively narrow region that encompasses all of the model materials that are nearly free of potentially catalytic inorganic matter. The lower dotted line is taken as a non-catalytic baseline in the model discussed in the section on reactivity / property relations.

defines R_{cat} as the difference between the measured reactivity and R_{carb} , the non-catalytic baseline value.

The primary challenge is to investigate relations between the catalytic residual, R_{cat} , and fuel properties. Studies involving demineralization and/or direct catalyst addition clearly reveal which elements are intrinsically catalytic for char oxidation: Group I metals, Group II metals, and many transition metals including V, Ni, and Fe, which have a particular importance in some solid fuels [5,22,24-27]. A spliced empirical relation for the non-catalytic baseline is:

$$\log_{10}R_{carb} = -4.1 - 6.25 \cdot 10^{-3}(\text{wt-\% C}), \text{ for wt-\% C} \leq 80$$

$$\log_{10}R_{carb} = -4.52 - 2.11 \cdot 10^{-7} \exp[0.16(\text{wt-\% C})], \text{ for wt-\% C} > 80$$

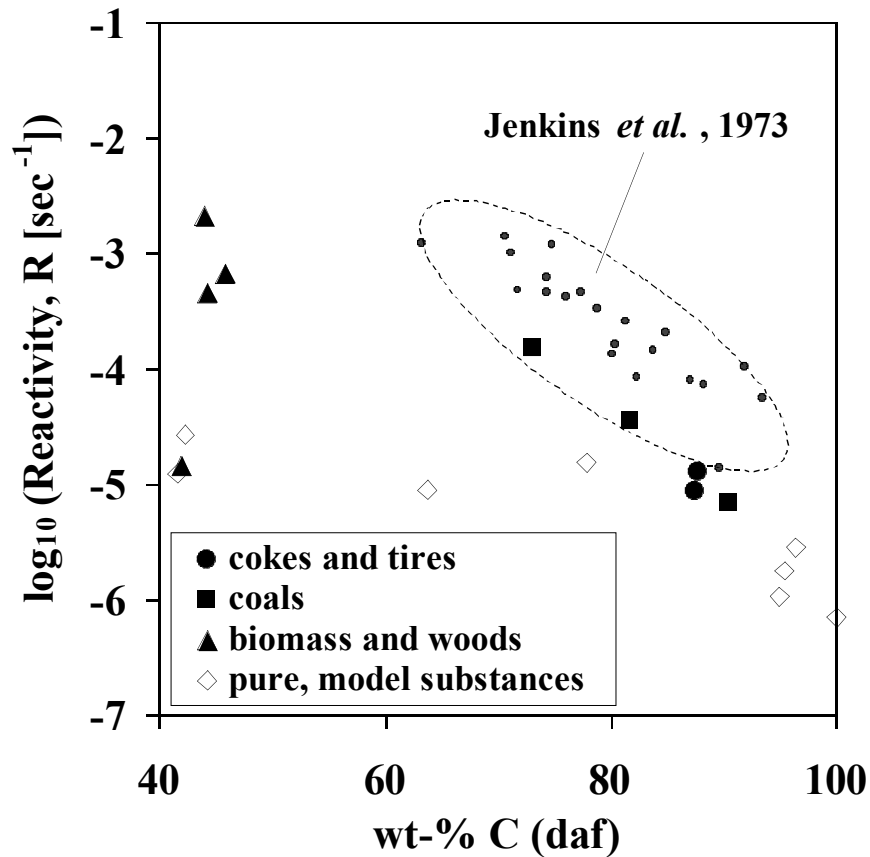


Figure 6.3 Master plot of measured reactivities for chars prepared at 1000 °C from a 17-sample subset of the 31-sample suite. The absolute reactivities are generally lower, but the fuel-to-fuel differences fall in a pattern very similar to the 700 °C chars in Figure 6.2. Literature data from Jenkins et al.[5] on coal chars prepared under similar conditions is shown for comparison.

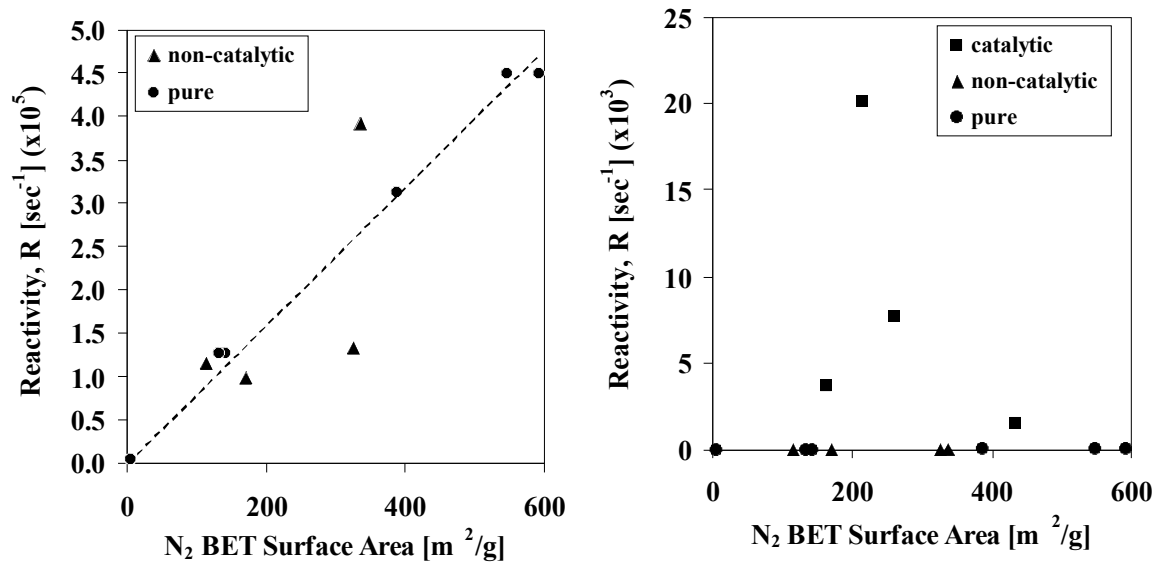


Figure 6.4 Cross plot of reactivity vs. total char surface area (N₂ BET) for pure and noncatalytic materials (left hand side) and for all samples (right hand side). Circles (pure materials) are the nearly-inorganic-free model substances from Table 1; Triangles (non-catalytic materials) are samples containing significant amounts of inorganic matter, but predicted by dispersion arguments to react in a primarily non-catalytic mode (see section on reactivity/ property relations).

Another key consideration is catalyst dispersion, or particle size, which is expected to vary greatly across the spectrum of solid fuels. Although dispersion is continuum variable, one can consider two important limiting cases: (1) *granular dispersion*—particulate matter of supramicron dimension arising from extraneous matter or bulk additives in the fuels, and (2) *nanophase dispersion* — finely dispersed particulate matter of submicron dimensions in chars originating from nanophase or atomically dispersed metals in the parent materials that have partially sintered during carbonization [22]. This highly active material may originate as dissolved salts in plant water, as cations exchanged on carboxylic sites, or as organometallic compounds with essential function (e.g. chlorophyll, porphyrins). Granular material has low catalytic activity by virtue of its low surface area [28], which suggests the relation:

$$R_{cat} = \alpha(K_{nano}) + \alpha(Ca_{nano} + Mg_{nano}) + \beta(V_{nano}) \quad [3]$$

Here M_{nano} indicates the wt-fraction (ppmw) of the nano-dispersed or atomically dispersed form of catalytic metal, M , present in the parent fuel, and α , β , and γ are specific activity coefficients to be determined from statistical analysis of the data. Although Na, Ni, and Fe are known catalysts for char oxidation [26,29], they are not observed to make statistically significant contributions to reactivity in this particular sample set and thus cannot be included in Eq. [3]. The alkaline earth metals are grouped together because our statistical analysis revealed a strong cross-correlation, making any attempt to distinguish the separate effects of Ca and Mg statistically meaningless. Studies employing metal addition have reported similar specific activities for Ca and Mg [26], so their linear combination here with equal weight is a useful approximation.

Before α , β , and γ can be determined, specific rules are needed for estimating the degree of catalyst dispersion in the various fuel classes. In coals, mineral matter is a combination of granular material and atomically dispersed material [30,31], with the major source of atomically dispersed matter in the form of cations exchanged on carboxylic sites [22,31]. The compilation of literature data in Figure 6.5 shows the carboxylic site density is strongly dependent on coal rank. For the hybrid chemical/statistical model we use the correlation shown in that figure to estimate carboxylic site density from wt-% carbon (daf) and carry out a stoichiometric calculation to determine what fraction of the K, Ca, and Mg in the sample is needed to saturate those -COOH sites. This simple two-step correlative technique gives a reasonable estimate of K_{nano} , Ca_{nano} , and Mg_{nano} for use in Eq. [3].

Dispersion of metals in biomass is also a mixture of granular and atomically dispersed forms [32-35]. In most plants, however, potassium salts are essential nutrients, and a high fraction of the potassium (80-90%) is either water soluble or ion-exchangeable [32,33,35,36]. Most calcium also tends to be water soluble or ion-exchangeable, indicative of high dispersion. An exception is sugar cane bagasse, which is washed during processing and has lost soluble salts [33,35]. For purposes of the model we take the group I and II metals in biomass to be finely dispersed with the exception of bagasse in which the remaining matter is taken to be primarily granular. For the non-biomass

alternate fuels, we take the inorganic components in tire fuel to be granular, while the vanadium in cokes is taken to be nano-dispersed, since it originates as atomically dispersed material within porphyrin structures in petroleum [37].

The preceding set of dispersion rules, along with Eqns. [2] and [3], the baseline function in Figure 6.2, and the carboxylic correlation in Figure 6.5, define the hybrid chemical/statistical model. Application of the model to our data set leads to the final correlation and the optimal least-squares values of β , γ , and δ shown in Figure 6.6. The now complete hybrid model provides a link between parent fuel elemental composition and char reactivity at 500°C in air for chars prepared at 700°C from arbitrary and diverse organic precursors.

It is clear from this analysis that catalysis plays a dominant role in the low-temperature reactivity of chars prepared at 700°C. Through examination of the data patterns in Figure 6.3, this same conclusion appears to hold for the chars prepared at 1000°C. Using the final values of β , γ , and δ as sensitivity coefficients, it can be stated that as little as 44 ppmw of nano-dispersed potassium or 270 ppmw of nano-dispersed Ca or Mg is sufficient for the catalytic component of reactivity to exceed the non-catalytic component for materials below 80 wt-%-carbon (daf). With these sensitivities it is difficult to rule out catalytic effects in all but the most pure materials. Indeed, the ICP sensitivity limits for some of the nearly pure model materials are 100 ppmw, so residual catalysis may even be important for some of these compounds, such as $C_{30}H_{18}O_4$ and polycarbonate resin, which lie in the upper region of the model substance band in Figure 6.2. Among the practical solid fuels, only the very highest rank coals (with no -COOH sites) are adequately approximated as non-catalytic. Previous studies employing acid demineralization have also suggested that catalytic effects are significant for most coals[5], although questions have often been raised about collateral effects of strong acids on the organic matrix. The present work reaches the same conclusion by statistical inference from reactivity data without the need for aggressive mineral solvents.

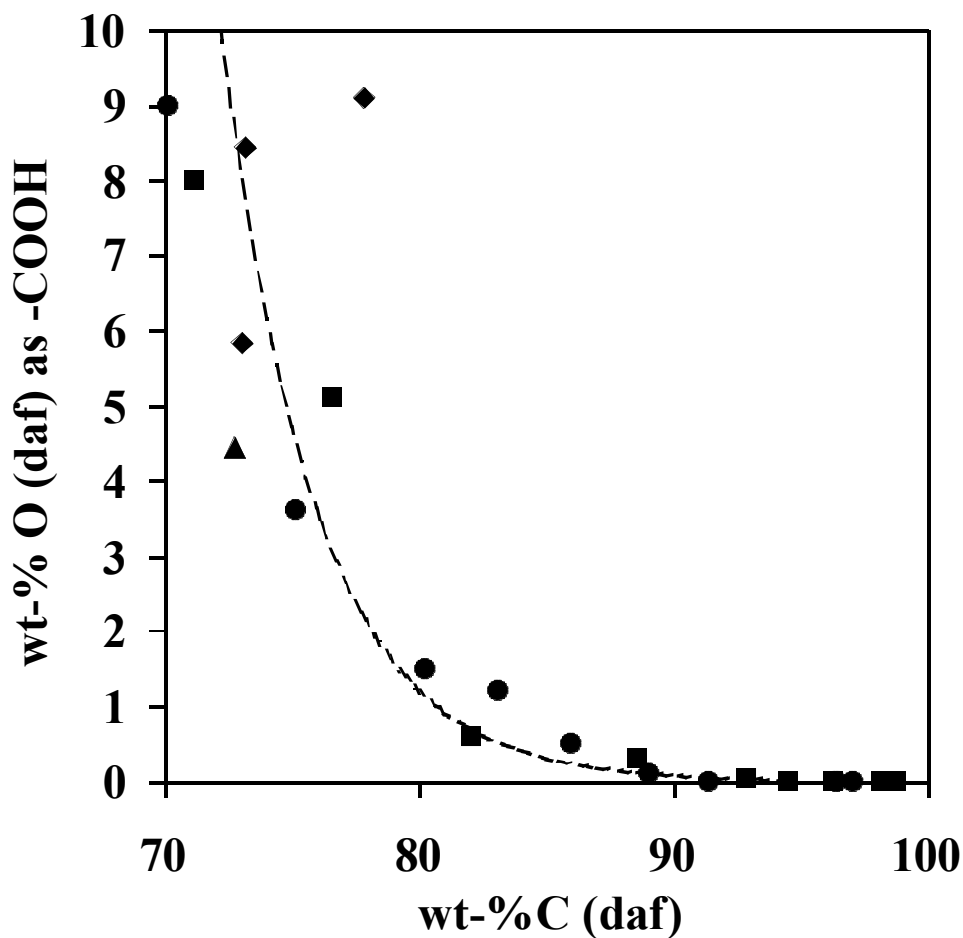


Figure 6.5 Compilation of literature data on the abundance of carboxylic groups in coals of various rank. Sources: circles are data from Ihnatowicz in [38], diamonds are data from Morgan and Jenkins [31], squares are data from Blom in [38], and triangles are data from Otake and Walker [39]. The fitted curve for use in the hybrid chemical/statistical model is: $(\text{wt-\% O as -COOH}) = 3.051 \cdot 10^{-9} \exp[-0.2706 \text{ wt-\% C (daf)}]$ for $\text{wt-\% C} < 90$. Above 90 wt-% C, -COOH site density is taken to be 0 in the model.

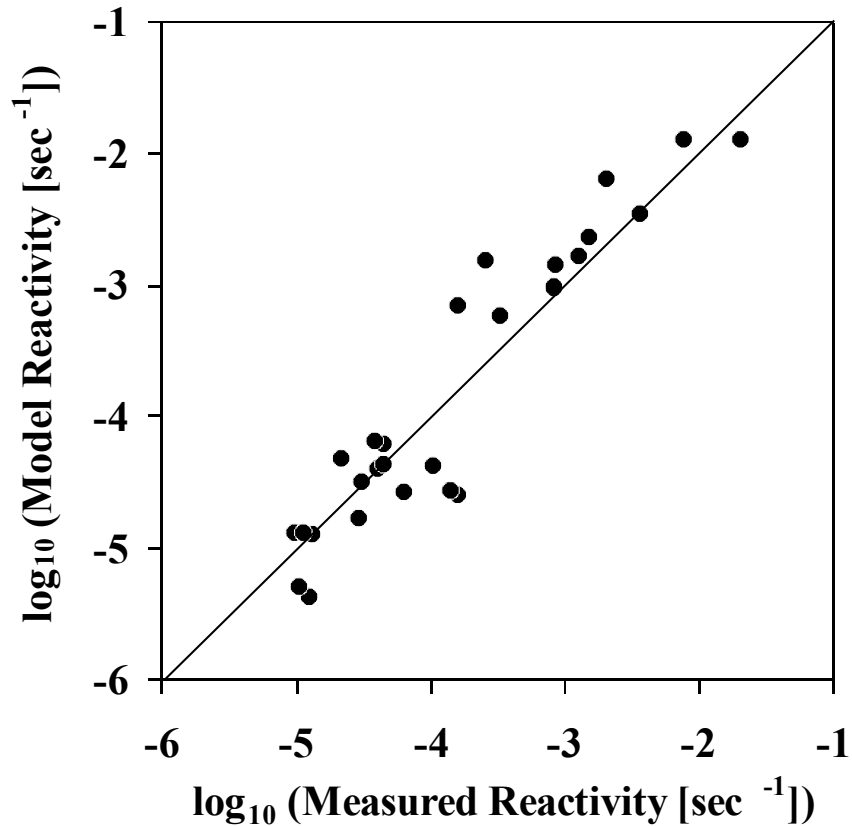


Figure 6.6 Comparison of measured reactivities with reactivities given by the hybrid chemical/statistical model. The plot contains every solid fuel and model material listed in Table 1 except graphites (which cannot be meaningfully described as 700 °C chars) and the Permian southern hemisphere coal (for which Figure 6.6 does not contain relevant data on carboxylic sites). The model reactivity is equal to:

$$R = R_{carb} + \alpha(K_{nano}) + \alpha(Ca_{nano} + Mg_{nano}) + \alpha(V_{nano})$$

where R_{carb} is the baseline function in Figure 6.2, $\alpha = 7.9 \cdot 10^{-7}$, $\alpha = 1.3 \cdot 10^{-7}$, and $\alpha = 3.1 \cdot 10^{-8}$, where the nano or atomically dispersed metals are measured in ppmw of the parent fuel.

Chapter 6 Conclusions

1. Char combustion reactivities at 500 °C in air from a diverse set of fuels and organic model compounds vary over 4 orders of magnitude when chars are prepared at 700 °C and over 3 orders of magnitude when chars are prepared at 1000 °C. Reactivities correlate poorly with organic elemental composition and poorly with char surface area.
2. Specially-acquired model materials with minute amounts of inorganic matter exhibit low reactivities that fall in a narrow band as a function of wt-% carbon. Reactivities in this sample subset correlate reasonably well with total char surface area.
3. A hybrid chemical/statistical model explains most of the observed reactivity variation based on four variables: the amounts of nano-dispersed K, nano-dispersed (Ca+Mg), elemental carbon (wt-% daf), and nano-dispersed vanadium, listed in decreasing order of importance. Catalytic effects play a very significant role in the oxidation of most practical solid fuel chars. Some degree of reactivity estimation is possible using only elemental analyses of parent fuels, but only if correlative techniques make use of the existing body of knowledge on the origin, form and dispersion of inorganic matter in various fuel classes.

Chapter 6 References

1. Essenhigh, R.H., in *Chemistry of Coal Utilization, Second Supplementary Volume* (M.A. Elliot, ed.), Wiley, New York, 1981, p. 1153.
2. Smith, I.W., *Fuel* 57:409 (1978).
3. Miura, K., Hashimoto, K., and Silveston, P.L., *Fuel* 68:1461 (1989).
4. Williams, A., Pourkashanian, M., Jones, J.M., *Proc. Comb. Inst.* 28:2141 (2000).
5. Jenkins, R.G., Nandi, S.P., and Walker Jr., P. L., *Fuel* 52:288 (1973).
6. Fung, D.P.C., and Kim, S.D., *Fuel* 63:1197 (1984).

7. Charpenay, S., Serio, M.A., and Solomon, P.R., *Proc. Comb. Inst.* 24:1189 (1992).
8. Zolin, A., Jensen, A., Pederson, L.S., Dam-Johansen, K., and Tørslev, P., *Energy Fuels* 12:268 (1998).
9. Field, M.A., *Combust. Flame*, 14:237 (1970).
10. Hurt, R.H., and Mitchell, R.E., *Proc. Comb. Inst.* 24:1243 (1992).
11. Luo, M., and Stanmore, B., *Fuel* 71:1074 (1992).
12. Werther, J., and Ogada, T., *Progress in Energy and Combustion Science* 25:55 (1999).
13. Zheng, G., and Kozinski, J.A., *Fuel* 79:181 (2000).
14. Zolin, A., Jensen, A., Jensen, P.A., Frandsen, F., Dam-Johansen, K., *Energy and Fuels* 15:1110 (2001).
15. Devi, T.G., and Kannan, M.P., *Energy & Fuels* 15:583 (2001).
16. Ganesh, A., Grover, P.D., and Iyer, P.V.R., *Fuel* 71:889 (1992).
17. Di Blasi, C., Buonanno, F., and Branca, C., *Carbon* 37:1227 (1999).
18. Marcilla, A., García-García, S., Asensio, M., and Conesa, J.A., *Carbon* 38:429 (2000).
19. Aarna, I., and Suuberg, E.M., *Proc. Comb. Inst.* 27:2933 (1998).
20. Adams, K.E., Glasson, D.R., and Jayaweera, S.A.A., *Carbon* 27:95 (1989).
21. Suuberg, E.M., Wojtowicz, M., Calo, J.M., *Proc. Comb. Inst.* 24:79 (1988).
22. Radovic, L.R., Walker, Jr., P.L., and Jenkins, R.G., *Fuel* 62:209 (1983).
23. Radovic, L.R., Walker, P.L.Jr., Jenkins, R.G. *Fuel*, 62:849 (1983).
24. Cope, R.F., Arrington, C.B., and Hecker, W.C., *Energy & Fuels* 8:1095 (1994).
25. Haykiri-Açma, H., Ersoy-Meriçboyu, A., and Küçükbayrak, S., *Thermochimica Acta* 362:131 (2000).
26. McKee, D.W., in *Chemistry and Physics of Carbon (Volume 16)* (P.L. Walker, Jr. and P.A. Throver, Eds.), Marcel Dekker, New York, 1981, p.1.
27. Devi, T.G., and Kannan, M.P., *Fuel* 77:1825 (1998).
28. Tomita, A., Mahajan, O.P., Walker, Jr. P.L., *ACS Fuel Chem. Preps*, 22:4 (1977).
29. Zhang, D.-K., and Poeze, A., *Proc. Comb. Inst.* 28:2337 (2000).

30. Baxter, L.L., Mitchell, R.E., and Fletcher, T.H., *Combustion and Flame* 108:494 (1997).
31. Morgan, M.E., Jenkins, R.G., and Walker, Jr., P.L., *Fuel* 60:189 (1981).
32. Epstein, E., *Mineral Nutrition of Plants: Principles and Perspectives*, Wiley and Sons, New York, 1972.
33. Jenkins, B.M., Baxter, L.L., Miles, Jr., T.R., and Miles, T.R., *Fuel Processing Technology* 54:17 (1998).
34. Dayton, D.C., Jenkins, B.M., Turn, S.Q., Bakker, R.R., Williams, R.B., Belle-Oudry, D., and Hill, L.M., *Energy and Fuels* 13:860 (1999).
35. Baxter, L.L., Miles, T.R., Miles, Jr., T.R., Jenkins, B.M., Milne, T., Dayton, D., Bryers, R.W., and Oden L., *Fuel Processing Technology* 54:47 (1998).
36. Jensen, P.A., Frandsen, F.J., Dam-Johansen, K., and Sander, B., *Energy Fuels* 14:1280 (2000).
37. Marquez, N., Ysambertt, F., De La Cruz, C., *Anal. Chim. Acta* 395:343 (1999).
38. Krevelen, D.W. and Schuyer J., *Coal Science: Aspects of Coal Combustion*, Elsevier, Princeton, NJ, 1957, p. 217.
39. Otake, Y., and Walker, Jr., P.L., *Fuel* 72:139 (1993).

CHAPTER 7

GASIFICATION KINETICS IN PRESSURIZED CO₂

Background

As indicated previously, several technologies, such as Integrated Gasification Combined Cycle (IGCC), Pressurized Fluidized Bed Combustion (PFBC) and Pulverized Coal Injection (PCI), have been identified as the most viable alternatives for the clean utilization of coal due to the use of combined cycles (Smoot and Smith, 1985; Smoot, 1998). These technologies operate at elevated pressure (e.g., 10-15 atm for PFBC, 15-25 atm for IGCC, and less than 5 atm for PCI). High pressure operation results in increased coal throughput, reduction in pollutant emissions, and enhancement of reactivity (Takematsu and Maude, 1991; Harris and Patterson, 1995). Here we focus specifically on the kinetics of CO₂ gasification at elevated pressures.

The carbon-CO₂ reaction has been extensively investigated due to its importance in the overall carbon gasification scheme. The gasification process first involves the chemisorption of oxygen on the carbonaceous surface, followed by subsequent desorption as carbon oxides. There have been a number of experimental studies on the mechanism of CO₂ gasification (Mentser and Ergun, 1973; Blackwood and Ingeme, 1960; Walker, 1986; Reif, 1952). Perhaps the most widely accepted mechanism in the literature for the carbon-CO₂ reaction at low pressures was proposed by Ergun and Mentser (1973). It is believed that CO₂ adsorption on the surface of the char, followed by CO desorption are the principal steps, *i.e.*



where C(O) is a carbon-oxygen surface complex, and C_f is a vacant carbon active site. Under pseudo-steady-state conditions, in an atmosphere of CO₂, reaction [R.1] is driven to the right, populating an active site and producing one CO molecule. The second step is the desorption of the carbon-oxygen surface complex to yield another molecule of CO, thereby, generating a new active site, and completing the overall stoichiometry:



The carbon-CO₂ gasification reaction is affected by a number of factors. Among them, CO₂ partial pressure plays an important role in determining the rate. It is widely accepted

that the pressure dependence on the gasification rate at low pressure can be adequately expressed by the well-known *Langmuir-Hinshelwood* type expression, whether the reaction is catalyzed (Kapteijn and Moulijn, 1983) or not (Mentser and Ergun, 1973), *i.e.*,

$$r = \frac{k_1 C_t P_{CO}}{1 + \frac{k_1}{k_2} P_{CO} + \frac{k_{-1}}{k_2} P_{CO}} \quad (1)$$

where C_t is the total number of active sites, and P_{CO} and P_{CO_2} are the partial pressures of CO and CO_2 , respectively.

The effect of CO_2 pressure on the gasification rate has been investigated by a number of workers (Dutta *et al.*, 1977; Harris and Smith, 1989; Ye *et al.*, 1998; Nozaki *et al.*, 1992; Zhang and Calo, 1996). However, the overall apparent reaction order for the carbon- CO_2 reaction still remains a matter of controversy. Most workers report that the gasification rate is first order with respect to CO_2 pressure below atmospheric pressure, and zeroth order at elevated pressures. Turkdogan and Vinters (1969) reported CO_2 gasification rates in the absence of CO in the reactor feed gas to be half-order at pressures less than 10 atm, and zeroth order at pressures of 10-20 atm. Koenig *et al.* (1985,1986) also reported half-order behavior. The latter workers proposed a model involving dual-site adsorption and dissociation of CO_2 to explain this behavior. The two-site adsorption of CO_2 can be expressed as:



where C^* is a two-site surface complex. One possibility for the structure of C^* is a lactone-type surface species.

On the other hand, the gasification data of Johnson (1979) for a bituminous coal char in CO/CO_2 mixtures over the range of 2-35 atm, showed a decreasing effect of CO_2 partial

pressure on the gasification rate at high pressures. A similar trend was reported by Golovina (1980), who reported first order behavior at near-atmospheric pressure, trending to zeroth order over the 3-10 atm range, followed by decreasing gasification rate with CO₂ partial pressure in the 20-40 atm pressure range.

However, some other notable exceptions have also been reported. Blackwood and Ingeme (1960) measured the gasification rate at elevated pressures, and proposed the following mechanism based on their data:



This mechanism results in a rate expression (Blackwood and Ingeme, 1960):

$$r = \frac{kP_{\text{CO}}^2}{1 + aP_{\text{CO}} + bP_{\text{CO}_2}} \quad (2)$$

which indicates a second order dependence on CO₂ partial pressure over a certain range.

Another factor to be considered is the inhibition by CO evident in Eqns. (1) and (2). It is known that product CO can have a retarding effect on the rate of reaction (Turkdogan and Vinters, 1970; Shufen and Ruizheng, 1994; DeGroot and Shafizadeh, 1984; Blackwood and McTaggart, 1959). Two theories have been advanced to explain this effect of CO (Blackwood and Ingeme, 1960). Gadsby *et al.* (1948) suggested that CO can be adsorbed on the carbon surface and thus compete for active sites. The process is represented by the reaction:



Blackwood and Ingeme (1960) and Liu *et al.* (2000) included this step in their mechanisms to explain gasification rates at high pressures. The second possibility, which is the most supported in the literature (Mentser and Ergun, 1973; Reif, 1952; Harris and Smith, 1989; Ye *et al.*, 1998; Kapteijn *et al.*, 1991), is the oxygen-exchange mechanism:



which suggests that CO inhibition occurs not by adsorption, but rather *via* the reverse reaction between CO and chemisorbed oxygen.

Due to the questions still remaining, the effects of elevated CO₂ pressures on gasification reactivity and the inhibition effect of CO were investigated in a high pressure TGA.

Experimental

High pressure thermogravimetry

Gasification rate data were obtained using a high pressure, high temperature thermogravimetric apparatus manufactured by DMT (Deutsche Montan Technologie) capable of operating under pressures up to 40 bar and temperatures up to 1100°C. The TGA system consists of: (1) the entire TGA-reactor; (2) the gas supply for three reaction gases and the flushing or purge gas; (3) the expansion unit including the condenser; (4) separate bypasses for the permanent reaction gases; and (5) a computerized data acquisition and process control system that allows for the recording of temperature, pressure, gas flow rates, and sample mass. The software also allows for automated pressurizing and depressurizing, control of total and partial pressures, flow rates, and internal and external temperatures.

With this system, the gas mixture can be pre-adjusted without exposing the sample to a reactive environment, while the sample is maintained under a separate inert flowing atmosphere. This guarantees a minimum of weight signal disturbance during switching from one atmosphere to the other. A process flow diagram is presented in Figure 7.1, and an image of the DMT-TGA apparatus in Figure 7.2.

A cylindrical sample holder containing approximately 100 mg of sample was placed in the pressurized sample chamber. The system was pressurized with CO₂/N₂ or CO₂/CO mixtures. The reaction zone was heated to the desired temperature and the sample was then lowered into the reaction zone. Gasification measurements were made at the following conditions:

Total pressure: 1-20 atm

Total flow rate: 0.90 l/min

Char samples

A few different chars were investigated in this work. The Brown University samples were prepared from synthesized phenol-formaldehyde resin (all from the same batch), and Wyodak subbituminous coal samples obtained from the Penn State coal sample bank (DECS-26/PSOC-1566) (DECS, 1995). The fresh resin and coal were sieved to +35/-20 mesh (420 – 840 μm), and then pyrolyzed in a quartz tube furnace in flowing ultrahigh pure helium at 1273K for 2 h. The resultant particle size range of the resultant char was 250-360 μm . The resultant chars were then activated in oxygen at 793K; the resin char to approximately 6%, and the Wyodak char to about 10% burn-off.

Preparation of the Brigham Young University (BYU) samples is described elsewhere in this report. The ultimate analysis of these coals and char samples produced in the HPFFB and the atmospheric flat flame burner at BYU are given in Table 7A.1 in Appendix A. The resultant pore size distributions and surface areas are presented in Table 7A.2. The latter were obtained from the CO_2 adsorption/desorption isotherms (195K – dry ice in acetone bath) presented in Figures 7A.1-4, that were obtained at Brown University.

Results and Discussion

The effect of total CO_2 pressure

The effect of total pressure on the gasification rate was investigated at temperatures between 825 and 1100°C in the pressure range 1-20 atm in pure CO_2 for the phenolic resin char (PRC) and Wyodak coal char (WY). Arrhenius plots of the resin char and Wyodak coal char reactivities in CO_2 are presented in Figures 7.3 and 7.4, respectively. The results in Figure 7.3 show that the apparent activation energy *decreases* with increasing pressure. In addition, increasing pressure *increases* the reactivity, especially at low temperatures, but this effect *decreases* with increasing temperature, such that by 1373K, the effect of pressure is much less marked. These data are in disagreement with some classical models developed at atmospheric pressure and below that suggest

asymptotic behavior of reactivity with increasing CO₂ pressure (Turkdogan and Vinters, 1969; Liu *et al.*, 2000; Frederick *et al.*, 1993).

In Figure 7.4 for the Wyodak coal char, it can be seen that the reactivity is almost unaffected by increasing total pressure up to about 15 atm. Above this pressure (20 atm) the reactivity *increases* considerably at temperatures < 900°C, and the apparent activation energy *decreases* with increasing total pressure (P > 10 atm). This behavior is most probably due to the presence of catalytic mineral matter impurities in the Wyodak coal char; e.g., calcium, which is known to catalyze the CO₂ gasification reaction. For example, Walker *et al.* (1979,1984) demonstrated that the reactivity of lignite chars is controlled primarily by the catalytic effect of calcium associated with carboxyl groups.

Some literature values for apparent activation energy and reaction order for CO₂ gasification for a variety of char types under various conditions are presented in Table 7.1. A summary of apparent activation energies for the resin char and Wyodak coal char obtained in the current work are presented in Table 7.2. These values agree reasonably well with some of the values reported in Table 7.1.

The effect of CO₂ partial pressure

The CO₂ partial pressure was varied from 100% to 40% at a total pressure of 15 atm by dilution with nitrogen. The gasification temperatures were 900°C for Wyodak coal char and 1000°C for the resin char.

In Figures 7.5 and 7.6 are presented plots of ln(*r*) vs ln(*P*_{CO₂}) for resin char and Wyodak coal char, respectively, where *r* is the specific reactivity, defined as the mass loss rate, *dm/dt*, divided by the sample mass, *m*, at the time *t*:

$$r = \frac{1}{m} \left(\frac{dm}{dt} \right) = kP_{CO_2}^n \quad (3)$$

where *k* is the rate constant, *P*_{CO₂} is the CO₂ partial pressure, and *n* is the apparent reaction order.

As shown in both figures, the partial pressure has a significant effect on reactivity for both chars at the selected gasification conditions, with the reactivity *increasing* with increasing CO₂ partial pressure. From Eq. (3), the slope of the plot of $\ln(r)$ vs $\ln(P_{CO_2})$ is equal to the apparent reaction order, n . As shown in Figure 7.5 and 7.6, the apparent reaction order, n , is 0.45 ± 0.09 for the resin char and 0.68 ± 0.39 for the Wyodak coal char. It has been reported that the reaction order for CO₂ gasification is first order with respect to CO₂ partial pressure below atmospheric pressure (Gadsby *et al.*, 1948; Biederman *et al.*, 1976), and half order at higher pressures (Nozaki *et al.*, 1992; Turkdogan and Vinters, 1969). The reaction orders observed in the current work agree reasonably well with some of the values reported in Table 7.1.

A comparison of the reactivities for both chars as a function of CO₂ partial pressure is presented in Figure 7.7. Since the Wyodak coal char contains mineral matter impurities, its reactivity is significantly greater than that of the resin char, even at lower CO₂ partial pressures.

The inhibition effect of CO

It is known that CO can have an inhibiting effect on the CO₂ gasification rate (Turkdogan and Vinters, 1970; Shufen and Ruizheng, 1994; DeGroot and Shafizadeh, 1984; Blackwood and McTaggart, 1959). However, studies on the effect of CO on the CO₂ gasification rate reaction at elevated pressure are relatively limited (Blackwood and Ingeme, 1960; Frederick *et al.*, 1993). Gasification rate measurements were carried out in the pressurized microbalance at 900°C for the Wyodak coal char and 1000°C for the resin char. CO₂ and CO partial pressures were varied while holding the total pressure constant at 15 atm.

In Figures 7.8 and 7.9 are presented plots of $\ln(r)$ vs $\ln(P_{CO_2})$ for the resin char and Wyodak coal char, respectively, along with the data from Figures 7.5 and 7.6 for comparison. As shown, in Figure 7.8, for the same corresponding CO₂ partial pressures, the reactivity *decreases* considerably with increasing CO partial pressure, and the apparent reaction order *increases* significantly from 0.45 ± 0.09 in the absence of CO to

1.15 ± 0.23 in the presence of additional CO. These data demonstrate the strong inhibition effect of CO on the gasification reaction. Frederick *et al.* (1993) investigated the effect of CO on the CO₂ gasification reaction at 700°C and elevated pressures and reported an apparent reaction order of 0.88.

Similar trends were observed for the Wyodak coal char in Figure 7.9. As shown, the reactivity *decreases* considerably with increasing CO partial pressure for the same corresponding CO₂ partial pressures, and the apparent reaction order *increases* from 0.68 ± 0.39 in the absence of CO to 1.96 ± 0.44 in the presence of additional CO. This is suggestive of the behavior of the rate expression proposed by Blackwood and Ingeme (1960) which described results obtained at elevated pressures in the presence of 10% of CO:

$$r = \frac{kP_{CO_2}^2}{1 + aP_{CO} + bP_{CO_2}} \quad (4)$$

indicating a *second order* dependence on CO₂ partial pressure over a certain pressure range. In order to test this rate form further, plots of P_{CO₂}/r vs 1/P_{CO₂} at constant total pressure (P_{CO₂} + P_{CO} = c = 15 atm), varying the relative partial pressures of CO₂ and CO, should be linear if the data conform to Eq. (4); i.e.,

$$\frac{P_{CO_2}}{r} = \frac{1}{kP_{CO_2}} [1 + ac] + \frac{(b - a)}{k} \quad (5)$$

Plots of Eq. (5) for the Wyodak coal char and the PRC are presented in Figure 7.10. As shown, the Wyodak data do indeed appear to follow a relatively linear relationship, thereby indicating agreement with the kinetic rate form of Eqns. (4) and (5) originally proposed by Blackwood and Ingeme (1960). However, as is also as shown in Figure 7.10, the PRC data, do not appear to follow this same rate form at all. Instead, they appear to follow the more traditional first order Langmuir-Hinshelwood rate form of Eq. (2), which when plotted in a similar fashion as Eq. (5) becomes:

$$\frac{1}{r} = \frac{1}{kP_{CO_2}} [1 + ac] + \frac{(b - a)}{k} \quad (6)$$

Plots of Eq. (6) for both sets of data are presented in Figure 7.11. As shown, it is clear that the PRC data fit the form of Eqns. (2) and (6), while the Wyodak data do not.

The primary difference between these two chars is that the Wyodak coal char reactivity is controlled by mineral matter whereas the PRC is not. Most probably the oxygen transport capacity of mineral matter sites in the Wyodak coal char to active carbon sites results in apparent second order behavior, whereas the first order behavior of the PRC is more in concert with the traditional oxygen exchange mechanism discussed previously.

Comparisons of the reactivities of both chars as a function of CO₂ partial pressure are presented in Figure 7.12. As shown, the Wyodak coal char exhibits *greater* reactivity than the resin char for CO₂ partial pressures greater than 11.25 atm (75% CO₂) primarily due to the presence of catalytic mineral matter impurities. However, with an increase in CO partial pressure (> 3.75 atm, or 25% CO) the reactivity of the Wyodak coal char becomes less than that of the phenolic resin char. This is most probably related to the effects of CO chemisorption on mineral matter impurities as well, that serves to retard the surface oxygen transport process catalyzed by the mineral matter to active carbon sites. Consequently, not only do mineral matter impurities often control the reactivity of coal chars, but can also alter the mechanism and the resultant apparent rate form as well. Due to the elliptic nature of Langmuir-Hinshelwood rate expressions (Eqns. (2) and (4)) plus the almost certain energetic heterogeneity of char surfaces (e.g., see Calo and Perkins, 1987), the apparent reaction order for CO₂ gasification can vary over the range of zero to two. This is one of the reasons for the wide range of apparent reaction orders reported in the literature. Consequently, the development of robust rate expressions for a particular char still depends on obtaining reliable reaction rate data at conditions similar to what the char will experience in practice. This is one of the important themes of the current project.

BYU coal chars

Reactivity measurements were obtained for four coal chars (Knife River, Wyodak, Koonfontain, and Pittsburgh #8) produced at 1300K at atmospheric pressure (actually 0.85 atm in Utah) in an atmospheric flat flame burner facility at Brigham Young University (Zhang and Fletcher, 2001). The char samples were collected immediately above the luminous devolatilization zone of the flame. The size of coal particles ranged from 45 to 130 μm . Typical particles used in pulverized coal furnace applications had a mean diameter of $\sim 50 \mu\text{m}$. Particle heating rates were $\sim 10^5 \text{ K/s}$.

The resultant measured reactivities are presented in Figures 7.13-7.17 for these coal chars, and the apparent activation energies are summarized in Table 7.3. The results for the BYU Wyodak coal char presented in Figure 7.13 show that reactivity increases with CO_2 pressure, as expected. A summary plot of the reactivity data for both the BYU and BU Wyodak chars is presented in Figure 7.14. It is noted that these coal chars differ primarily in the heating rates at which they were prepared, and the “heat soak” time at the ultimate temperature. The BU samples in Figure 7.3 were produced in a tube furnace at very low heating rates at 1273K, whereas the samples in Figure 7.13 were prepared at about 1300K at heating rates on the order of 10^5 K/s . As shown, the BYU samples are much more reactive at higher temperatures, but their apparent activation energies are also greater, such that their reactivities become more comparable to the BU Wyodak samples at lower temperatures. Thus, the noted differences in reactivity are undoubtedly due to the considerably longer annealing times experienced by the BU chars (i.e., 2h in the tube furnace vs 50 – 100 ms in the flat flame burner), which significantly decreased the concentrations of active sites in the BU chars.

Similar reactivity behavior is noted for the Knife River lignite, the Koonfontain, and the Pittsburgh #8 coal chars in Figures 7.15, 7.16, and 7.17, respectively. For the Pittsburgh #8 char there was a very large increase in reactivity upon increasing the CO_2 pressure from 5 atm to 10 atm.

Chapter 7 Conclusions

CO₂ gasification reactivities were determined for a phenolic resin char and Wyodak coal char and the effects of total CO₂ pressure, CO₂ partial pressure, and the inhibition effect of CO on the reaction rate were investigated at elevated pressures. For both chars, the apparent activation energy *decreases* with *increasing* pressure. In the case of the resin char, higher pressure *increases* reactivity at low temperature, but this effect *decreases* with increasing temperature, such that by 1373K, the effect of pressure has *decreased* substantially. These data are in disagreement with some classical models developed at atmospheric pressure and below that suggest asymptotic behavior of reactivity with increasing pressure. For the Wyodak coal char, the reactivity is only modestly affected by increasing the total pressure up to 15 atm. This is attributed to the presence of mineral matter impurities in the Wyodak coal char; i.e., calcium, which is known to catalytically dominate the CO₂ gasification reaction.

These char samples were gasified in varying mixtures of CO₂ and nitrogen at a total pressure of 15 atm. The results show that char reactivity increases monotonically with CO₂ partial pressure for both chars. Since the Wyodak coal char contains mineral matter impurities, its reactivity is significantly higher than that of the resin char, even at lower CO₂ partial pressures.

The inhibition effect of CO on gasification rate was investigated for the phenolic resin char and Wyodak coal char in varying mixtures of CO₂ and CO at a total pressure of 15 atm. The reactivity *decreases* considerably with increasing CO partial pressure, and the apparent reaction order *increases* significantly from 0.45 to 1.15 for resin char and from 0.68 to 1.98 for Wyodak coal char. Kinetic analysis of these data show that the Wyodak coal char obeys a Langmuir-Hinshelwood-type rate form with both CO and CO₂ inhibition terms in the denominator and a numerator that is quadratic in CO₂ partial pressure (e.g., as proposed by Blackwood and Ingeme, 1960). The PRC data, on the other hand, are fit by a similar expression, but with a numerator that is first order in CO₂ partial pressure (e.g., as proposed by Mentser and Ergun, 1973). These differences in kinetic behavior are attributed to the surface oxygen transport capacity of the mineral matter in

the Wyodak coal char, most probably calcium (23.5 % of the ash by weight, on average; DECS, 1995).

The BYU coal char samples produced at high heating rates exhibited similar behavior; i.e., increasing reactivity with CO₂ partial pressure. The Wyodak coal char results indicate that the BYU chars were much more reactive at high temperatures than the BU samples, but exhibited larger apparent activation energies, such that their reactivities became more comparable to that of the BU Wyodak samples at lower temperatures. This was attributed to the high heating rate ($\sim 10^5$ K/s) and very short pyrolysis times (~ 100 ms) experienced by the samples in the BYU FFB. This did not allow any time for thermal annealing, and thus produced high concentrations of active carbon sites. Due to the elliptic nature of Langmuir-Hinshelwood rate expressions (Eqns. (2) and (4)) plus the almost certain energetic heterogeneity of char surfaces (e.g., see Calo and Perkins, 1987), the apparent reaction order for CO₂ gasification can vary over the range of zero to two. This is one of the reasons for the wide range of apparent reaction orders reported in the literature. Moreover, the char preparation conditions can have a very large impact on the resultant reactivities as well. Consequently, the development of robust rate expressions for a particular coal char still depends on obtaining reliable reaction rate data under preparation conditions and subsequent reaction conditions similar to what the char will experience in practice. This was one of the fundamental themes of this project.

Chapter 7 References

- Biederman, D.L., Miles, A.J., Vastola, F.J. and Walker, P.L. Jr., *Carbon*, 14, 351, (1976).
Blackwood, J.D. and Ingeme, A.J., *Australian Journal of Chemistry*, 13, 194, (1960).
Blackwood, J.D. and McTaggart, F.K., *Australian Journal of Chemistry*, 12, 533, (1959).
Calo, J.M., and Perkins, M.T. *Carbon*, 25, 395 (1987).
The Department of Energy Coal Sample Bank, DECS-Series Data Printouts, The Pennsylvania State University, University Park, PA, December, 1995.
DeGroot, W. and Shafizadeh, F., *Fuel*, 63, 210, (1984).

Dutta, S., Wen, C. Y., Belt, R. J., *Ind. Eng. Chem. Process Des. Dev.*, 16(1), 20, (1977).

Frederick, W.J., Wag, K.J. and Hupa, M.M., *Ind. Eng. Chem. Res.*, 32, 1747, (1993).

Gadsby, J., Long, F.J., Sleightholm, P. and Sykes, K.W., *Proc. Royal Society of London*, 193-A, 357, (1948);

Golovina, E.S., *Carbon*, 18, 197, (1980).

Harris, D. and Smith, I., *ACS Fuel Chemistry Division Preprints*, 34(1), 94, (1989).

Harris, D.J. and J.H. Patterson, *Aust. Inst. of Energy J.* 13, 22 (1995).

Hippo, E.J., Jenkins, R.G. and Walker, P.L., *Fuel*, 58, 338, (1979).

Jiang, H. and Radovic, L.R., *ACS Fuel Chemistry Division Preprints*, 34(1), 79, (1989).

Johnson, J.L., *Kinetics of Coal Gasification*, Wiley, NY, (1979).

Kapteijn, F. and Moulijn, J., *Fuel*, 62, 221, (1983).

Kapteijn, F., Meijer, R. and Moulijn, J.A., *ACS Div. Fuel Chemistry Prepr.*, 36(3), 906, (1991).

Koenig, P.C., Squires, R.G. and Laurendeau, N.M., *Carbon*, 23(5), 531, (1985).

Koenig, P.C., Squires, R.G. and Laurendeau, N.M., *Fuel*, 65, 412, (1986).

Liu, G., Tate, A.G., Bryant, G.W. and Wall, T.F., *Fuel*, 79, 1145, (2000).

Mentser, M. and Ergun, S., *U.S. Bur. Mines Bull.*, 664, (1973).

Nozaki, T., Adschiri, T. and Fujimoto, K., *Fuel*, 7(11), 249, (1992).

Ollero, P., Serrera, A., Arjona, R. and Alcantarilla, S., *Biomass and Bioenergy*, 24, 151, (2003).

Overholser, L.G. and Blakely, J.P., *Carbon*, 2, 385, (1965).

Reif, A.E., *J. Phy. Chem.*, 56, 785, (1952).

Shufen, L. and Ruizheng, S., *Fuel*, 73, 413, (1994).

Shufen, L. and Yuanlin, C., *Fuel*, 74(3), 456, (1995).

Sinag, A., Sinek, K., Tekes, A.T., Misirlioglu, Z., Canel, M. and Wang, L., *Chemical Engineering and Processing*, In Press, Corrected Proof, 15 January, (2003).

Smoot, L.D. and P.J. Smith, *Coal combustion and gasification*. Plenum Press, New York, 1985, p. x, xvi, 443.

Smoot, L.D., *Progress in Energy and Combustion Science* 24 (5), 409-501 (1998).

Takematsu, T. and C. Maude, *Coal Gasification for IGCC Power Generation*. London, 1991.

Turkdogan, E.T. and Vinters, J.V., *Carbon*, 7, 101, (1969).

Walker, P.L. Jr., in *Carbon and Coal Gasification*, Figueiredo, Moulijn, eds., NATO ASI Series, 9.3, (1986).

Ye, D.P., Agnew, J.B. and Zhang, D.K., *Fuel*, 77(11), 1209, (1998)

Zhang, L. and Calo, J.M., *ACS Div, Fuel Chemistry Prepr.*, 41(1), 138, (1996).

Zhang, H. and T. H. Fletcher, *Energy and Fuels*, 15: 1512-1522 (2001).

Table 7.1 Apparent activation energies and reaction orders for the char-CO₂ gasification reaction.

Sample	Temperature Range (K)	CO ₂ Partial Pressure (bar)	Apparent Activation Energy (kJ/mol)	Apparent Reaction Order	Reference
Coal char	1093-1158	1	251	–	Jiang and Radovic, 1989
Coke, char	923-1173	1	185-245	0.68	Harris and Smith, 1989
Coal char	993-1293	2	122	–	Shufen and Yuanlin, 1995
Lignite char	1073-1323	1	146-128	–	Sinag <i>et al.</i> , 2003
Olive residue char	1073-1223	0.2-0.5	133	0.43	Ollero <i>et al.</i> 2003
Australian coal char	987-1165	1	91	–	Ye <i>et al.</i> , 1998
Coal chars	1123	0.2-0.5 0.5-15 above 15	–	0.7 0.5 0.7	Nozaki <i>et al.</i> , 1992
Lignite char	1073-1223	10	149	0.34	Shufen and Riuzheng, 1994
Resin and coal chars	1073-1205	1	209-251	0.7 0.6	Zhang and Calo, 1996
Graphite	1050-1300	1	230-251	0.7	Overholser and Blakely, 1965
Graphite and coconut char	975-1475	10 ⁻³ -10	284.5	0.5	Turkdogan and Vinters, 1969

Table 7.2 Apparent activation energies for CO₂ gasification of the Brown University samples: resin char (PRC) and Wyodak coal char (WY) as a function of pressure.

Char Sample	Total Pressure (atm)	Apparent Activation Energy (kJ/mol)
PRC	1	178 ± 18
PRC	5	163 ± 16
PRC	10	149 ± 15
PRC	15	110 ± 11
PRC	20	107 ± 11
WY	1	161 ± 16
WY	5	164 ± 16
WY	10	155 ± 16
WY	15	138 ± 14
WY	20	94 ± 9

Table 7.3 Apparent activation energies for CO₂ gasification of the Brigham Young University samples as a function of pressure.

Char Sample	Total CO ₂ Pressure (atm)	Apparent Activation Energy (kJ/mol)
Wyodak	1	233 ± 23
Wyodak	5	198 ± 20
Wyodak	10	230 ± 23
Knife River	1	206 ± 21
Knife River	10	299 ± 30
Koonfontaine	1	336 ± 34
Koonfontaine	10	288 ± 29
Pittsburgh #8	1	198 ± 20
Pittsburgh #8	5	160 ± 16
Pittsburgh #8	10	468 ± 47



Figure 7.2 High pressure, high temperature thermogravimetric apparatus (DMT-TGA).

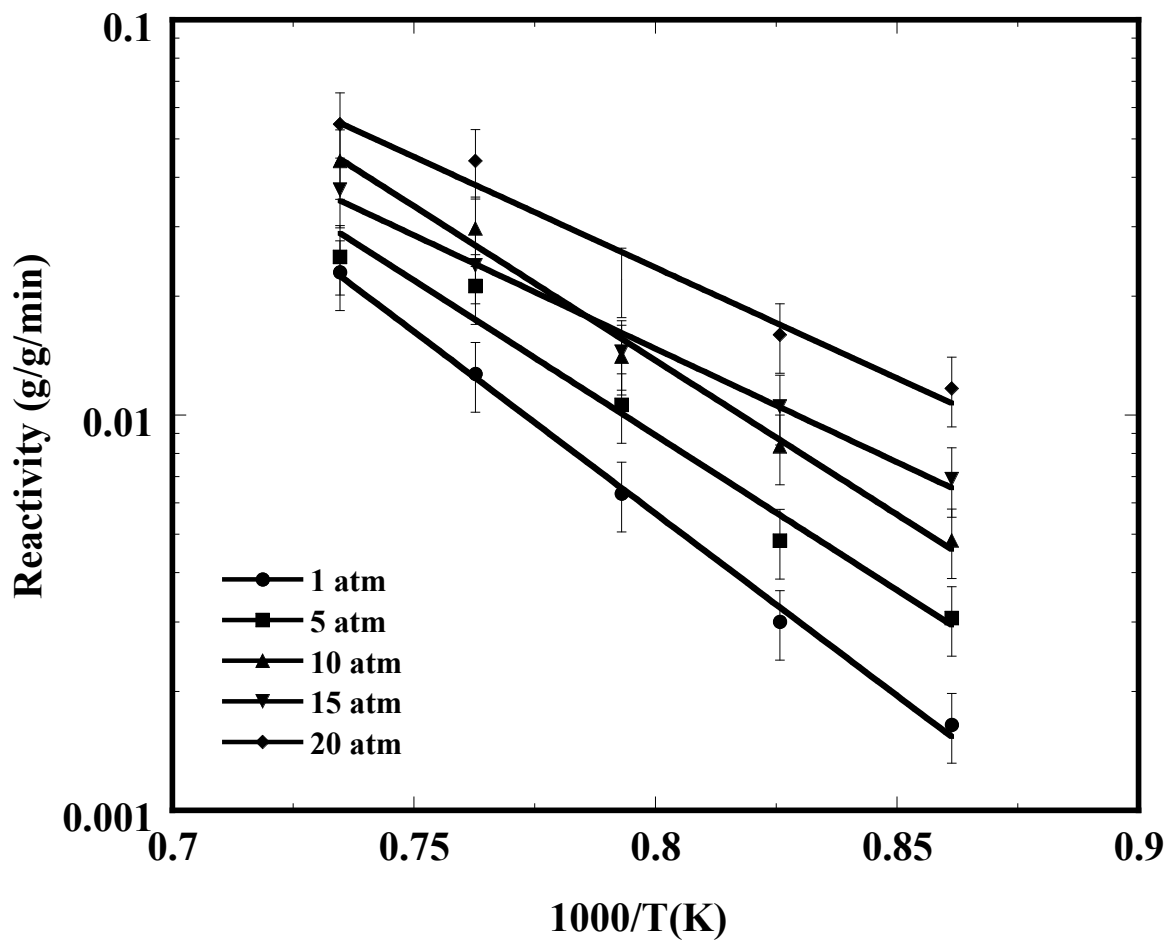


Figure 7.3. Arrhenius plots for phenolic resin char (PRC) as a function of total CO₂ pressure.

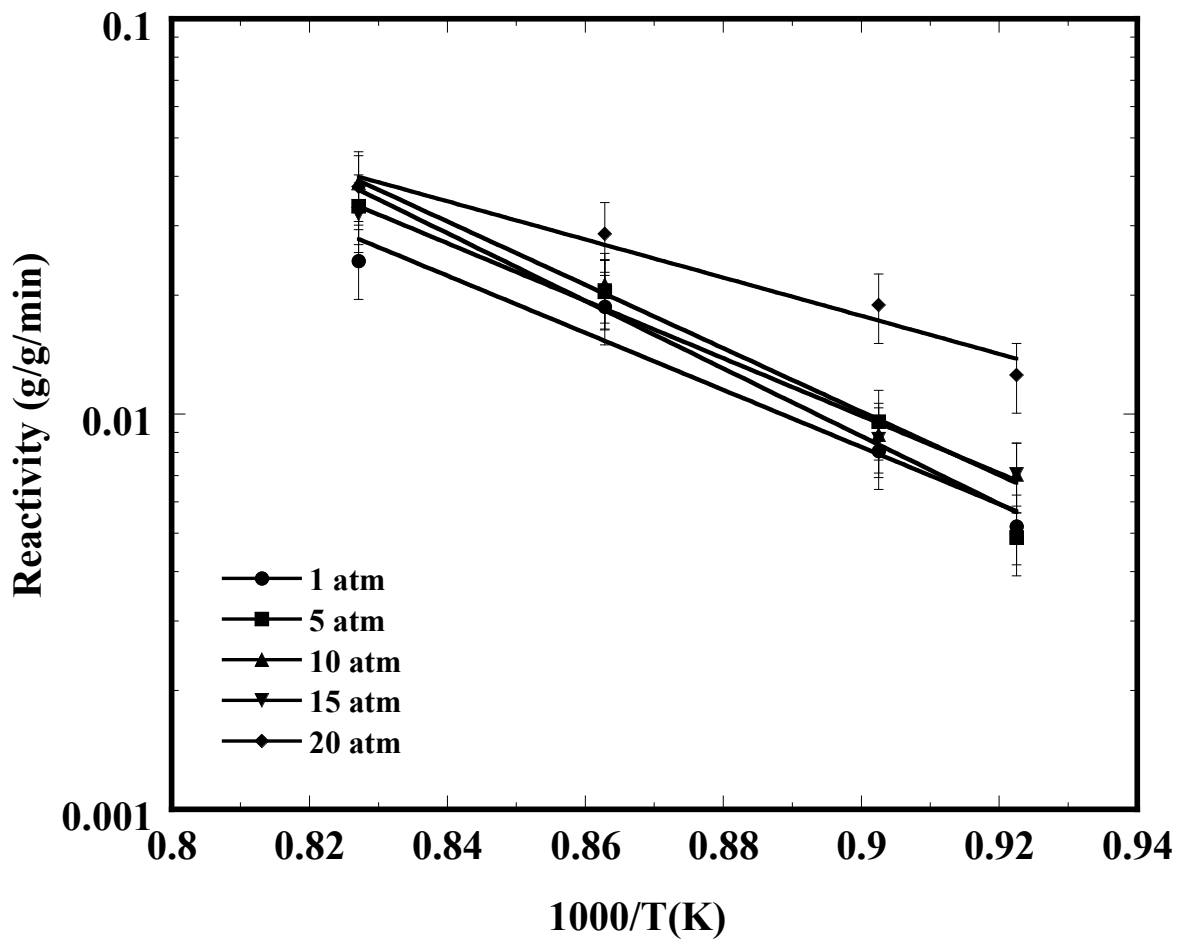


Figure 7.4. Arrhenius plots for Wyodak coal char (WY) as a function of total CO₂ pressure.

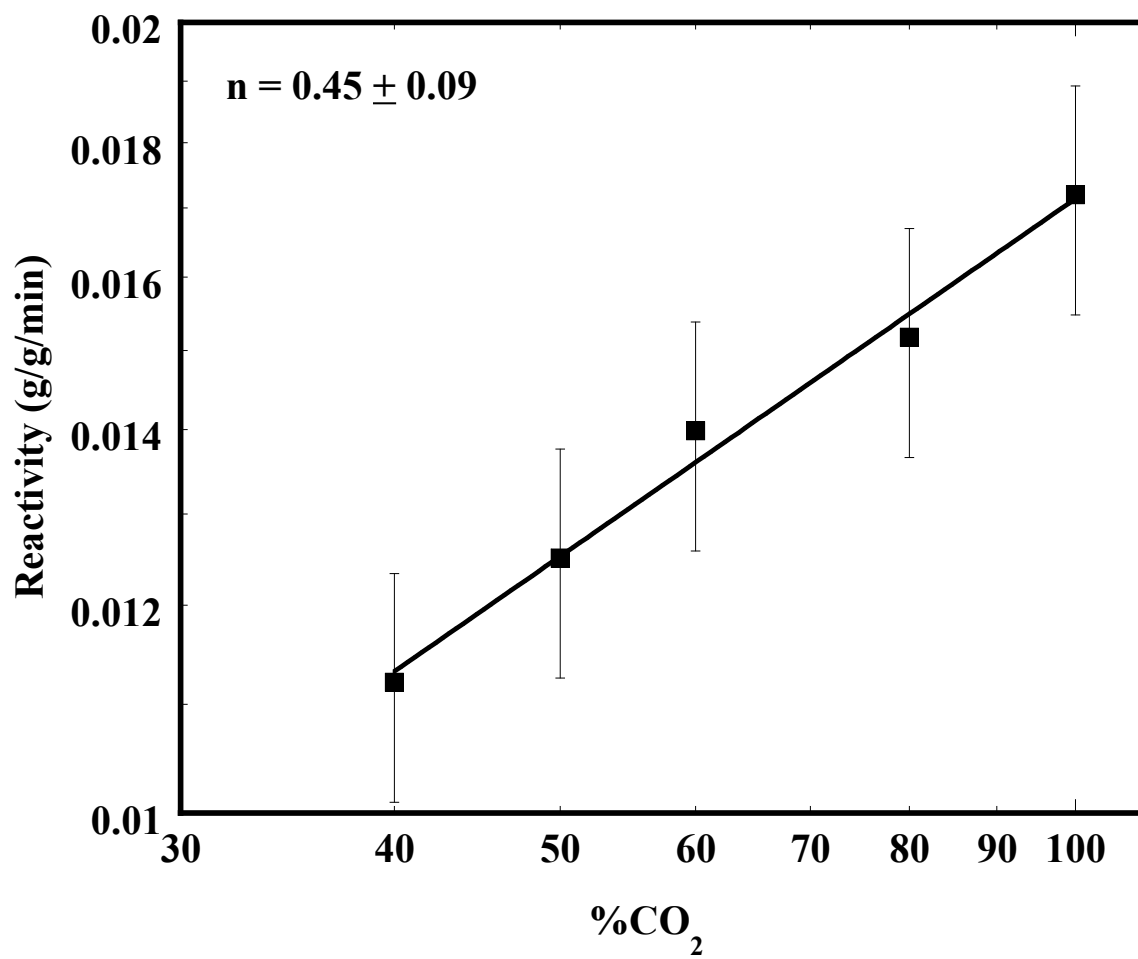


Figure 7.5. Specific reactivity of phenolic resin char (PRC) in CO₂/N₂ mixtures at 1000°C as a function of CO₂ partial pressure at a total pressure of 15 atm.

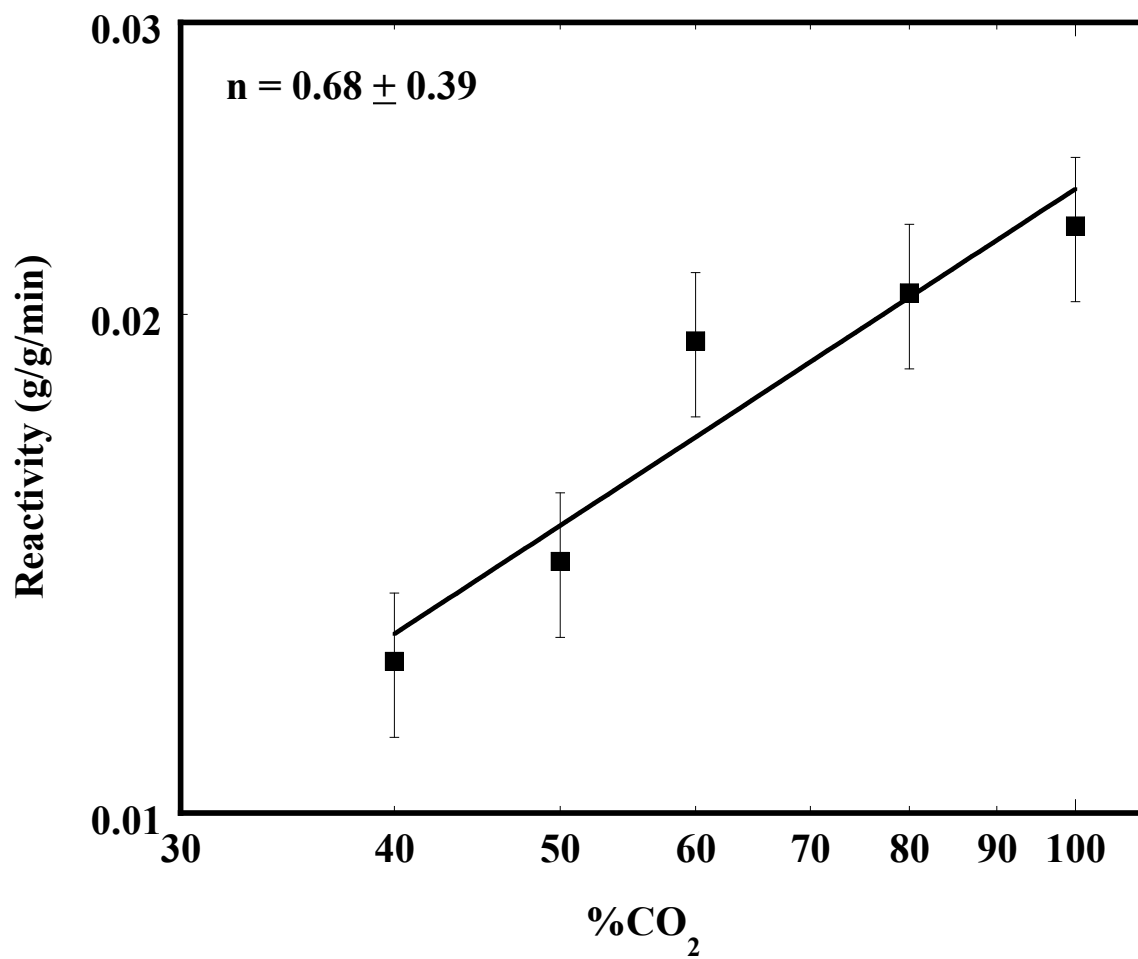


Figure 7.6. Specific reactivity of Wyodak coal char (WY) in CO₂/N₂ mixtures at 900°C as a function of CO₂ partial pressure at a total pressure of 15 atm.

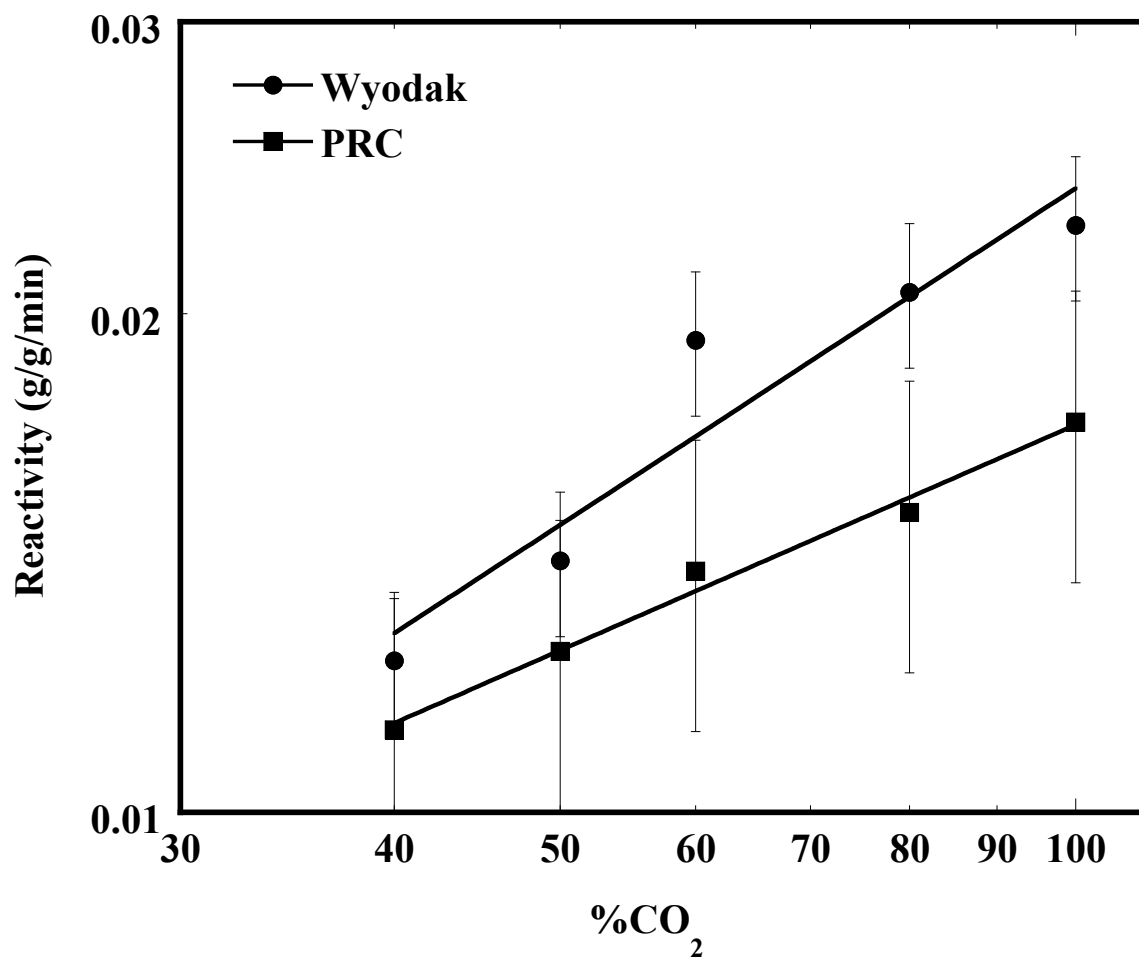


Figure 7.7 Comparison of specific reactivities of phenolic resin char (PRC) and Wyodak coal char (WY) in CO₂/N₂ mixtures as a function of CO₂ partial pressure at a total pressure of 15 atm.

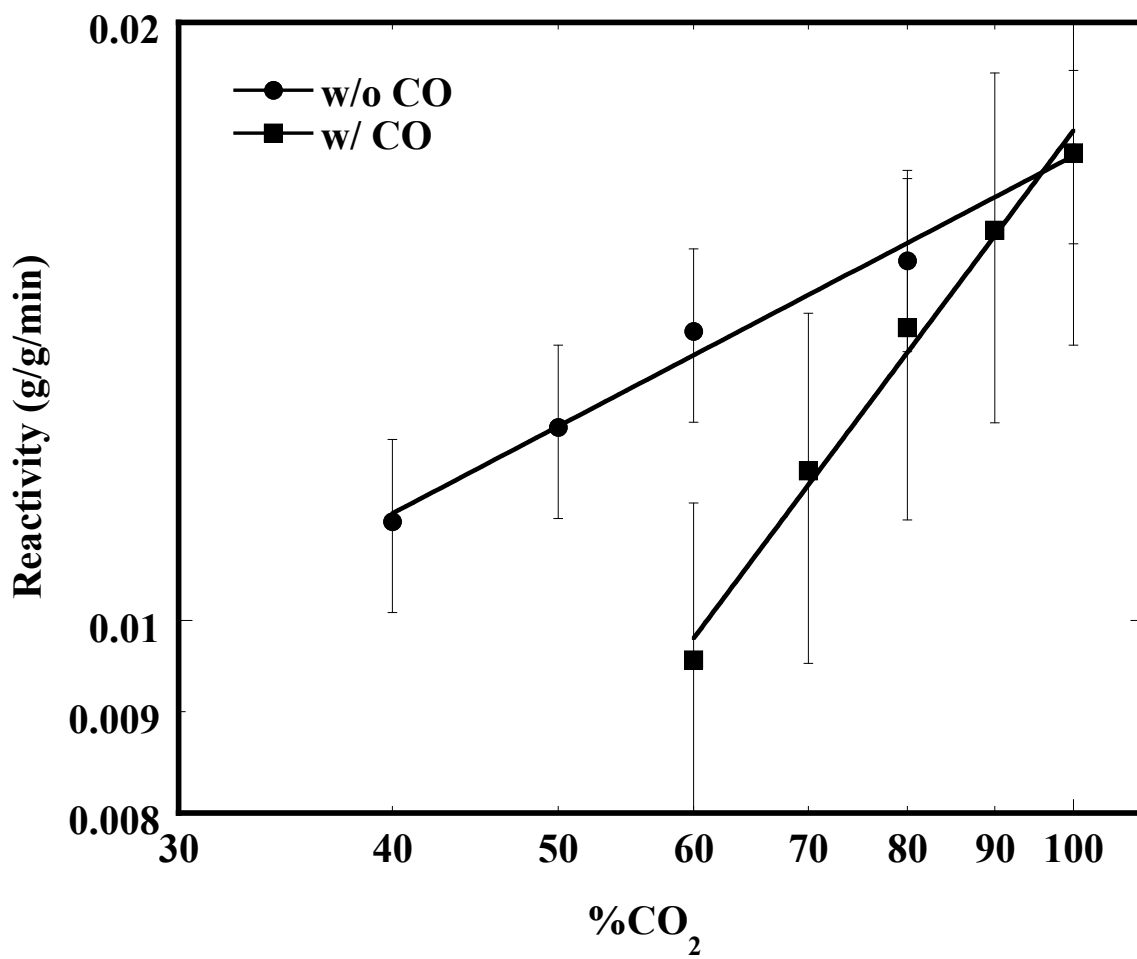


Figure 7.8 Specific reactivity of phenolic resin char (PRC) in CO₂/CO mixtures at 1000°C as a function of CO₂ partial pressure at a total pressure of 15 atm.

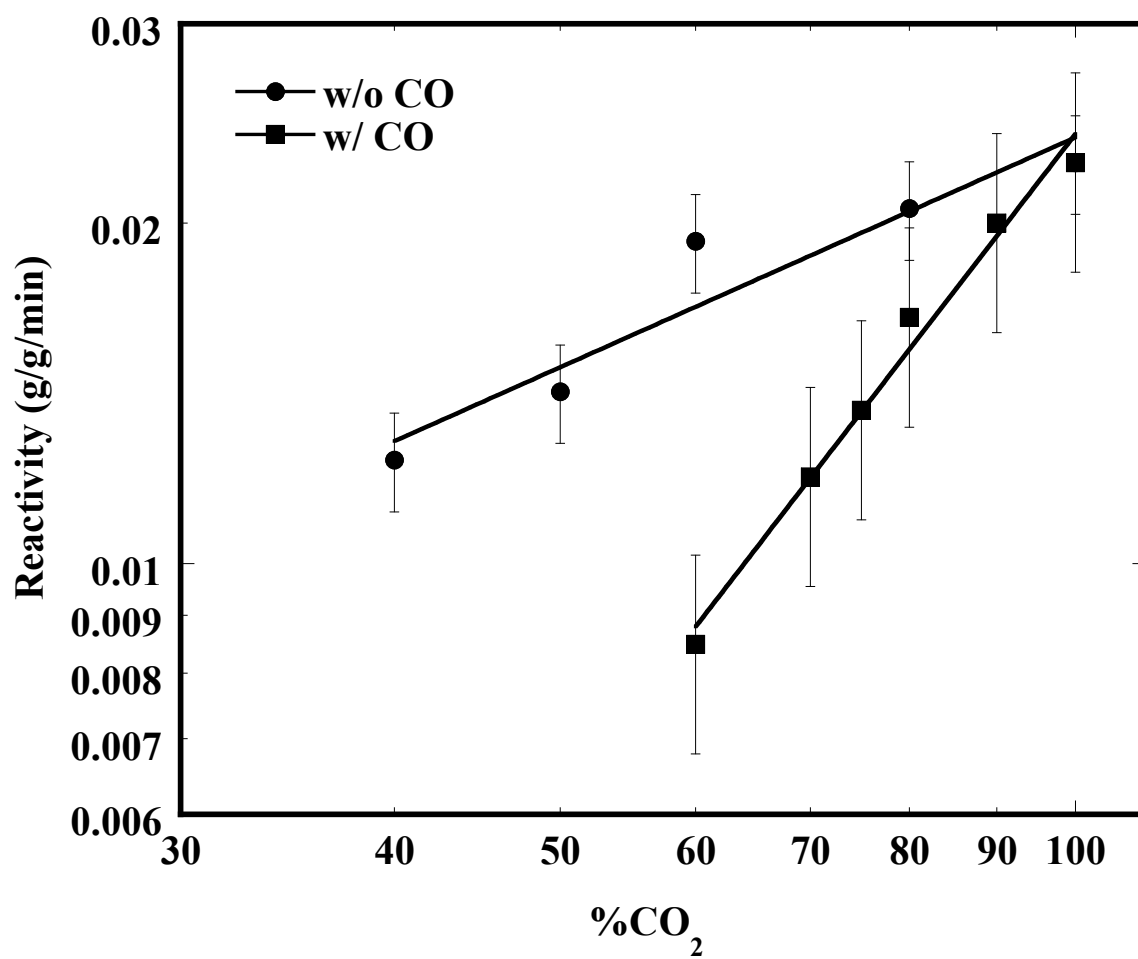


Figure 7.9 Specific reactivity of Wyodak coal char (WY) in CO₂/CO mixtures at 900°C as a function of CO₂ partial pressure at a total pressure of 15 atm.

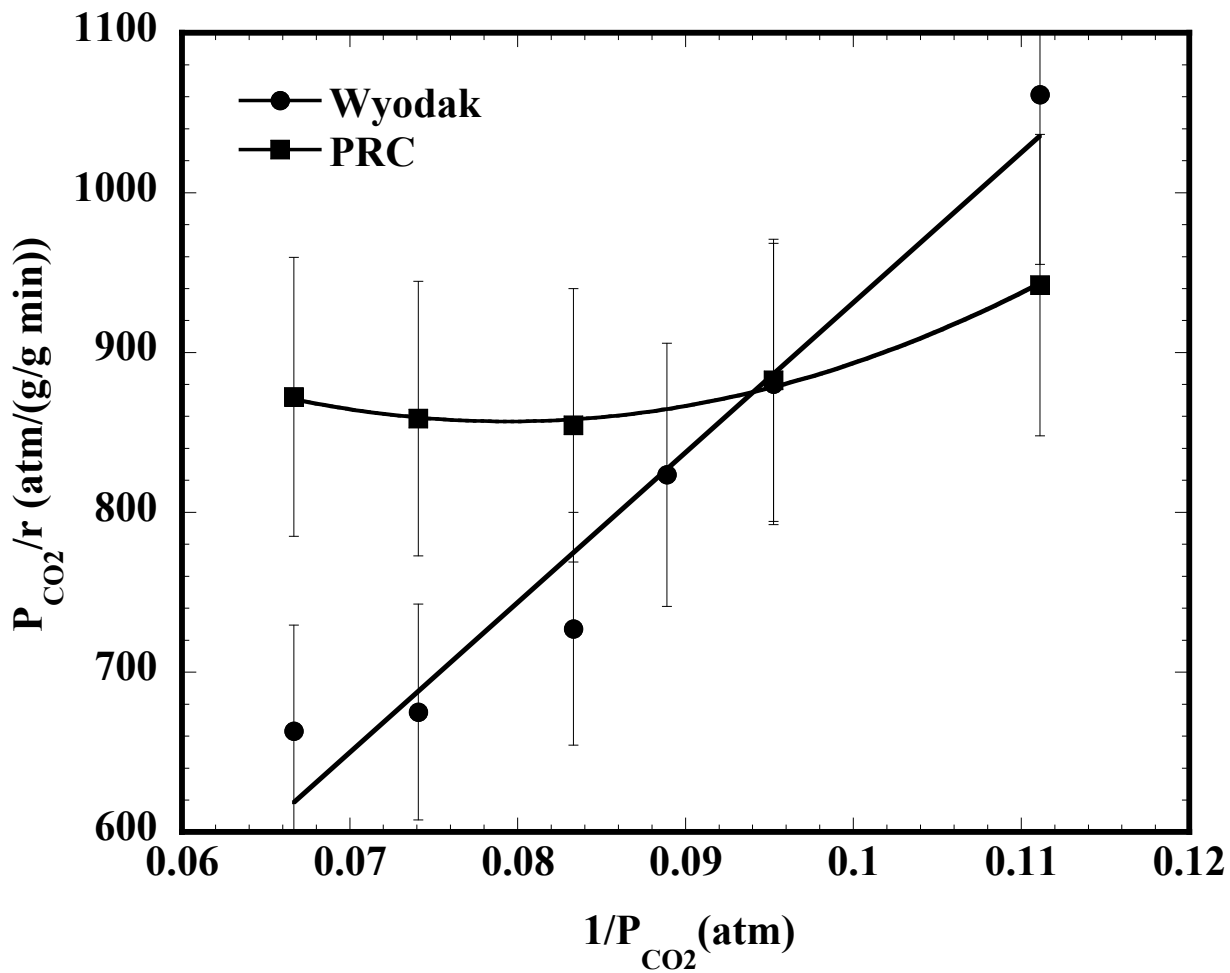


Figure 7.10 Test of quadratic kinetic model of Wyodak coal char and phenolic resin chars at a total pressure of 15 atm in CO₂/CO mixtures.

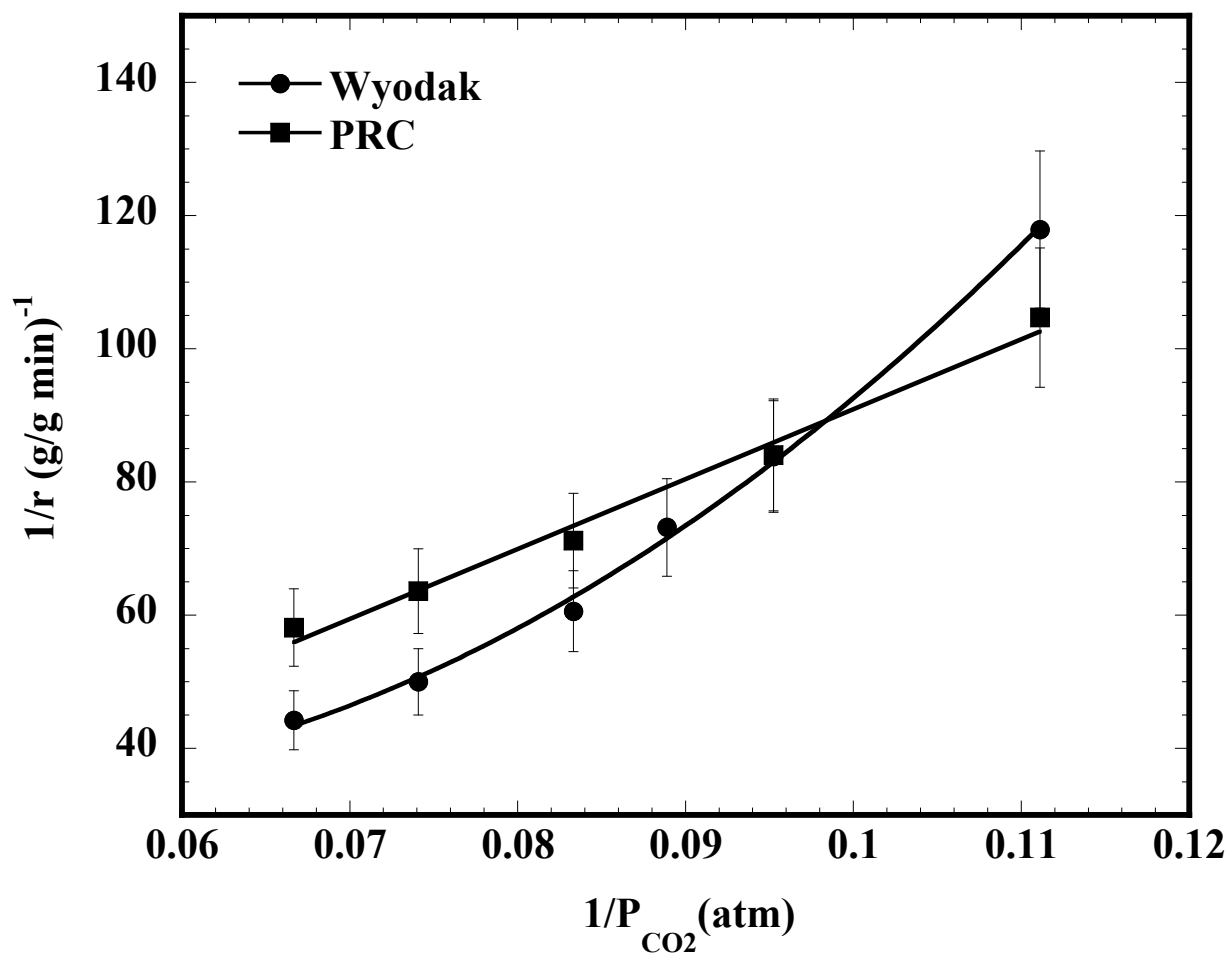


Figure 7.11 Test of first order kinetic model of Wyodak coal char and phenolic resin chars at a total pressure of 15 atm in CO₂/CO mixtures.

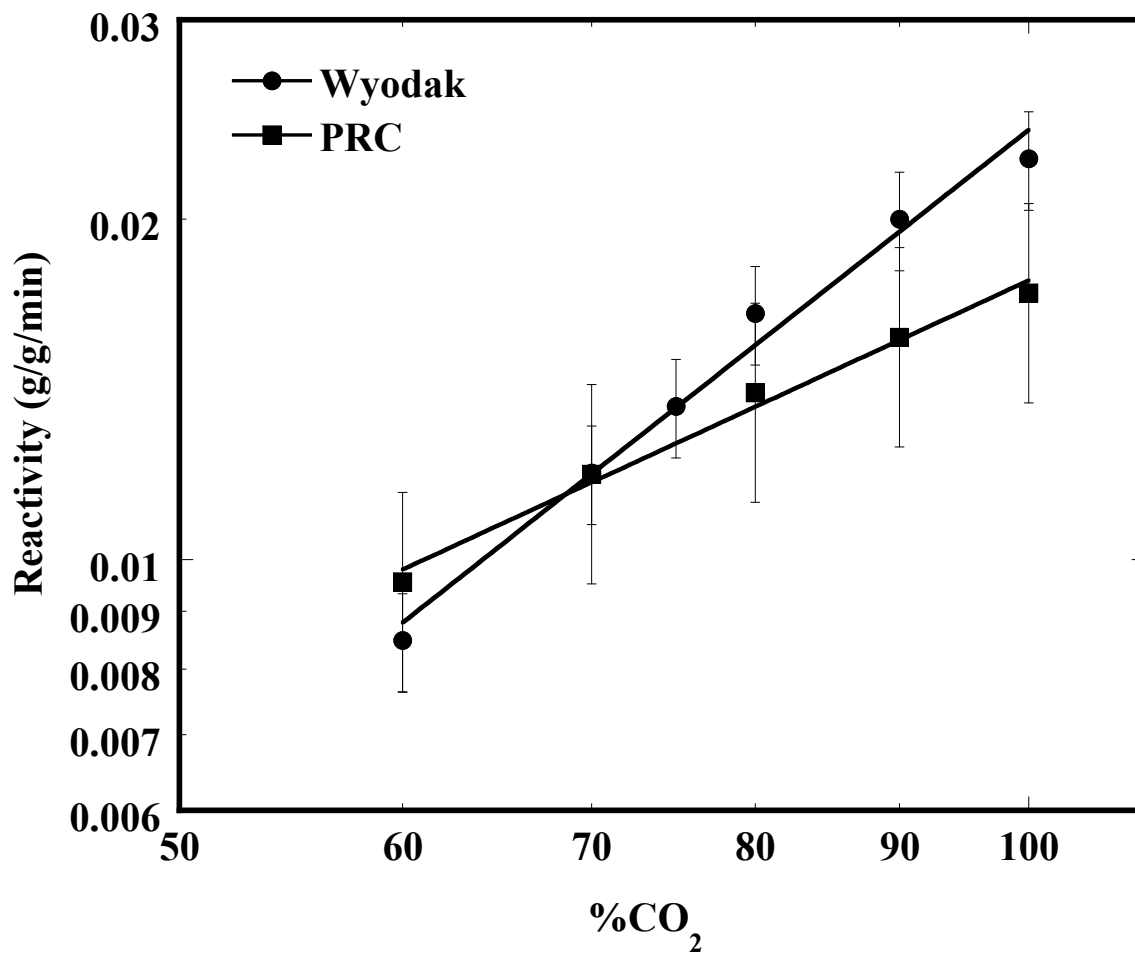


Figure 7.12 Comparison of specific reactivities of phenolic resin char (PRC) and Wyodak coal char (WY) in CO₂/CO mixtures as a function of CO₂ partial pressure at a total pressure of 15 atm.

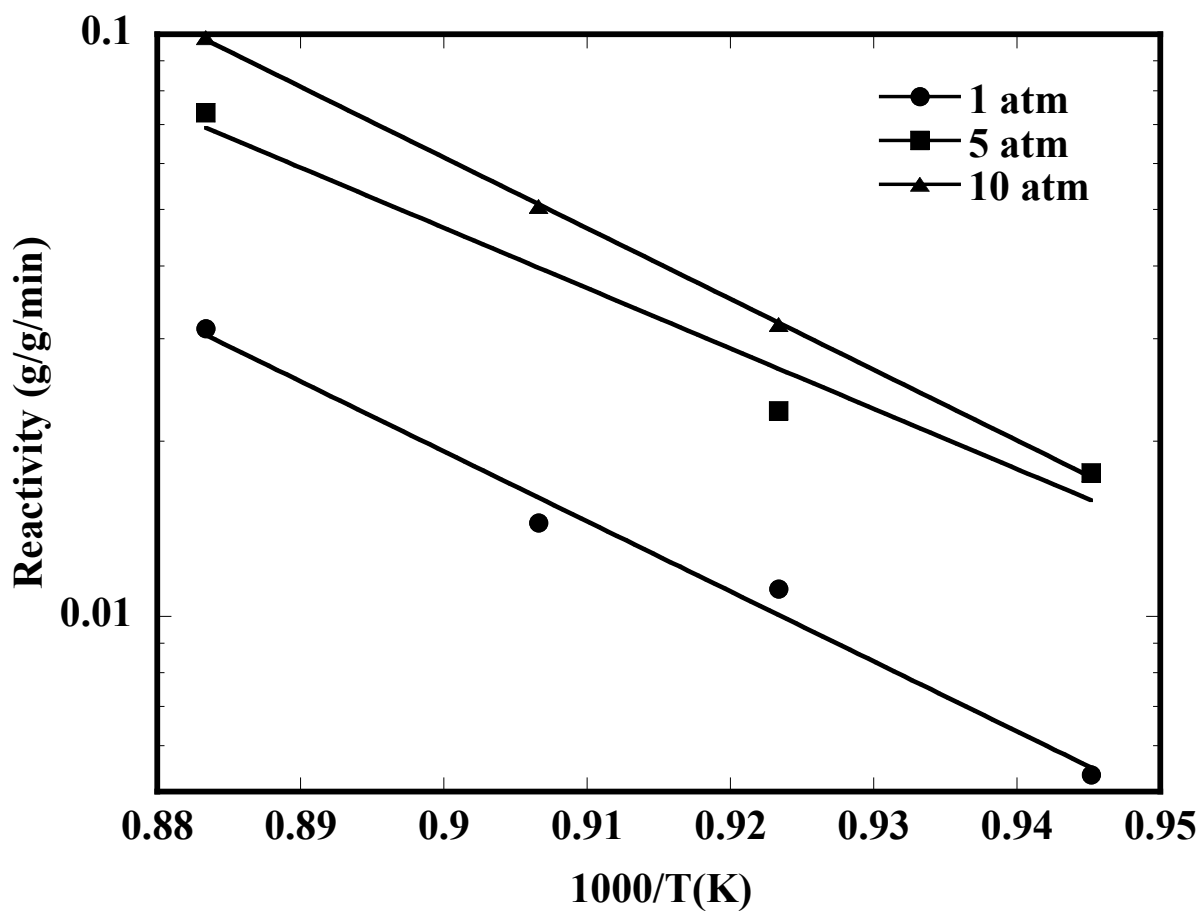


Figure 7.13 Arrhenius plots for Wyodak (BYU) coal char as a function of total CO₂ pressure.

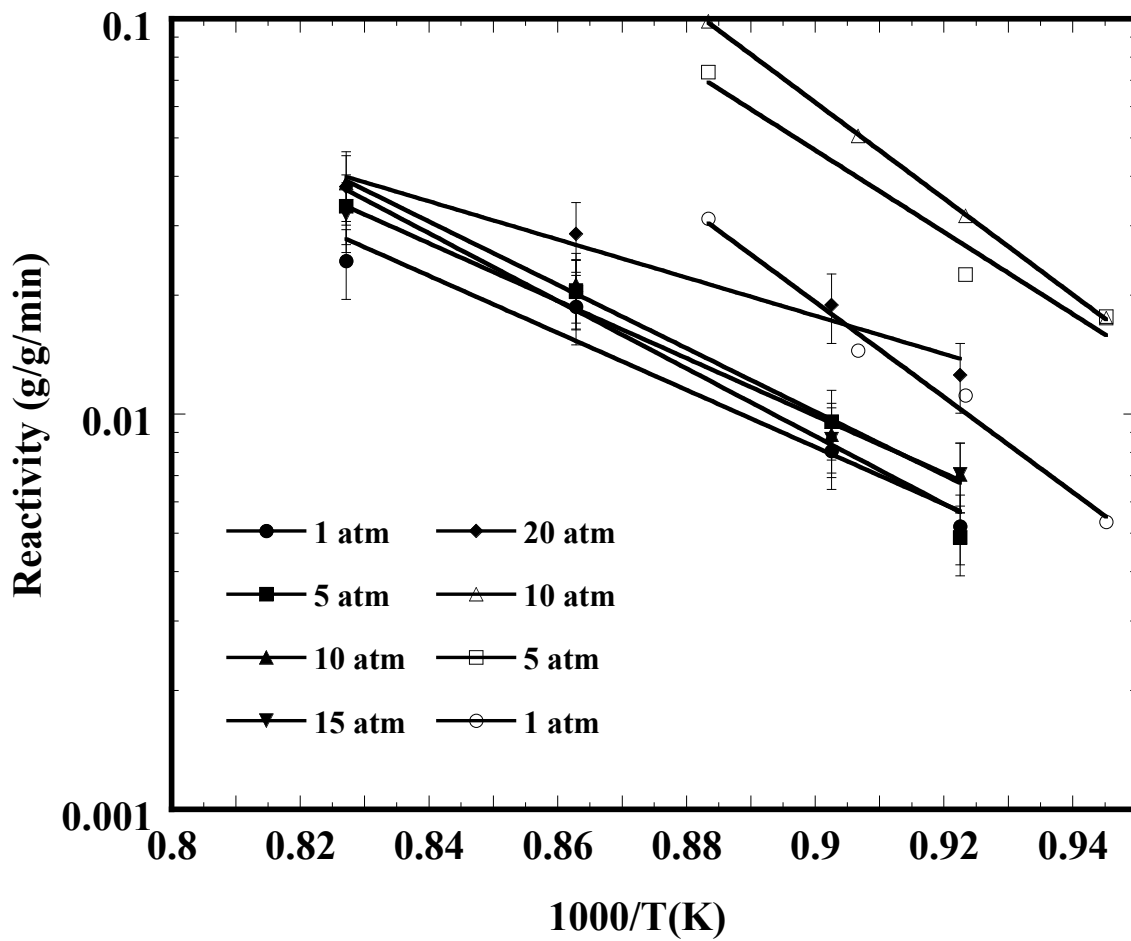


Figure 7.14 Arrhenius plots for Wyodak coal char as a function of total CO₂ pressure. The open symbols are for the Brown char, and the closed symbols for the BYU char.

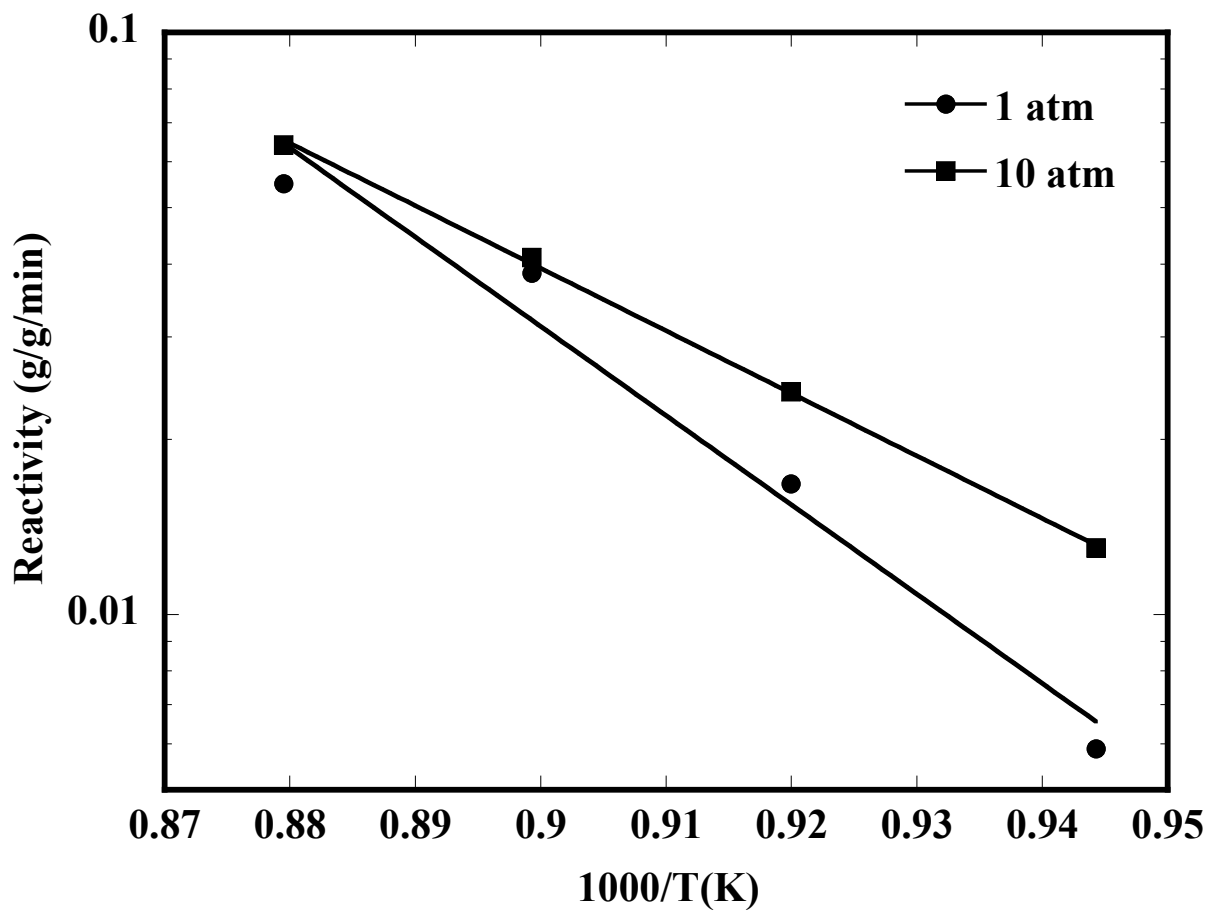


Figure 7.15 Arrhenius plots for Knife River coal char as a function of total CO₂ pressure.

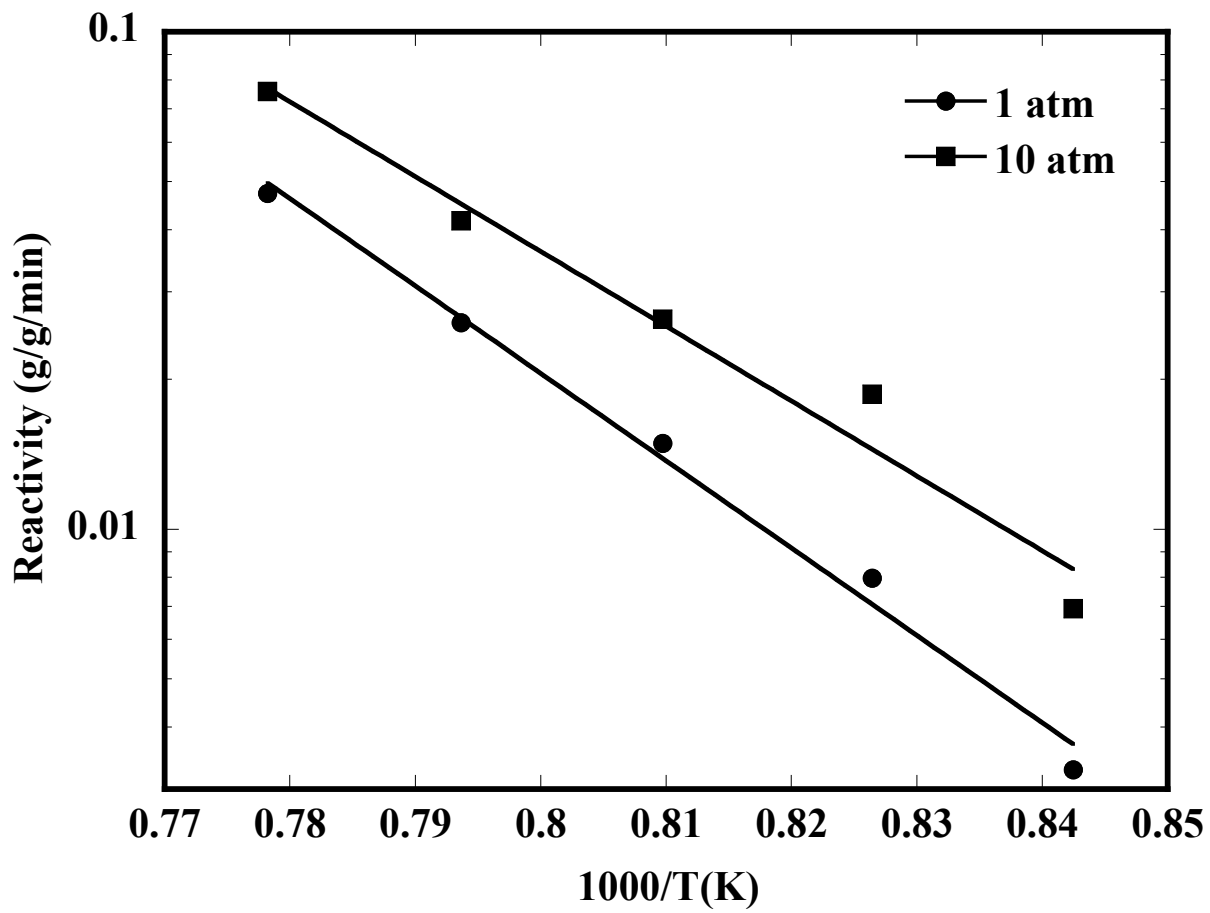


Figure 7.16 Arrhenius plots for Koonfontain coal char as a function of total CO₂ pressure.

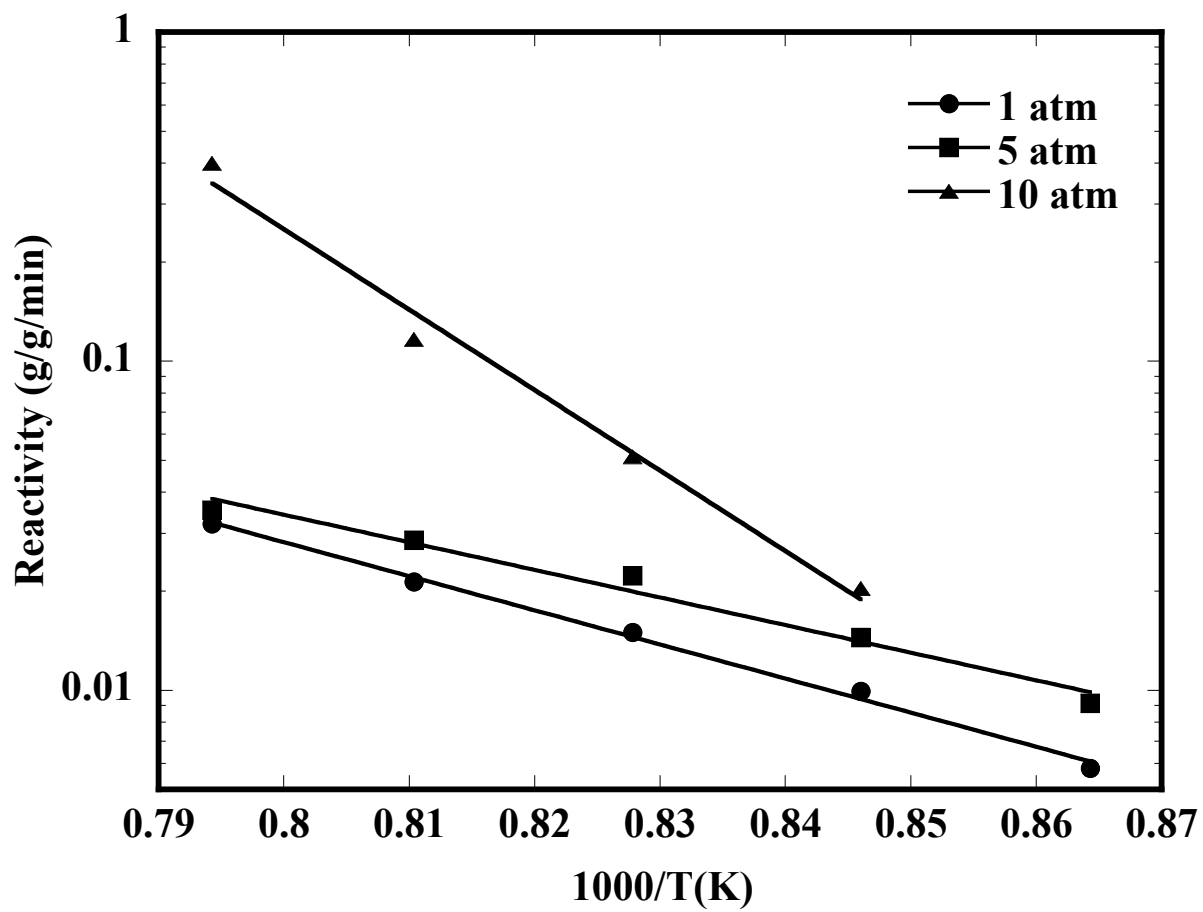


Figure 7.17 Arrhenius plots for Pittsburgh#8 coal char as a function of total CO₂ pressure.

Appendix 7A.

Brigham Young University Coal Chars Characterized at Brown University

Table 7A.1. Ultimate analysis of BYU samples.

Coal/Char	Ultimate Analysis (wt%, daf)				
	C	H	N	S	O
Knife River Lignite Coal	51.697	3.516	0.789	1.062	42.937
1 atm Knife River Lignite Char	60.043	1.002	0.621	0.815	37.520
6 atm Knife River Lignite Char	58.427	1.836	0.705	0.993	38.040
10 atm Knife River Lignite Char	40.897	0.904	0.347	1.905	55.947
Wyodak SubB Coal	62.227	4.804	0.855	0.417	31.698
1 atm Wyodak Char	77.137	1.347	0.627	0.123	20.767
6 atm Wyodak Char	98.907	0.894	0.120	0.083	-0.003
10 atm Wyodak Char	75.600	1.135	0.359	0.136	22.770
Koonfontain Coal	71.035	3.970	1.992	0.373	22.631
1 atm Koonfontain Char	77.070	0.769	1.670	0.043	20.448
6 atm Koonfontain Char	79.975	1.753	1.893	0.315	16.065
10 atm Koonfontain Char	84.713	1.519	1.460	0.140	12.168
Pittsburgh #8 Coal	78.067	5.055	1.854	0.454	14.570
1 atm Pittsburgh #8 Coal Char	78.173	1.226	1.781	0.576	18.244
6 atm Pittsburgh #8 Coal Char	72.750	1.457	1.661	0.591	23.541
10 atm Pittsburgh #8 Coal Char	59.507	2.239	0.578	0.833	36.843

Table 7A.2. Porosity characterization from CO₂ adsorption isotherms.

Coal Char/Flat Flame Burner Pressure	Dubinin-Radushkevich Analysis			BET Analysis
	Mean Pore Width (nm)	Micropore Volume (cm ³ /g)	Micropore Surface Area (m ² /g)	BET Surface Area (m ² /g)
Knife River Lignite Char				
1 atm	1.51	0.167	387	317
6 atm	1.69	0.109	252	215
10 atm	4.05	0.092	192	162
Wyodak SubB Coal Char				
1 atm	1.59	0.215	499	426
6 atm	1.67	0.190	440	403
10 atm	1.76	0.035	81.7	93.2
Koonfontain Coal Char				
1 atm	1.91	0.160	373	197
6 atm	1.66	0.123	286	221
10 atm	1.64	0.162	376	314
Pittsburgh #8 Coal Char				
1 atm	1.60	0.163	378	213
6 atm	1.67	0.190	440	403
10 atm	1.68	0.117	271	237

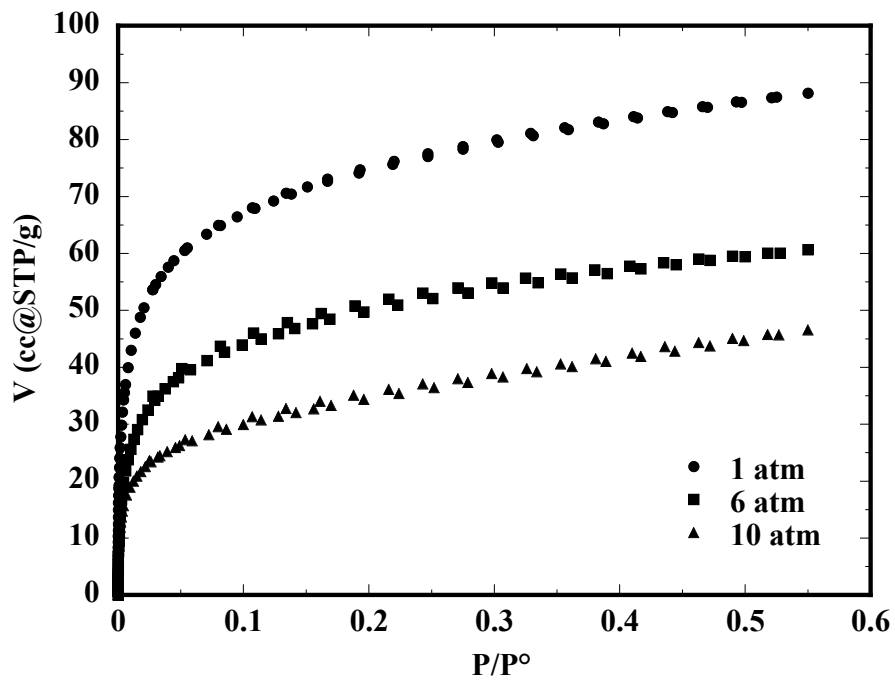


Figure 7A.1. CO₂ adsorption/desorption isotherms (195K – dry ice in acetone bath) of Knife River lignite char prepared at different pressures at BYU.

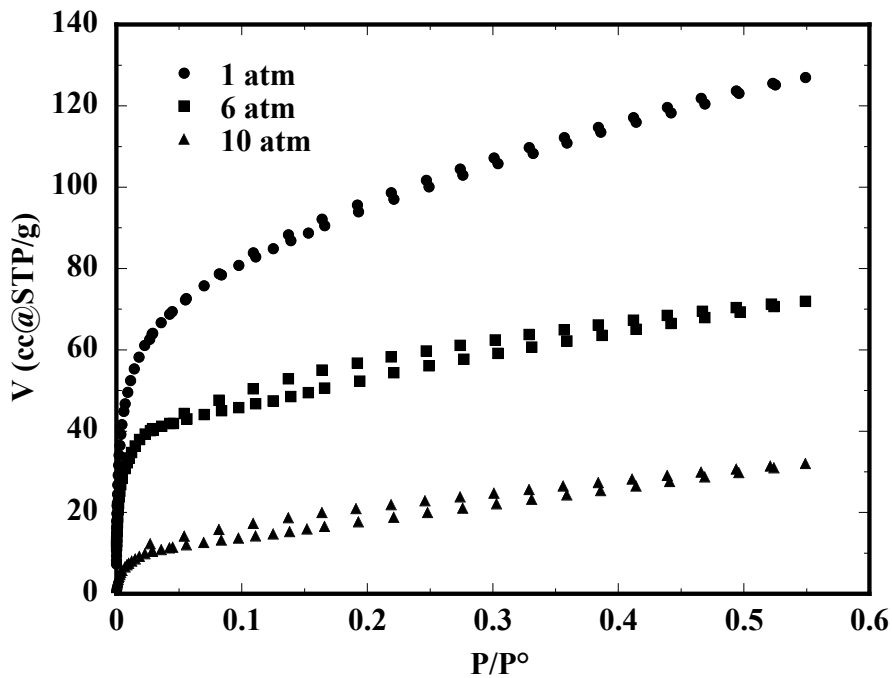


Figure 7A.2. CO₂ adsorption/desorption isotherms (195K – dry ice in acetone bath) of Wyodak coal char prepared at different pressures at BYU.

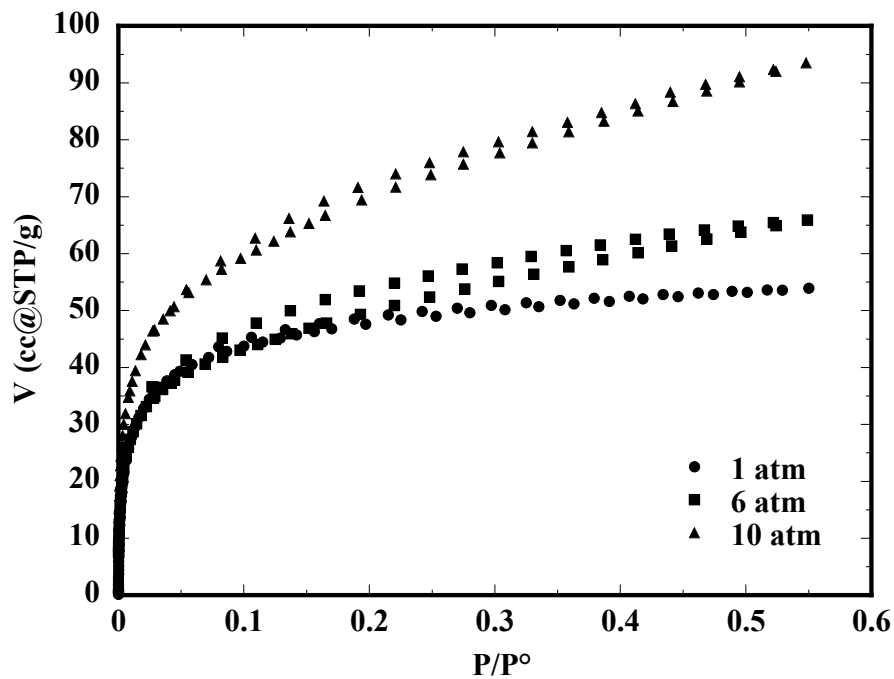


Figure 7A.3 CO₂ adsorption/desorption isotherms (195K – dry ice in acetone bath) of Koonfontain coal char prepared at different pressures at BYU.

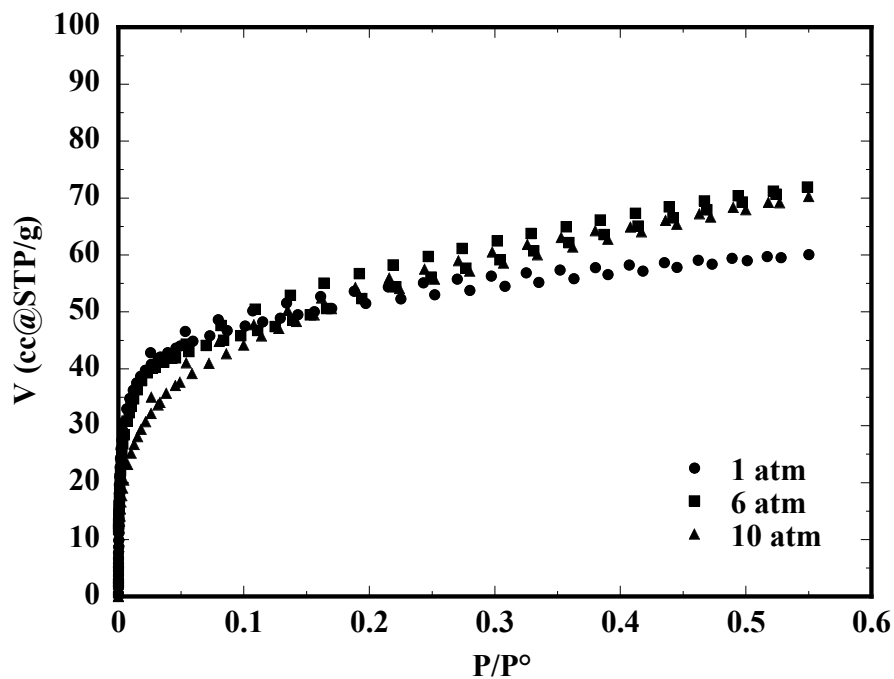


Figure 7A.4 CO₂ adsorption/desorption isotherms (195K – dry ice in acetone bath) of Pittsburgh #8 coal char prepared at different pressures at BYU.

CHAPTER 8

IMPLEMENTATION OF ADVANCED COAL COMBUSTION SUBMODELS INTO B&W'S CFD CODE

1 INTRODUCTION

The advanced coal combustion models, Chemical Percolation and Devolatilization (CPD) [Fletcher, 1992] and Carbon Burnout Kinetic (CBK) [Hurt, 1988] were modified as part of this project for inclusion in comprehensive computational CFD codes. These models were implemented as subroutines in B&W's proprietary CFD code, COMOSM. In order to realize the increased accuracy from these advanced models the coal/char constituent model was reformulated to allow variable rates of progress for different gaseous products during devolatilization and char oxidation. This report gives a technical specification for the interface between these models and related chemical processes and physical properties.

For consistency with the current software language conventions used in COMOSM both subroutines were converted to ANSI C with the revised versions submitted back to the originating authors. The change from FORTRAN to C follows the objected-oriented programming paradigm currently used in most major software development projects. For successful coupling to a CFD code, which solves the particle transport using a stiff ODE solver, it is necessary for the calls to the rate routines for the submodels to be idempotent (multiple calls to the subroutine yields the same result). The identification of the variables which constituted the descriptive states of the particles was a significant undertaking in the early part of the project. Further work is planned at B&W to further reduce the number of state variables by removal of variables which can be derived from independent variables thus reducing the amount of information which is to be transferred when particles are computed in parallel implementations.

2. THEORY

Particle Constituent Model

The coal composition is represented as water, ash and the principal organic elements (carbon, hydrogen, nitrogen, oxygen and sulfur). Prior to the implementation of the CPD model, the composition of coal was modeled with the constituents C, H, N, O, S, H₂O and ASH. The implementation of the CPD model necessitated the reformulation of the coal constituent model to include a new constituent C* which is used to partition the fuel carbon (carbon is partitioned between C and C*). The species C* is used to model the coal heat of formation such that the complete conversion of the Dry, Ash-Free (DAF) coal constituents (C, C*, H, N, O, S) to gaseous products produces the specified coal higher heating value.

The mass of the C* specie is assumed to be completely consumed during the devolatilization process. Only carbon in the form of C is allowed to remain since the heat of combustion of the constituent C is in good agreement with the measured heat of combustion of residual char samples (primarily composed of carbon). In the Arrhenius formulation all the DAF carbon is initially assigned to the C* constituent. Since the final devolatilization yield is specified a priori the C* is then converted to C (reaction 1) proportionally to the rate of devolatilization through equation 1.1. From a thermophysical perspective, C and C* are identical in both formulations, except for the heat of formation.



$$r_{C, \text{char}} = X_{C^*, \text{DAFF}}^0 r_{\text{devol}} \quad 1.1$$

where

$$X_{C^*, \text{DAFF}}^0 = \text{initial DAF coal carbon mass fraction } (kg_{C^*} / kg_{\text{DAFF}})$$

$$r_{\text{devol}} = \text{rate of devolatilization } (kg_{\text{DAFF}} / s)$$

When the CPD model is used the initial amount of the specie C* is modeled as the amount of initial carbon present in the form of labile bridges. The mass of this specie is assumed to be completely consumed during the devolatilization process at the rate of labile bridge transformation via equation 1.2.

$$r_C = -\frac{dC^*}{dt} \equiv -\frac{d\xi}{dt} \quad 1.2$$

where

$$\frac{d\xi}{dt} = \text{rate of labile bridge transformation (kg}_{DAFF} \text{ s}^{-1}\text{)}$$

The heat of formation of C* for both devolatilization submodels is determined from equation 1.3:

$$\Delta H_{f,C^*} = \frac{\Delta H_{comb} - \sum_{j=1, \text{cons} \neq C^*}^{N_{org. \text{ cons.}}} \Delta H_{f,j} X_{j,DAFF}^0}{X_{C^*,DAFF}^0} \quad 1.3$$

where

$$\Delta H_{comb} = \text{heat of combustion of DAF coal (J kg}_{DAFF}^{-1}\text{)}$$

$$N_{org. \text{ cons.}} = \text{number of organic fuel constituents}$$

$$X_{j,DAFF}^0 = \text{initial DAF organic fuel constituent mass fraction ()}$$

$$X_{C^*,DAFF}^0 = \text{initial DAF C* mass fraction ()}$$

Particle Energy Balance

The particle energy balance is modeled as the sum of convective heat transfer between the local gas environment, radiative heat transfer from incident radiant energy and particle absorption/emission and energy transfer occurring through chemical reactions.

The governing equation for the particle energy balance is written as follows:

$$\frac{d}{dt}(m_p h_p) = Q_{conv} + Q_{rad} + \sum_{k=1}^{N_R} r_k \sum_{j=1}^{N_{gs}} (\bar{c}_{jk} \hat{h}_j(T_g) - \bar{c}_{jk} \hat{h}_j(T_p)) \hat{M}_j \quad 1.4$$

where

$m_p =$	particle mass (kg)
$h_p =$	particle enthalpy ($J kg^{-1}$)
$Q_{conv} =$	convective heat transfer to the particle (W)
$Q_{rad} =$	radiative heat transfer to the particle (W)
$N_R =$	number of chemical reactions
$r_i =$	rate of reaction i ($kg s^{-1}$)
$N_{gs} =$	number of gas species
$\nu_{jk} =$	stoichiometric coefficients of reactant species j
$\hat{h}_j =$	molar enthalpies ($J kmol^{-1}$)
$T_g =$	gas temperature (K)
$\nu'_{jk} =$	stoichiometric coefficients of product species j
$T_p =$	particle temperature (K)
$\hat{M}_j =$	relative molecular weight ($kg kmol^{-1}$)

Differentiation of the LHS by parts:

$$\begin{aligned} \frac{d}{dt}(m_p h_p) &= \frac{d}{dt} \sum_{j=1}^{N_{cons.}} m_j h_j(T_p) = \sum_{j=1}^{N_{cons.}} m_j \frac{dh_j}{dt} + \sum_{j=1}^{N_{cons.}} h_j \frac{dm_j}{dt} \\ &= m_p \frac{dh_p}{dt} + \sum_{j=1}^{N_{cons.}} \hat{M}_j \sum_{k=1}^{N_R} r_k (\nu'_{jk} \hat{h}_j - \nu_{jk} \hat{h}_j) \end{aligned} \quad 1.5$$

where

$$N_{cons.} = \text{number of solid constituents}$$

Combining Eq. 1.4 with Eq. 1.5 results in

$$m_p \frac{dh_p}{dt} = Q_{conv} + Q_{rad} + \sum_{k=1}^{N_R} r_k \underbrace{\sum_{j=1}^{N_{gs}} (\nu'_{jk} \hat{h}_j(T_g) - \nu_{jk} \hat{h}_j(T_p)) \hat{M}_j + \sum_{j=1}^{N_{cons.}} (\nu'_{jk} \hat{h}_j(T_p) - \nu_{jk} \hat{h}_j(T_p)) \hat{M}_j}_{\sum H_k} \quad 1.6$$

where

$$N_{gs} = \text{number of gas species}$$

Over the time interval Δt of numerical integration (Equation 1.7) the particle specific

heat is modeled as a constant:

$$m_p \frac{dh_p}{dt} = m_p \frac{d}{dt} \left[h(T_o) + \int_{T_o}^{T_p} c_p dT \right] = m_p c_p \frac{dT_p}{dt} \quad 1.7$$

where

$$c_p = \text{heat capacity of the particle } (J kg^{-1} K^{-1})$$

$$\frac{dT_p}{dt} = \text{rate of change in particle temperature } (K s^{-1})$$

For small time steps, the error introduced by the assumption of constant specific heat during the time-step is negligible. The latent heat of phase change (moisture evaporation and devolatilization) must be accounted for in the heat of formations of reactants and products. Except for the thermophysical properties of tar, the latent heat of devolatilization is neglected since the gaseous products are formed from pure elemental constituents. To explicitly account for the latent heat of vaporization the constituent model would have to be modified to include solid constituents with heat of formations which realize the change in enthalpy when the solid constituents are released as gaseous products.

Convective Heat Transfer Rate : The convective heat transfer rate Q_{conv} is defined as:

$$Q_{conv} = h A_p (T_g - T_p) \quad 1.8$$

where

$$h = \text{convective heat transfer coefficient } (W m^{-2} K^{-1})$$

$$A_p = \text{particle surface area } (m^2)$$

The heat transfer coefficient h is defined as:

$$h = \frac{\Gamma \cdot Nu \cdot k_g}{d_p} \quad 1.9$$

where :

$$\Gamma = \text{mass transfer number } (\Gamma)$$

$$Nu = \text{Nusselt number } (\Gamma)$$

$$k_g = \text{gas thermal conductivity } (W m^{-1} K^{-1})$$

The Γ term represents the effects of high mass transfer on the convective heat transfer coefficient [Spalding, 1955], and is defined by the following equation:

$$\Gamma = B / (e^B - 1) \quad 1.10$$

where the transfer number B for heat transfer is defined by:

$$B = \frac{c_{Pg}}{2\Gamma d_p k_g} \frac{dm_p}{dt} \quad 1.11$$

where: c_{pg} = gas heat capacity ($J m^{-1} K^{-1}$).

The Nusselt number is given by :

$$Nu_{ht} = 2 + 0.6 Re_d^{1/2} Pr^{1/3} \quad 1.12$$

where

Re_d = Reynolds number based on the particle diameter and relative velocity of continuous phase (\square)

Pr = Prandtl number (\square)

Currently the Prandtl number is approximated as 0.7. The gas thermal conductivity k_g is calculated based on the local film temperature T_{film} , modeled as the arithmetic mean:

$$T_{film} = \frac{T_g + T_p}{2} \quad 1.13$$

Radiative Heat Transfer Rate : The radiative heat transfer rate Q_{rad} is defined as:

$$Q_{rad} = \square_p A_p (\square_{bb} \square \square \cdot T_p^4) \quad 1.14$$

where

\square = Stefan-Boltzman constant ($5.67 \cdot 10^{28} W m^{-2} K^{-4}$)

\square_p = particle emissivity (\square)

\square_{bb} = radiative flux to particle ($W m^{-2}$)

General Model Formulation

Material balances for Lagrangian particles are simply written as

$$\frac{dm_i}{dt} = \hat{M}_i \sum_{k=1}^{N_R} r_k \sum_{j=1}^{N_{cons.}} (\square_{kj}^* \square \square_{kj}) n_{ij} \quad 1.15$$

where

n_{ij} = moles of constituent i per mole of solid species j

\hat{M}_i = molecular weight of constituent i

with initial conditions $m_i = m_i^o$ at the start of the particle trajectory, $t=0$, and

$m_p = \sum_{L=1}^{N_{cons.}} m_L$ is the total particle mass where $L = \{C, H, N, O, S, H_2O, Ash, C^*\}$.

Auxiliary transport equations for initial coal mass (m_{coal}^o) and initial char mass (m_{char}^o) may be required to determine particle properties (diameter, number concentration, surface area, density, etc.) used to calculate heterogeneous reaction rates. They are never used directly for overall mass and material balances.

For Lagrangian particles, these quantities are known a priori or determined later along the particle trajectory.

Overview of Particle Lifetime

The particle life is modeled as a sequence of particle conversion modes which are particle heat-up, moisture evaporation, devolatilization, char combustion and inert ash transport. For low-rank coals there may be overlap between the devolatilization and char combustion modes. Currently, the possible overlap is not accounted for in the particle conversion modes during Lagrangian calculations; overlap is permitted during Eulerian particle calculations.

Particle Heatup

During the particle heat-up period (before evaporation of moisture) the particle temperature typically increases due to convective and radiative heat transfer. The only particle property which varies during this period is the particle heat capacity which is temperature dependent.

$$m_p c_p \frac{dT_p}{dt} = Q_{conv} + Q_{rad} \quad 1.16$$

Moisture Evaporation Rate

The rate of evaporation is given by:



$$r_{evap} = N_{H_2O} A_p M_{H_2O} \quad 1.17$$

where

$$N_{H_2O} = \text{molar flux of vapor } (kmol m^{-2} s^{-1})$$

The molar flux of vapor is given by:

$$N_{H_2O} = A_p \frac{Nu k_{gas}}{d_p c_{p, gas}} (C_{H_2O,s} - C_{H_2O,\infty}) \quad 1.18$$

where

$$C_{H_2O,s} = \text{water vapor concentration at the particle surface } (kmol m^{-3})$$

$$C_{H_2O,\infty} = \text{water vapor concentration in the bulk gas } (kmol m^{-3})$$

The water vapor concentration at the particle surface is modeled as :

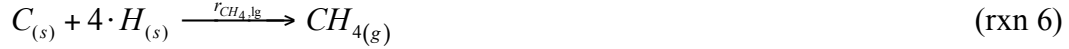
$$C_{H_2O,s} = \frac{P_{sat}(T_p)}{R_{gas} T_p} \quad 1.19$$

Coal Devolatilization

The CPD model has been incorporated into COMOSM for the prediction of coal devolatilization. This model uses percolation theory and correlations based on readily available proximate and ultimate analyses to model the coal particle devolatilization. Modifications were made to the original CPD formulation by [Perry, 2000] to predict evolution of nitrogen species. Modifications were made during this project to allow the routine to be used to return rate of progress of gaseous species evolution at the beginning of an arbitrary time step. The heterogeneous reaction steps for the transformation of particle constituents are given by reactions 4-15:

Light gas reactions:





Tar reactions:



In the CPD model, the coal structure breaks down into a distribution of char, metaplast, tar and light gases. The metaplast fraction is released into the gas phase as tar or cross-linked into the char structure. The CPD model distributes the fraction of the particle mass released as light gases into H₂O, CO, CO₂, CH₄, and “other” through the use of a look-up table based on the work of Xu and Tomita [ref]. In Eq. 1.20 the “other” fraction has been modeled as C₂H₄.

$$f_{lg} = f_{H_2O} + f_{CO} + f_{CO_2} + f_{CH_4} + f_{C_2H_4} \quad 1.20$$

H₂S evolution is assumed to be proportional to light gas release according to Eq. 1.21. The fraction of particle mass evolved as HCN (f_{HCN}) is given directly as an output of the CPD model. The NH₃/HCN ratio is available as a user specified constant.

$$f_{H_2S} = f_S^o \cdot f_{lg} \cdot \frac{\hat{M}_{H_2S}}{\hat{M}_S} \quad 1.21$$

With the current constituent model in COMOSM it is necessary to specify the elemental composition of the tar which is fixed during the devolatilization of the particle. This is accomplished in a preprocessing step by integrating the light gas evolution over an arbitrary temperature profile and setting the tar composition equal to the original particle composition less the composition of the light gas products (char and tar are assumed to be equal in composition). The molecular weight of the tar is obtained from the preprocessing step as the average tar molecular weight calculated from the CPD model. Since the thermochemical information of species is specified into COMOSM using JANAF polynomial databases, the hydrocarbon portion of the tar is input as a newly created specie “TAR” and the residual oxygen and sulfur are represented as separate species. It is currently considered not worthwhile to create an agglomerate specie which contains all the organic elements since this can not be represented as a JANAF database and would require a major development effort.

The total particle mass for an arbitrary time step is determined by Eq. 1.22.

$$m_{p,t+\Delta t} = m_{p,t} + \Delta t \cdot \left[\frac{dm_{p,tar}}{dt} + \frac{dm_{p,lg}}{dt} + \frac{dm_{p,H_2S,HCN\&NH_3}}{dt} \right] \quad 1.22$$

The elemental composition is determined from Eq. 1.23 for each element e

where $e = \{C, H, N, O, S\}$

$$m_{pe,t+\Delta t} = m_{pe,t} + \Delta t \cdot \left[\frac{dm_{pe,tar}}{dt} + \frac{dm_{pe,lg}}{dt} + \frac{dm_{pe,H_2S,HCN\&NH_3}}{dt} \right] \quad 1.23$$

The amounts of elements C, H, O & S remaining after the complete light gas evolution are determined by Eqs. 1.24-1.27 where the f_C^r indicates the total final yield of each product and the r indicates the remaining fraction of the elemental composition which is either released as tar or incorporated into the final char solid matrix.

$$f_C^r = f_C^o \left[f_{CO} \cdot \frac{\hat{M}_C}{\hat{M}_{CO}} + f_{CO_2} \cdot \frac{\hat{M}_C}{\hat{M}_{CO_2}} + f_{CH_4} \cdot \frac{\hat{M}_C}{\hat{M}_{CH_4}} + f_{C_2H_4} \cdot \frac{2 \cdot \hat{M}_C}{\hat{M}_{C_2H_4}} + f_{HCN} \cdot \frac{\hat{M}_C}{\hat{M}_{HCN}} \right] \quad 1.24$$

$$f_H^r = f_H^o \begin{bmatrix} \square \\ \square \\ \square \\ \square \end{bmatrix} f_{H_2O} \cdot \frac{\hat{M}_{H_2}}{\hat{M}_{H_2O}} + f_{CH_4} \frac{4 \cdot \hat{M}_H}{\hat{M}_{CH_4}} + f_{C_2H_4} \frac{4 \cdot \hat{M}_H}{\hat{M}_{C_2H_4}} + f_{HCN} \frac{\hat{M}_H}{\hat{M}_{HCN}} + f_{H_2S} \frac{2 \cdot \hat{M}_H}{\hat{M}_{H_2S}} \begin{bmatrix} \square \\ \square \\ \square \\ \square \end{bmatrix} \quad 1.25$$

$$f_O^r = f_O^o \begin{bmatrix} \square \\ \square \\ \square \\ \square \end{bmatrix} f_{CO} \cdot \frac{\hat{M}_O}{\hat{M}_{CO}} + f_{CO_2} \cdot \frac{\hat{M}_{O_2}}{\hat{M}_{CO_2}} + f_{H_2O} \cdot \frac{\hat{M}_O}{\hat{M}_{H_2O}} \begin{bmatrix} \square \\ \square \\ \square \\ \square \end{bmatrix} \quad 1.26$$

$$f_S^r = f_S^o \begin{bmatrix} \square \\ \square \\ \square \\ \square \end{bmatrix} f_{H_2S} \frac{\hat{M}_S}{\hat{M}_{H_2S}} \quad 1.27$$

The particle elemental composition due to tar and "other" light gas evolution is given by Eqs. 1.28-1.35. As previously stated, the stoichiometric coefficients \square_{tar} are given as input. The rates of particle elemental conversion in the following equations are the modifications which were made to the CPD model as part of this project and are tracked internal to the CPD model. The rate of nitrogen conversion uses existing expressions already present in the CPD model.

$$\frac{dm_{p_{C,tar}}}{dt} = \begin{bmatrix} \square \\ \square \\ \square \\ \square \end{bmatrix} \frac{dm_{p_{tar}}}{dt} \begin{bmatrix} \square \\ \square \\ \square \\ \square \end{bmatrix} \frac{dm_{p_{N,tar}}}{dt} \begin{bmatrix} \square \\ \square \\ \square \\ \square \end{bmatrix} \square_{C,tar} \quad 1.28$$

$$\frac{dm_{p_{C,lg}}}{dt} = \frac{dm_{p_{lg}}}{dt} \cdot \begin{bmatrix} \square \\ \square \\ \square \\ \square \end{bmatrix} \frac{X_{CO} \cdot \hat{M}_C}{\hat{M}_{CO}} + \frac{X_{CO_2} \cdot \hat{M}_C}{\hat{M}_{CO_2}} + \frac{X_{CH_4} \cdot \hat{M}_C}{\hat{M}_{CH_4}} + \frac{X_{C_2H_4} \cdot 2 \cdot \hat{M}_C}{\hat{M}_{C_2H_4}} \begin{bmatrix} \square \\ \square \\ \square \\ \square \end{bmatrix} \quad 1.29$$

$$\frac{dm_{p_{H,tar}}}{dt} = \begin{bmatrix} \square \\ \square \\ \square \\ \square \end{bmatrix} \frac{dm_{p_{tar}}}{dt} \begin{bmatrix} \square \\ \square \\ \square \\ \square \end{bmatrix} \frac{dm_{p_{N,tar}}}{dt} \begin{bmatrix} \square \\ \square \\ \square \\ \square \end{bmatrix} \square_{H,tar} \quad 1.30$$

$$\frac{dm_{p_{H,lg}}}{dt} = \frac{dm_{p_{lg}}}{dt} \cdot \begin{bmatrix} \square \\ \square \\ \square \\ \square \end{bmatrix} \frac{X_{CH_4} \cdot 4 \cdot \hat{M}_H}{\hat{M}_{CH_4}} + \frac{X_{H_2O} \cdot 2 \cdot \hat{M}_H}{\hat{M}_{H_2O}} + \frac{X_{C_2H_4} \cdot 4 \cdot \hat{M}_H}{\hat{M}_{C_2H_4}} \begin{bmatrix} \square \\ \square \\ \square \\ \square \end{bmatrix} \quad 1.31$$

$$\frac{dm_{p_{O,tar}}}{dt} = \begin{bmatrix} \square \\ \square \\ \square \\ \square \end{bmatrix} \frac{dm_{p_{tar}}}{dt} \begin{bmatrix} \square \\ \square \\ \square \\ \square \end{bmatrix} \frac{dm_{p_{N,tar}}}{dt} \begin{bmatrix} \square \\ \square \\ \square \\ \square \end{bmatrix} \square_{O,tar} \quad 1.32$$

$$\frac{dm_{p_{O,lg}}}{dt} = \frac{dm_{p_{lg}}}{dt} \cdot \begin{bmatrix} \square \\ \square \\ \square \\ \square \end{bmatrix} \frac{X_{CO} \cdot \hat{M}_O}{\hat{M}_{CO}} + \frac{X_{CO_2} \cdot 2 \cdot \hat{M}_O}{\hat{M}_{CO_2}} + \frac{X_{H_2O} \cdot \hat{M}_O}{\hat{M}_{H_2O}} \begin{bmatrix} \square \\ \square \\ \square \\ \square \end{bmatrix} \quad 1.33$$

$$\frac{dm_{pS,tar}}{dt} = \frac{dm_{p,tar}}{dt} - \frac{dm_{pN,tar}}{dt} \quad 1.34$$

$$\frac{dm_{pS,lg}}{dt} = 0 \quad 1.35$$

The source terms for the gas phase conservation equations may be derived from rates of progress given in eqs. 1.36-1.43 with the particle conversion rates and fractional distribution determined by the CPD model.

$$r_{CH_4,lg} = \frac{dm_p}{dt} \cdot f_{CH_4} \quad 1.36$$

$$r_{C_2H_4,lg} = \frac{dm_p}{dt} \cdot f_{C_2H_4} \quad 1.37$$

$$r_{CO,lg} = \frac{dm_p}{dt} \cdot f_{CO} \quad 1.38$$

$$r_{CO_2,lg} = \frac{dm_p}{dt} \cdot f_{CO_2} \quad 1.39$$

$$r_{H_2O,lg} = \frac{dm_p}{dt} \cdot f_{H_2O} \quad 1.40$$

$$r_{HCN,lg} = \frac{dm_p}{dt} \cdot f_{HCN} \quad 1.41$$

$$r_{H_2S,lg} = \frac{dm_p}{dt} \cdot f_{H_2S} \quad 1.42$$

$$r_{tar} = \frac{dm_p}{dt} \cdot f_{tar} \quad 1.43$$

During devolatilization the particle diameter changes due to coal particle swelling. For sub-bituminous coals volatile evolution proceeds at a slow rate long after the initial yield due to internal cracking and distillation processes. The initial particle mass is given by:

$$m_p^o = m_{pH_2O}^o + m_{pash}^o + m_{pcoal,dry}^o \quad 1.44$$

Devolatilization Termination Criteria: Since the current implementation doesn't allow overlap of stages it is necessary to specify the criteria for the termination of the devolatilization. In particular, low-rank western coals continue to devolatilize, albeit at a slower rate for long periods after the labile bridges are consumed. The criteria adopted was to terminate the devolatilization stage if 1) all the labile bridges have been destroyed:

$$\xi = 0 \quad 1.45$$

and if the rate of O₂ diffusion to the particle is greater than the rate of devolatilization:

$$r_{diff} = \frac{2 D_{ab} A_p M_{O_2} C_{H_2O}}{m_p d_p} \quad 1.46$$

where:

A_p = particle area (m^2)

m_p = particle mass (kg)

d_p = particle diameter (m)

D_{ab} = binary diffusivity of O₂ in N₂ ($m^2 s^{-1}$), given by:

$$D_{ab} = 2.851 \cdot 10^{-4} \left[\frac{T_p + T_g}{2} \right]^{1.65} P_{Atm} \quad 1.47$$

where:

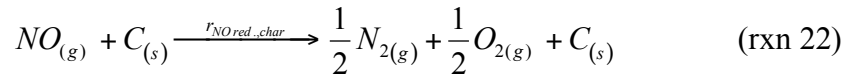
P_{Atm} = ambient pressure (Atm)

Char Oxidation

The CBK model was implemented as a submodel in COMOSM in order to obtain more accurate predictions of char burnout. The CBK was developed specifically to account for the reduction in char reaction rates through thermal annealing and ash inhibition effects which cause char conversion to be overpredicted in the submodel based on the formulation of Field.

Since the bulk of the organic char matrix is carbon and relative changes in the stoichiometric coefficients are thought to have a negligible impact on predictions the

stoichiometric distribution of the products is held constant relative to the initial stoichiometric distribution at the onset of char oxidation. The char reaction mechanism is given by reactions 15-22:



Char carbon reacts to form CO and CO₂ with a molar ratio determined by:

$$\frac{N_{CO}}{N_{CO_2}} = A_C \cdot e^{\frac{-E_c}{RT_p}} \quad 1.48$$

The rates of reactions 16 & 17 are determined directly from the rate of char combustion q_c obtained from the CBK model according to eqs. 1.49-1.50 as:

$$r_{CO, char} = \frac{N_{CO}}{N_{CO} + N_{CO_2}} \cdot q_c \cdot \frac{\Delta \cdot dp^2}{2} \quad 1.49$$

$$r_{CO_2, char} = \frac{N_{CO_2}}{N_{CO} + N_{CO_2}} \cdot q_c \cdot \frac{\Delta \cdot dp^2}{2} \quad 1.50$$

The rates of reactions 18-23 are obtained by maintaining the initial char stoichiometric distribution according to eqs. 1.51-1.55.

$$r_{H_2O,char} = \frac{1}{2} (r_{CO,char} + r_{CO_2,char}) \cdot \frac{m_{p,H}}{m_{p,C}} \quad 1.51$$

$$r_{O_2,char} = (r_{CO,char} + r_{CO_2,char}) \cdot \frac{m_{p,O}}{m_{p,C}} \quad 1.52$$

$$r_{SO_2,char} = (r_{CO,char} + r_{CO_2,char}) \cdot \frac{m_{p,S}}{m_{p,C}} \quad 1.53$$

$$r_{N_2,char} = (r_{CO,char} + r_{CO_2,char}) \cdot \frac{m_{p,N}}{m_{p,C}} \cdot (1 - f_{NO,char}) \quad 1.54$$

$$r_{NO,char} = (r_{CO,char} + r_{CO_2,char}) \cdot \frac{m_{p,N}}{m_{p,C}} \cdot f_{NO,char} \quad 1.55$$

The particle density during char combustion is determined through the char burning mode α according to Eq. 1.56.

$$\frac{\alpha}{\alpha_{char}^0} = \frac{m_p}{m_{p,char}^0} \quad 1.56$$

The particle diameter is determined by Eq. 1.57.

1.57

$$\frac{d_p}{d_{p,char}^0} = \left(\frac{m_p}{m_{p,char}^0} \right)^{(1-\alpha)/3}$$

RESULTS

Sandia CDL

To test the accuracy of the devolatilization reactions of COMOSM using the CPD model the laminar flow experiments conducted in the Sandia CDL were modeled [Fletcher, 1992]. A 2D model was developed for the calculations consisting of a 3x1000 element mesh. The measured gas temperature and velocity profiles were approximated with polynomials which were subsequently used to initialize the elements of the model. The particle trajectory was then calculated while holding the gas temperature, velocity and composition constant. Shown below are the predictions for a single particle (115 μm) and measured temperatures (106-125 μm) of New Mexico Blue #1 in the nominal 1050 K gas temperature environment. In Figure 1 it is seen that the predicted particle temperatures are in reasonable agreement.

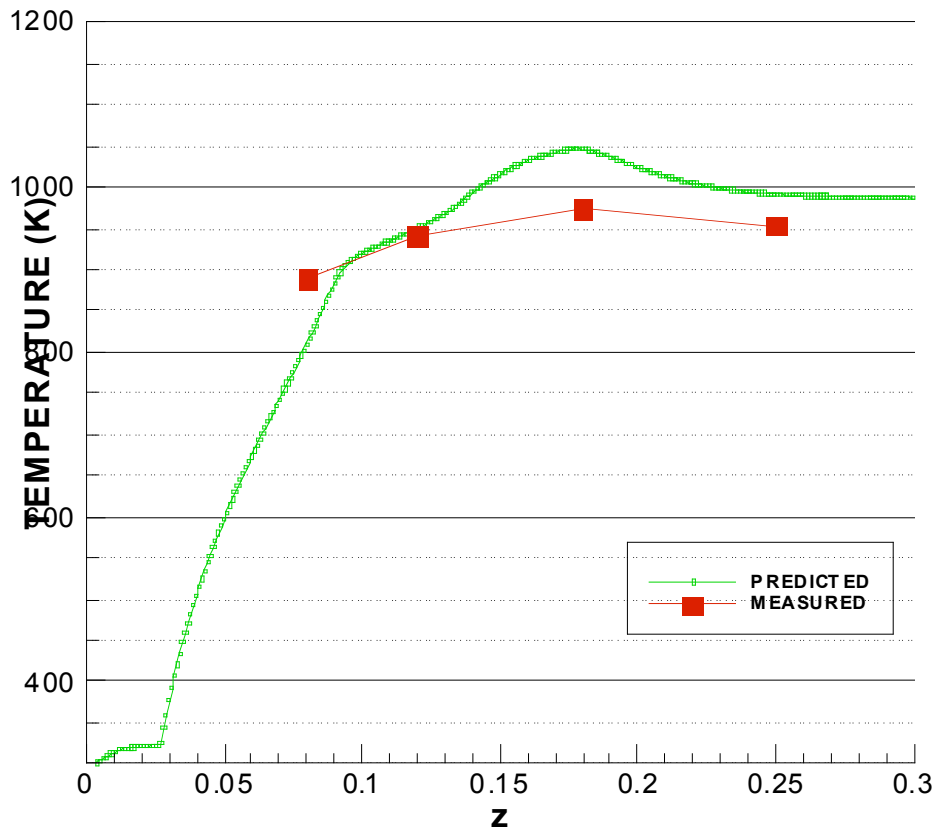


Figure 8.1. Predicted and Measured Particle Temperatures for New Mexico Blue #1 (PSOC-1445D) in 1050 K Gas Environment.

To understand the particle temperature the components of the particle energy transfer equation are computed for each time-step during the integration of the particle trajectory. It is observed in Figure 2 that initially the heat of reaction is endothermic which corresponds to the evaporation of moisture. During the late stages of devolatilization (around $z = 0.15$ m) the formation of the gaseous products from the solid fuel constituents causes the prediction of an exothermic reaction enthalpy. These exothermic transformations account for the predicted particle temperature overshoot shown in Figure 1.

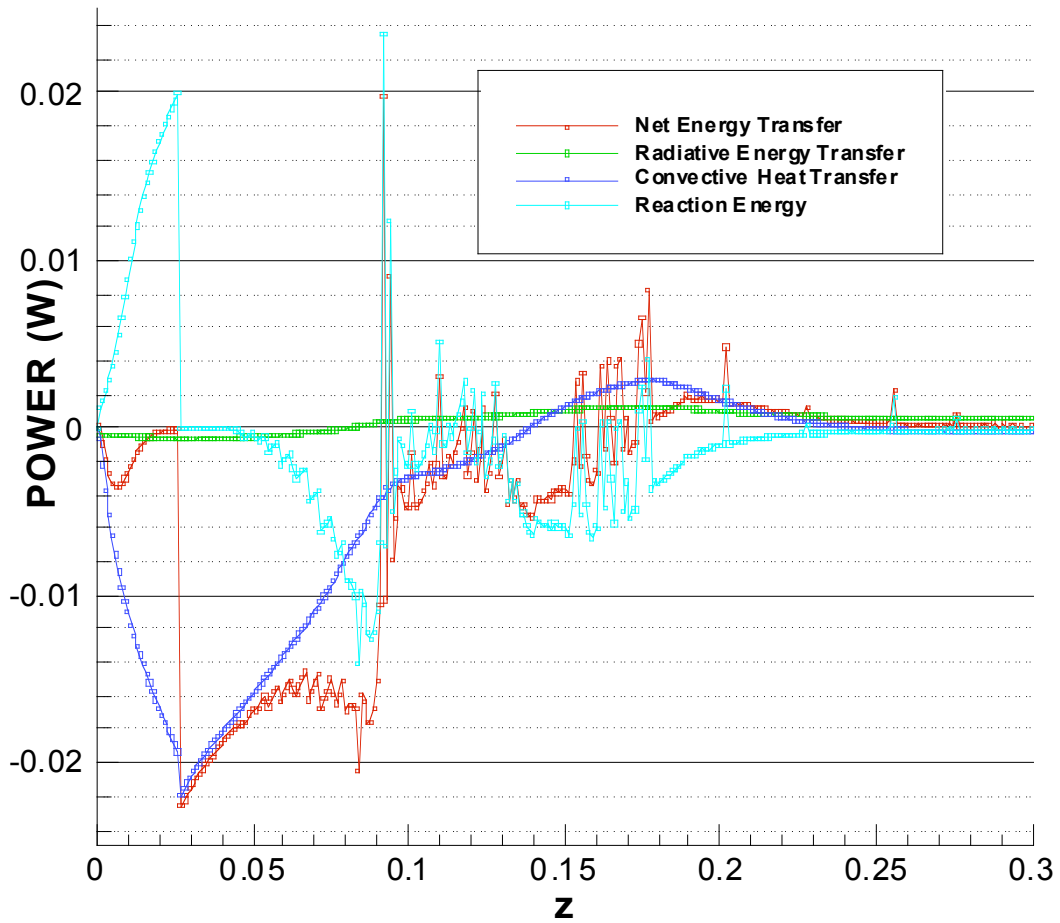


Figure 8.2. Predicted Energy Transfer for New Mexico Blue #1 (PSOC-1445D) in 1050 K Gas Environment.

The predicted rates of progress for each of the devolatilization reactions is shown in Figure 3. Several reactions occur in parallel during the devolatilization. Future internal development at B&W will modify the constituent model to incorporate organic forms of oxygen (carbonyl, carboxyl and hydroxyl) and hydrogen (hydrogen and aliphatic) so that the transformation of the solid fuel reactants to gaseous products provides a better thermochemical model (less exothermic/endothermic) of the devolatilization process.

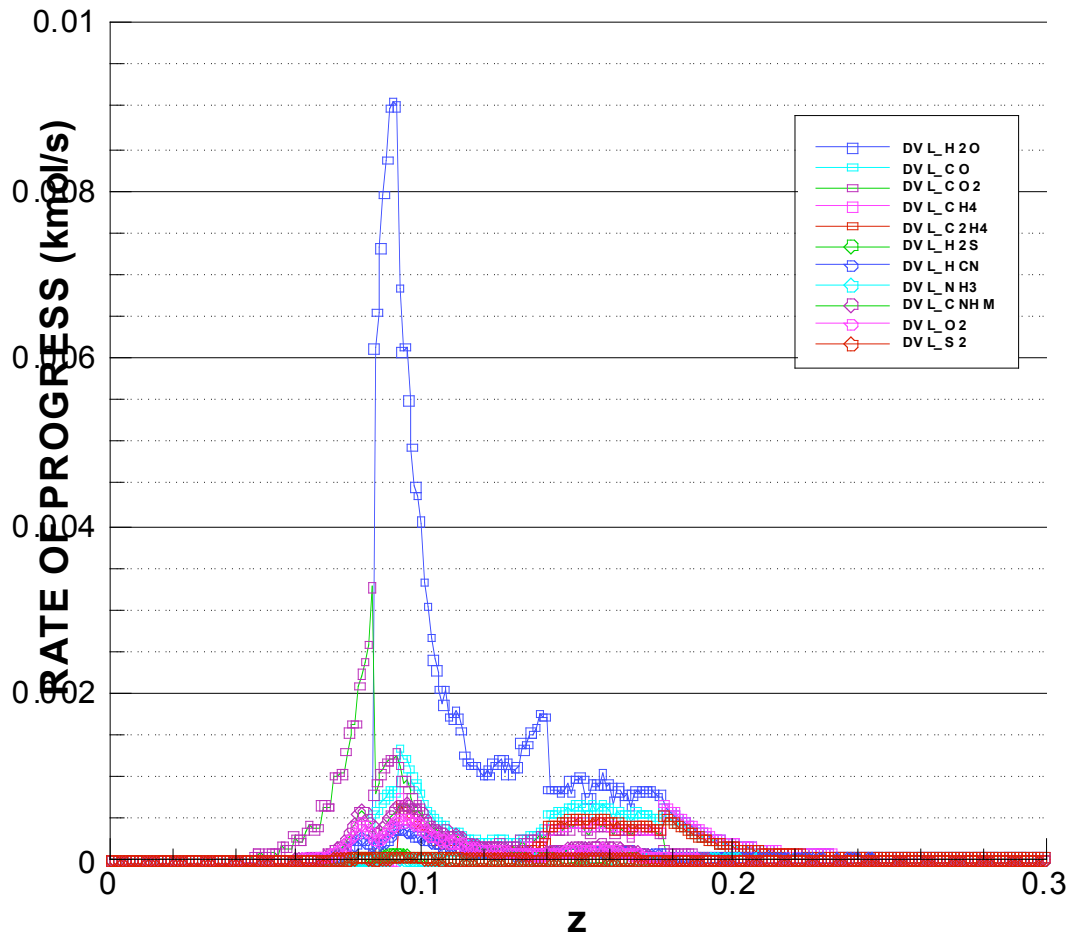


Figure 8.3. Predicted Rates of Progress for Devolatilization Constituents for New Mexico Blue #1 (PSOC-1445D) in 1050 K Gas Environment.

BYU PC Combustion Validation Cases

The introduction of the CPD and CBK models has brought the PC combustion modeling capabilities up to the state-of-the-art. During the design and implementation of the submodels, a decision was made to permit the new models to co-exist and to be applied interchangeably with the existing heterogeneous submodels for devolatilization and char oxidation – models of Ubhayaker, et al. (1975) and Field (1967), respectively. In addition

to providing a transition, this approach allows a side-by-side comparison of the models and their various permutations.

Table 1 – Description of Cases

Case	Devolatilization model	Char oxidation model
1 : ubhay-field	Ubhayaker	Field
2 : cpd-field	CPD	Field
3 : cpd-cbk	CPD	CBK

Initial comparison of the models were made using a 2-D, axisymmetric, non-swirling, PC combustion case described in several references (Fiveland et al., 1984, Fiveland and Jessee, 1994). Since the new submodels are only permitted with Lagrangian particles, the various permutations of the case only use this particle mode. Three model permutations are considered and are summarized in Table 1.

All cases were run with version 8.11.8 of COMOSM and all used the following models/methods:

- 1) k-epsilon turbulence model
- 2) SIMPLE algorithm for gas-phase flow solution
- 3) S4 discrete ordinate method for radiation heat transfer
- 4) Eddy dissipation gas-phase combustion model
- 5) Upwind advection scheme for all Eulerian transport equations

The operating conditions are detailed in the previously mentioned references. The 2-D axisymmetric domain was discretized using a non-uniform orthogonal mesh of 870 cells.

For the different cases, the results of axial velocity (U1), mixture temperature (TF), and oxygen (O₂), carbon dioxide (CO₂), and carbon monoxide (CO) concentrations are compared. For the three cases, the results are included in Figures 4-6, respectively.

In comparing the predictions, the biggest difference is the increased levels of CO₂ and higher temperatures for the cases using the CBK submodel. The Field model only reacts fuel carbon to CO while the CBK model reacts a portion of the fuel carbon to CO₂. This

results in higher temperature. The characteristics of the case, namely its 1-D nature and adiabatic boundaries, contribute significantly to the degree of variation in the predictions. Thus, these relatively large variations will not likely be seen in the analysis of commercial utility equipment. Nevertheless, the case is useful in highlighting the differences in the various heterogeneous reaction submodels.

Table 2 – Predicted Exit Values for BYU cases.

Case	Gas temp. (K)	CO (% kmol-i/kmol)	CO ₂ (% kmol-i/kmol)	O ₂ (% kmol-i/kmol)
1 : ubhay-field	2220	0.33	13.14	5.65
5 : ubhay-cbk	2294	0.10	14.16	4.34
6 : cpd-cbk				

Exit values for the cases are shown in Table 2. Included in the table are gas temperature, and CO, CO₂, and O₂ concentrations (mole fractions). The differences are largely attributed to the before-mentioned differences in the differences in char reaction products.

The CPU times for the three cases are displayed in Table 3. The activation of the CBK model in case 2 increases the CPU time by approximately 12%. The activation of the CPD model in case 3 increases the CPU time by approximately 353%. This may be expected since both the CPD and CBK models are more technically sophisticated than their respective counterparts. This increase in CPU time may be mitigated in the future by applying parallel processing and/or increasing the efficiency of the submodel calculations. The CPU times are all for 1000 global solution iterations. All cases were run on a Linux Cluster with 2.8 GHz Intel Xeon chips and Red Hat 8.0.

Table 3 – CPU Times for BYU cases.

Case	CPU time (s)*	increase over base
1 : ubhay-field	869	-
2 : ubhay-cbk	974	12%
3 : cpd-cbk	3936	353%

* the value represents the system time

The convergence history for the case 1 is shown in Figures 7. The momentum and mass residuals initially drop by three orders of magnitude over the first 300 iterations. Then, the stochastic nature of the particle dispersion takes over and the residuals level out. Lower levels may be achieved by increasing the sampling rate for the particle trajectories (i.e., number of trajectories) or relaxing the particle source terms. The residual histories for the other three cases exhibit similar characteristics and thus are not shown here.

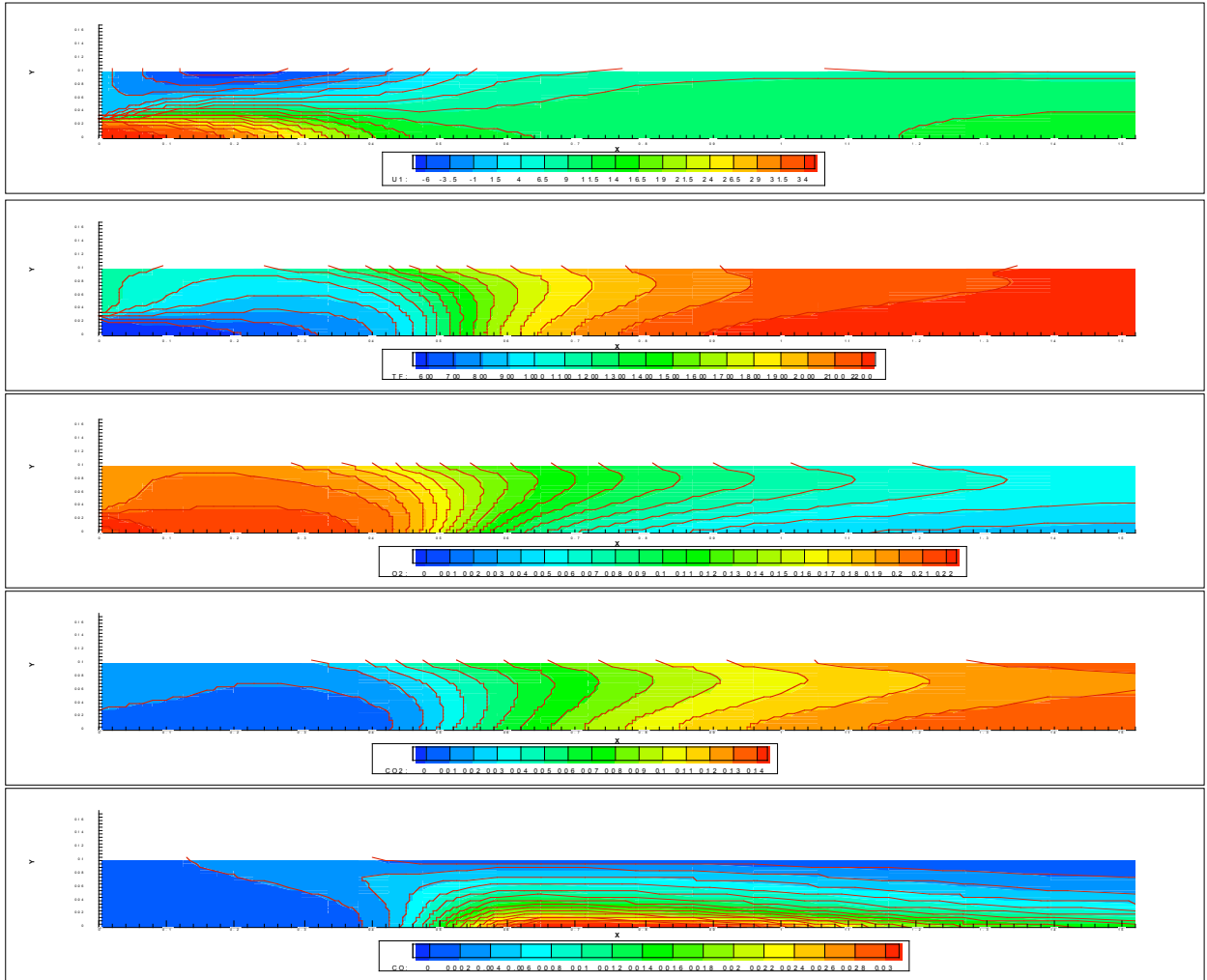


Figure 8.4 - State Contours for Case 1 (Ubhay-field).

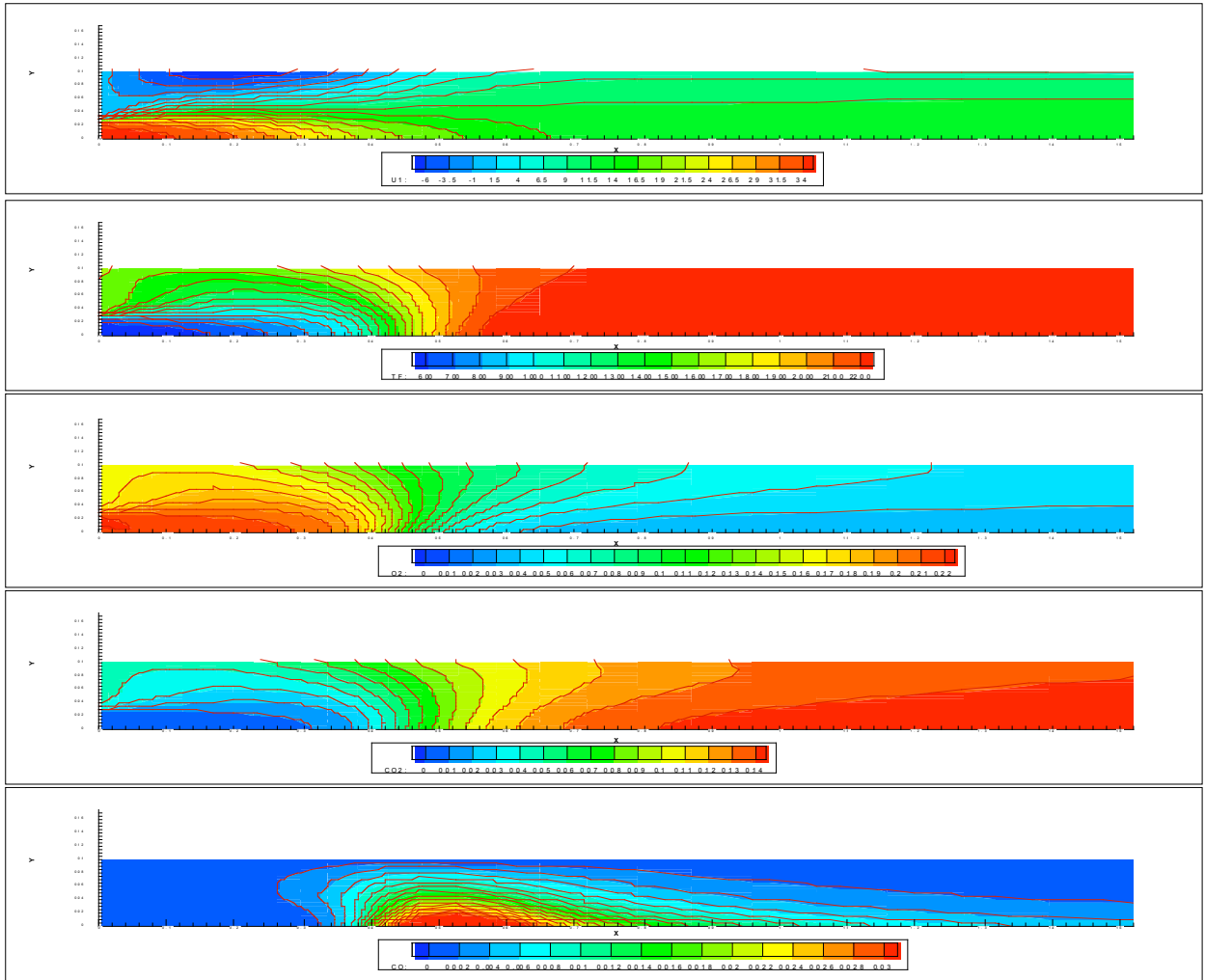


Figure 8.5 - State Contours for Case 2 (Ubhay -cbk).

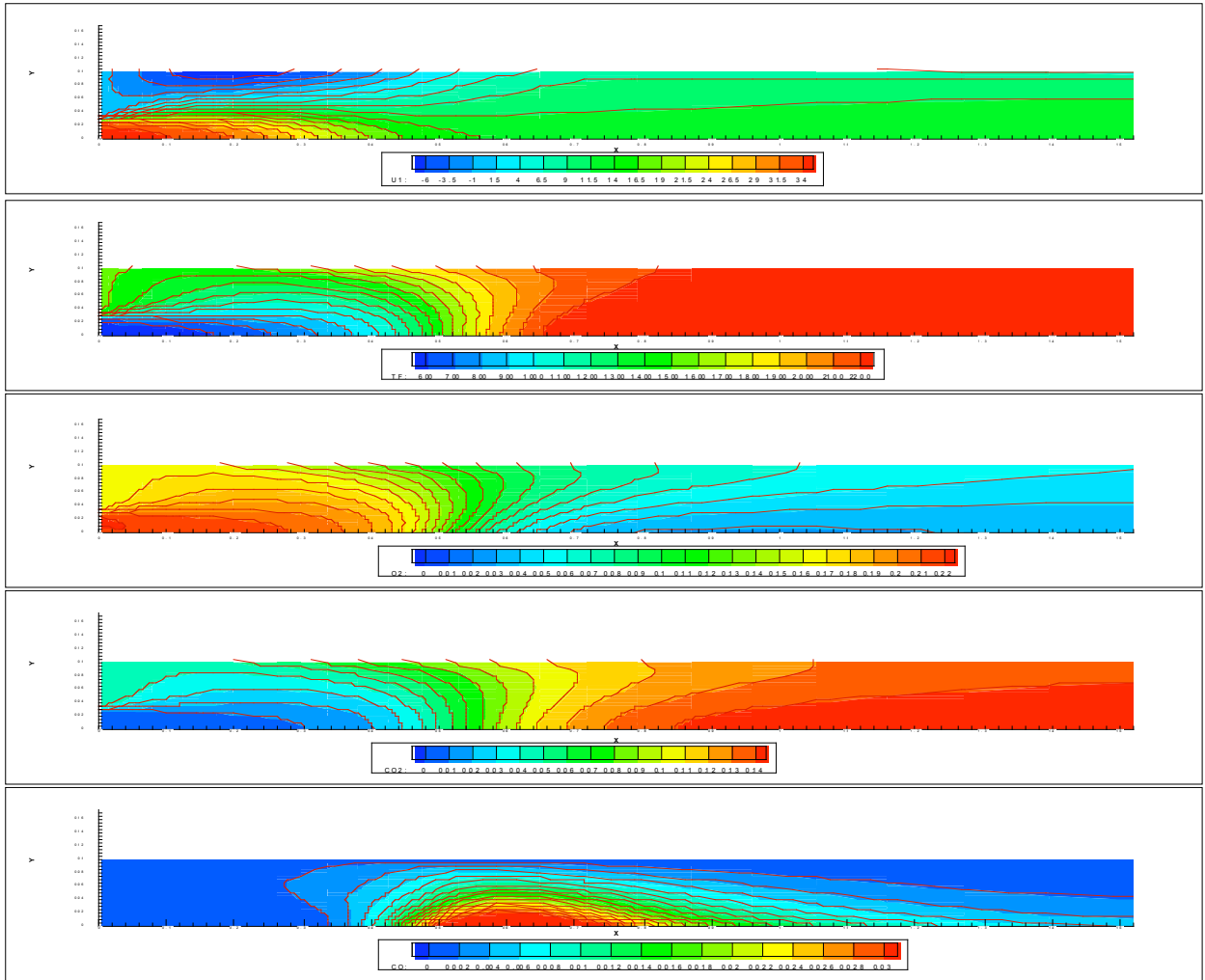


Figure 8.4 - State Contours for Case 3 (cpd-cbk).

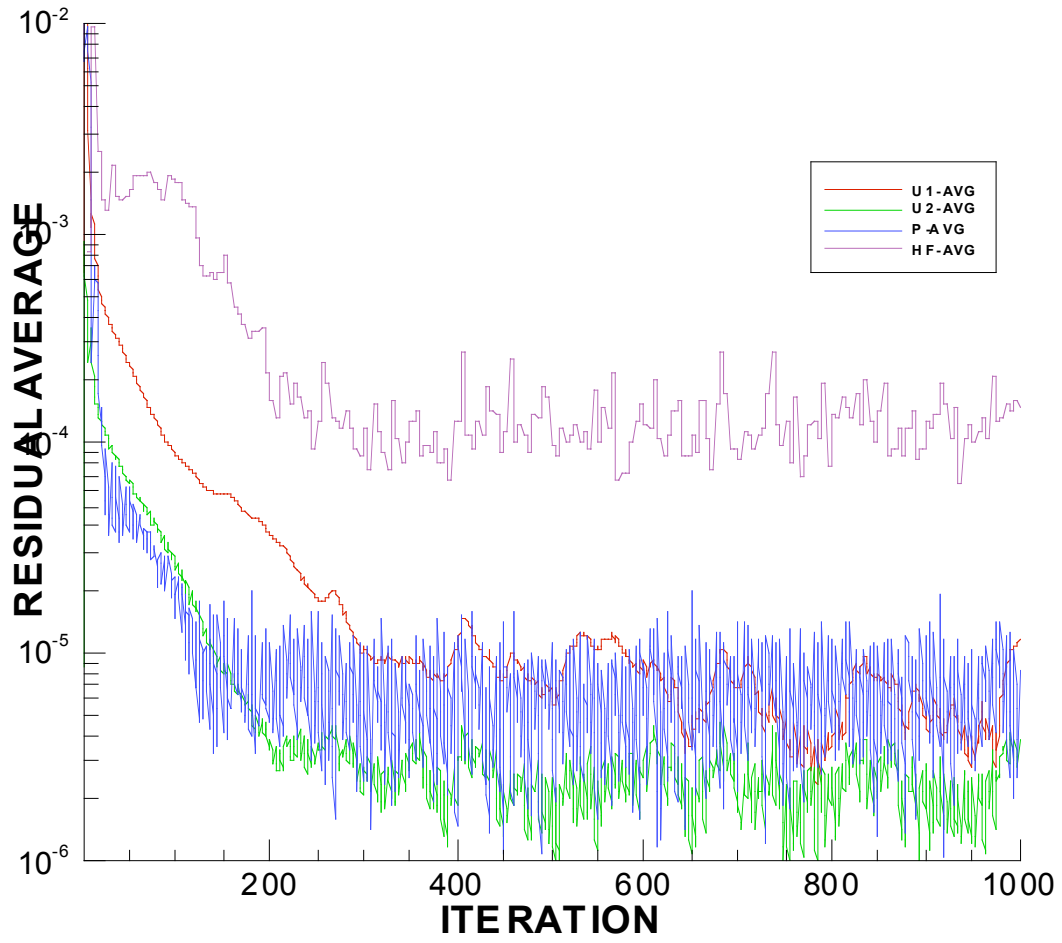


Figure 8.7 - Residual History for Case 1 (ubhay-field).

RECOMMENDATIONS

It is recommended that the coal constituent model in COMOSM be modified to incorporate functional groups for the functional groups containing oxygen (hydroxyl, carbonyl, carboxyl) and aliphatic H (Ar-CH₃)

REFERENCES

Allardice, D. J. and Evans, D. G., Chapter 7 "Moisture in Coal" in *Analytical Methods for Coal and Coal Products*, by Karr, C. Jr., ed, Academic Press, 1978, ISBN 012399901-04.

Bird, R. B., Stewart, W. E., and Lightfoot, E. N., *Transport Phenomena*, Wiley and Sons, New York (1960).

Field, M.A., Gill, D.W., Morgan, B.B., and Hawksley, P.G.W., Combustion of Pulverised Coal, The British Coal Utilisation Research Association, Leatherhead, Surrey, England, 1967.

Fiveland, W.A., and Jessee, J.P., "Mathematical Modeling of Pulverized Coal Combustion in Axisymmetric Geometries," 1994 Joint EPRI/ASME Power Generation Conference, Phoenix, Arizona, October 9-12, 1994.

Fiveland, W.A., Cornelius, D.K., and Oberjohn, W.J., "COMO: A Numerical Model for Predicting Furnace Performance in Axisymmetric Geometries," ASME Paper No. 84-HT-103, 1984.

Fletcher, T. H., "Time-Resolved Temperature Measurements of Individual Coal Particle During Devolatilization," *Comb. Sci. Tech.*, **63**, 89 (1989).

Fletcher, T. H., and Hardesty, D. R., "Compilation of Sandia Coal Devolatilization Data: Milestone Report," Sandia Report No. SAND92-8209, May 1992.

Fletcher, T. H., et al., "Chemical Percolation Model for Devolatilization. A Direct Use of ¹³C NMR Data to Predict Effects of Coal Type," Energy & Fuels, Vol. 6, No. 4, 1992.

Hurt, R., Sun, J.-K., and Lunden, M., "A Kinetic Model of Carbon Burnout in Pulverized Coal Combustion", *Combustion and Flame*, Vol. 113, p. 181-197 (1998).

Perry, S., Ph.D., Dissertation, BUY, "A Global Free-Radical Mechanism for Nitrogen Release During Devolatilization Based on Coal Chemical Structure," 2000.

Spalding, D.B., *Some Fundamentals of Combustion*, Butterworths Scientific Publications, London (1955).

Ubhayakar, S.K., Stickler, D.B., Von Rosenberg C.W. and Gannon, R.E., "Rapid Devolatilization of Pulverized Coal in Hot Combustion Gases," 16th International Symposium on Combustion, The Combustion Institute, 1975.

NOMENCLATURE FOR CHAPTER 8

A_p	=	particle surface area	(m^2)
c_p	=	heat capacity of the particle	$(J\ kg^{-1}\ K^{-1})$
C^*	=	Carbon in labile bridges	(\square)
$\frac{dT_p}{dt}$	=	rate of change in particle temperature	$(K\ s^{-1})$
$\square H_i$	=	heat of reaction i	$(J\ kg^{-1})$
\square_b	=	particle emissivity	(\square)
f	=	fraction of particle mass	(\square)
h	=	convective heat transfer coefficient	$(W\ m^{-2}\ K^{-1})$
h_{fg}	=	latent heat of vaporization of water	$(J\ kg^{-1})$
k_g	=	gas thermal conductivity	$(W\ m^{-1}\ K^{-1})$
\hat{M}_j	=	relative molecular weight of constituent i	$(kmol\ kg^{-1})$
m_p	=	mass of the particle	(kg)
N_{gs}	=	number of gas species	
n_{ij}	=	moles of constituent i per mole of solid species j	
N_R	=	number of chemical reactions	
Nu	=	Nusselt number	(\square)
Q_{conv}	=	convective heat transfer to the particle	(W)
Q_{rad}	=	radiative heat transfer to the particle	(W)
Q_{rxn}	=	effect of phase change and chemical reactions on particle temperature	(W)
\dot{r}_i	=	rate of reaction I	$(kg\ s^{-1})$
\square	=	Stefan-Boltzman constant	$(5.67 \cdot 10^{08}\ W\ m^{-2}\ K^{-4})$
\square	=	correction factor	(\square)
\square_{bb}	=	radiative flux to particle	$(W\ m^{-2})$
T_g	=	gas temperature	(K)
\square'_{jk}	=	stoichiometric coefficients of product species j	
\square_{jk}	=	stoichiometric coefficients of reactant species j	

CHAPTER 9

CONCLUSIONS

This multi-organization, multi-investigator project made significant progress in creating the necessary computer tools and fuel database entries for simulation of next-generation coal-based, fuel-flexible combustion and gasification processes. The main issue for pyrolysis is the effect of pressure for coals of various rank. By generating chars in both atmospheric and pressurized flat-flame burners (up to 15 atm), the team found a number of important trends. Volatiles yield decreases with increasing pressure, a trend that we also predicted using the CPD model using only the elemental composition and ASTM volatiles yields of the parent coals as changeable input parameters that relate to coal chemical structure. The H/C and O/C ratios in the resulting chars initially increase with increasing pressure, but remain relatively constant at pressures from 6 to 15 atm.

Swelling ratios of the lignite chars were less than 1.0, and only about 1.3-1.8 for the bituminous coals. All coal chars showed slight increases in swelling behavior as pressure increased. The swelling behavior observed for the Pitt #8 coal char at each pressure was lower than reported in high pressure drop tube experiments, supporting earlier work at atmospheric pressure showing that particle swelling decreases as heating rates approach 10^5 K/s. Both high pressure and low heating rate tend to increase swelling factors to values greater than those now used to describe atmospheric pc combustion.

Total char surface area, a parameter used in some char combustion models but not others, was found to decrease with increasing pressure. Char reactivities also decreased, when expressed on a per gram basis, but were found to be nearly constant on a per unit total surface area basis. We can thus expect high pressure chars to be somewhat less reactive, primarily due to loss of surface area, associated perhaps with decreased tar vaporization at pressure.

High-pressure, high-temperature char combustion experiments were also performed and the results analyzed with a combination of Fluent and the CPD and CBK submodels. The char oxidation rate was observed to increase with increasing total pressure. A different value of E or A_{30} was necessary for each pressure condition for each coal, meaning that a one-point calibration is necessary before CBK/E or CBK8 is capable of predicting char burnout at different pressures. The result obtained here that char reactivity increases with increasing total pressure is different than reported by some investigators. Some of that difference may be due to the fact that many previous investigators produced their starting char at atmospheric pressure only, rather than at the pressure where reactivity was measured (as was done in this study).

The work on pressurized combustion kinetics included a critical review and theoretical treatment of the global, power-law form and advanced, multi-step forms. One result is the first theoretical justification for the long-standing paradox of persistent, high fractional order in the char/oxygen reaction is surface heterogeneity. Simple models of surface heterogeneity, whether intrinsic or induced, predict power-law behavior over wide ranges of partial pressure if the breadth of the activation energy distribution for adsorption and/or desorption is large. The heterogeneous surface model of Haynes is a promising framework for describing the major features in the low-temperature carbon oxidation database including the persistent power-law behavior. More work is needed on the oxide oxidation step, $O_2 + C(O) \rightarrow products$ before a comprehensive model is available for application to the literature database.

The new theoretical work in this project sufficient underpinning to justify the use of the power-law form in practical char combustion modeling. The use of this form has practical advantages, but to date has lacked a fundamental basis and has led to much controversy and confusion in the field. There continues to be interest in the development and applications of more detailed rate expressions. If the field proceeds in that direction, the work carried out here suggests that the common 2-step Langmuir form is unsuitable, as it cannot predict the high fractional orders almost universally seen at low temperature. A possible promising direction is the use of three-step or four-step semi-global

mechanisms incorporating O₂-complex reaction as described here in Chapter 4. It remains to be seen if the added complexity relative to power-law approaches will allow this a popular approach in design applications.

This project also examined the *gasification* mechanisms at elevated pressure. CO₂ gasification reactivities were determined for a phenolic resin char and Wyodak coal char and the effects of total CO₂ pressure, CO₂ partial pressure, and the inhibition effect of CO on the reaction rate were investigated at elevated pressures. The results show that char reactivity increases monotonically with CO₂ partial pressure and the apparent activation energy *decreases* with *increasing* pressure. Further, reactivity *decreases* considerably with increasing CO partial pressure. The BYU coal char samples produced at high heating rates exhibited similar behavior; i.e., increasing reactivity with CO₂ partial pressure. The BYU chars were found to be much more reactive at high temperatures than the BU samples, but exhibited larger apparent activation energies, such that their reactivities became more comparable to that of the BU Wyodak samples at lower temperatures. This was attributed to the high heating rate ($\sim 10^5$ K/s) and very short pyrolysis times (~ 100 ms) experienced by the samples in the BYU FFB. This did not allow any time for thermal annealing, and thus produced high concentrations of active carbon sites.

This project also addressed the issue of fuel flexibility anticipated in next generation systems by providing a large database of comparative reactivities on coals and alternative solid fuels. A hybrid chemical/statistical model was developed that explains most of the observed reactivity variation based on four variables: the amounts of nano-dispersed K, nano-dispersed (Ca+Mg), elemental carbon (wt-% daf), and nano-dispersed vanadium, listed in decreasing order of importance. Catalytic effects play a very significant role in the oxidation of most practical solid fuel chars. Some degree of reactivity estimation is possible using only elemental analyses of parent fuels, but only if correlative techniques make use of the existing body of knowledge on the origin, form and dispersion of inorganic matter in various fuel classes.

Finally the project included a task in which advanced coal combustion submodels, Chemical Percolation and Devolatilization (CPD) and Carbon Burnout Kinetic (CBK) were modified and incorporated into a comprehensive computational CFD code. These models were implemented as subroutines in B&W's CFD code, COMOSM. In order to realize the increased accuracy from these advanced models the coal/char constituent model was reformulated to allow variable rates of progress for different gaseous products during devolatilization and char oxidation. This report gives a technical specification for the interface between these models and related chemical processes and physical properties.

Overall, the effects of elevated pressure, temperature, heating rate, and alternative fuel use are all complex and much more work could be further undertaken in this area. Nevertheless, the current project with its new data, correlations, and computer models provides a much improved basis for model-based design of next generation systems operating under these new conditions.